

NOTE TO USERS

This reproduction is the best copy available.

UMI[®]

University of Alberta

Photonics Applications of Nanostructured Thin Films

by

Scott Ronald Kennedy



A thesis submitted to the Faculty of Graduate Studies and Research in partial fulfillment
of the requirements for the degree of Doctor of Philosophy

Department of Electrical and Computer Engineering

Edmonton, Alberta

Spring 2004



Library and
Archives Canada

Bibliothèque et
Archives Canada

Published Heritage
Branch

Direction du
Patrimoine de l'édition

395 Wellington Street
Ottawa ON K1A 0N4
Canada

395, rue Wellington
Ottawa ON K1A 0N4
Canada

Your file *Votre référence*
ISBN: 0-612-96286-5
Our file *Notre référence*
ISBN: 0-612-96286-5

The author has granted a non-exclusive license allowing the Library and Archives Canada to reproduce, loan, distribute or sell copies of this thesis in microform, paper or electronic formats.

L'auteur a accordé une licence non exclusive permettant à la Bibliothèque et Archives Canada de reproduire, prêter, distribuer ou vendre des copies de cette thèse sous la forme de microfiche/film, de reproduction sur papier ou sur format électronique.

The author retains ownership of the copyright in this thesis. Neither the thesis nor substantial extracts from it may be printed or otherwise reproduced without the author's permission.

L'auteur conserve la propriété du droit d'auteur qui protège cette thèse. Ni la thèse ni des extraits substantiels de celle-ci ne doivent être imprimés ou autrement reproduits sans son autorisation.

In compliance with the Canadian Privacy Act some supporting forms may have been removed from this thesis.

Conformément à la loi canadienne sur la protection de la vie privée, quelques formulaires secondaires ont été enlevés de cette thèse.

While these forms may be included in the document page count, their removal does not represent any loss of content from the thesis.

Bien que ces formulaires aient inclus dans la pagination, il n'y aura aucun contenu manquant.

Canada

Abstract

Using an advanced thin film fabrication technique known as Glancing Angle Deposition (GLAD), it is possible to fabricate unique thin film nanostructures with characteristic dimensions on the order of a wavelength of light. By tailoring the morphologies of the films, they can be designed to exhibit particular optical properties that can be customized through advanced substrate motion and highly oblique flux incidence angles. In applications to photonics, controlling the flow of light for a specified task, GLAD thin films can be fabricated to provide the ability to manipulate incident light through controlled interactions of optical frequency electromagnetic radiation with the thin film nanostructures. Tetragonal square spiral photonic band gap crystals, a new class of periodic dielectric material that is characterized by the elimination of the density of states for frequencies lying in the stop gap of the crystal, can be fabricated using GLAD in a virtual single step process. The design and fabrication of these unique devices has been performed and the resultant crystals characterized in terms of optical response with respect to forbidden propagation modes, material properties, and advanced deposition techniques used to improve the overall structure. Chiral or helical thin films deposited using GLAD were also investigated, and have been shown to exhibit optical activity and circular birefringence due to their inherent structural anisotropy. It has been shown that the addition of nematic liquid crystals (LCs) to chiral thin films enhances the overall device performance due to order induced in the LCs by the film structure. This effect was investigated for a variety of materials and film structures. Finally, by developing a modified GLAD technique whereby the deposited film porosity is controlled through the angle of flux incidence, porous broadband antireflection

coatings were produced. Using an appropriate effective medium theory to describe the index of refraction profile of the coating in terms of the local film density, a model was developed to aid in the design and fabrication of graded index GLAD antireflection films.

Acknowledgements

This thesis is the result of more than four years of ups and downs, and without the help and support of so many people its compilation and the work included in it would not have been possible. First and foremost, I want to thank my family. To my Mom and Dad, thank you so much for all of your love and support, and for being the models of who I most want to be in life. To my sister and her family, Gaylene, Brent, Kayla and the new little Layden, thank you for always being there for me, for supporting me, and for being my best friends. To the love of my life, my girlfriend Genevieve, thank you so much for always lending an ear when I needed it, for always being supportive of whatever I wanted to do, for taking such good care of me and for being the best partner and friend a person could ask for. I couldn't have done it without you.

I have to sincerely thank Dr. Michael Brett, my supervisor, who had the vision to send me in the right direction, but gave me the freedom to wander in getting to my goal. And Karin Hayward, who had the impossible job of keeping us all organized, and in the process managed always to have time for me whenever I needed something.

I also have to thank the GLAD group who helped in so many ways. From the 'old' generation, M. Colgan, M. Jensen, M. Seto, B. Dick, D. Vick, K. Harris and J. Sit who not only provided sounding boards for new ideas, they also kept my mind and reflexes sharp with a couple games of foosball here and there. Also, the upcoming group of GLAD researchers, A. van Popta, P. Hruday, A. Elias, M. Summers, J. Gospodyn, S. Tsoi and J. Steele, many thanks for always questioning my thought processes and making me really think about what I was trying to do. To the members of Nanofab staff, K. Westra, K. Franklin, and N. Morin thank you for all of your work in developing the world-class facility where much of this work was carried out.

Finally, I would like to thank George Braybrook for the hours and hours he spent in a darkened room taking the perfect SEM photos and making something appear from nothing. Without your help, this work would be nothing but pages of pointless words.

Table of Contents

1	Chapter 1 – Introduction	1
1.1	Motivation	1
1.2	Scope	3
1.3	Thin Films	4
1.3.1	Introduction	4
1.3.2	Thin film deposition	5
1.3.3	Oblique incidence deposition	7
1.3.4	History of oblique deposition	8
1.3.5	Glancing angle deposition	10
1.3.5.1	Extreme angles of incidence	10
1.3.5.2	Columnar nanostructure	11
1.3.5.3	Substrate rotation	12
1.3.5.4	GLAD apparatus	13
1.3.5.5	Control software	15
1.3.5.6	Applications of GLAD films	18
2	Chapter 2 – Square Spiral Photonic Band Gap Crystals	21
2.1	Introduction – Photonic band gap crystals	21
2.1.1	Applications of photonic crystals	22
2.1.2	Photonic band gap theory	23
2.1.3	Photonic crystal dimensionality	28
2.1.4	Photonic band gap edges	29
2.1.5	Photonic crystal materials	29
2.1.6	Three dimensional photonic crystal structures	30
2.1.7	Classes of three-dimensional photonic band gap structures	31
2.1.7.1	Yablonovitch-Gmitter-Leung structure	31
2.1.7.2	The woodpile structure	32
2.1.7.3	Inverse opals	33
2.1.7.4	Square spirals	34
2.2	Tetragonal square spiral photonic crystals	34
2.2.1	Diamond and FCC lattice mapping	35
2.2.2	Square spiral structure parameters	36
2.3	Fabrication of square spiral photonic crystals	38
2.3.1	Substrate seeding	38
2.3.2	Tetragonal square spiral photonic crystals	42

2.3.3	Advantages of GLAD square spiral photonic crystals.....	45
3	Chapter 3 – Properties of Square Spiral Photonic Crystals.....	48
3.1	Deposited material characteristics of GLAD square spirals.....	48
3.1.1	Deposited silicon crystallography	49
3.1.2	Oxygen contamination	51
3.2	Advanced deposition control algorithms	53
3.2.1	Slow corner algorithm.....	53
3.2.2	Variable alpha post algorithm	56
3.3	Fabrication of SiO ₂ square spirals	62
3.3.1	SiO ₂ square spirals as an inverse template.....	62
3.3.2	Post-deposition annealing	64
3.4	Optical characterization of square spiral photonic crystals.....	65
3.4.1	Measurement of the three-dimensional band gap	66
3.4.2	Theoretical modelling of experimental results.....	72
3.4.3	Shift of the photonic band gap	74
4	Chapter 4 – Chiral Thin Film / Liquid Crystal Hybrids	76
4.1	Introduction to Chiral Optics.....	76
4.1.1	Optical activity and circular birefringence.....	77
4.1.2	Circular dichroism.....	81
4.1.3	Rotatory dispersion	83
4.2	Chiral GLAD/liquid crystal hybrids.....	83
4.2.1	Liquid crystals.....	85
4.2.2	Chiral nematics.....	87
4.2.3	Alignment of NLCs by chiral GLAD films	88
4.2.3.1	Fabrication of Chiral GLAD films	88
4.2.3.2	Addition of NLCs.....	90
4.2.3.3	Measurement of optical activity	91
4.3	Results.....	92
4.3.1	Film density manipulation by deposition angle	93
4.3.2	Film thickness	94
4.3.3	Wavelength properties of chiral thin films	98
4.4	Conclusions.....	100

5	Chapter 5 – Graded Index Antireflection Coatings	102
5.1	Antireflection coatings	102
5.2	Porous antireflection coatings	103
5.2.1	Graded index AR coatings	103
5.2.2	GLAD graded index AR films	106
5.2.2.1	Fabrication of customized density profiles	107
5.2.2.2	Fabrication of vertical projections	109
5.2.2.3	GRIN GLAD characteristic dimensions	111
5.3	Effective medium theory	112
5.3.1	Fundamentals of EMT.....	112
5.3.2	EMT simulation of GRIN GLAD films	114
5.3.3	Application of EMT models to GRIN GLAD	115
5.3.4	Scattering from GRIN GLAD films.....	116
5.4	Antireflection results	117
5.4.1	Effect of index of refraction profile	118
5.4.2	Wavelength properties of GRIN GLAD films	119
5.4.3	AR properties at non-normal incidence	122
5.5	Conclusions.....	123
6	Chapter 6 – Summary and Conclusions	125
6.1	Optical GLAD nanostructures.....	125
6.1.1	Square spiral photonic band gap crystals.....	125
6.1.2	Chiral thin film/liquid crystal hybrids.....	127
6.1.3	Porous broadband GRIN GLAD antireflection coatings	128
6.2	Recommendations	129
7	References.....	125
A	Appendix A – GLAD Nanostructure Control Routines.....	144
A.1	Slanted posts	144
A.2	Chiral nanostructure	145
A.3	Vertical posts	145
A.4	Zig Zags	146
A.5	Polygonal spirals.....	146
A.6	Exponential Capping	147
A.7	Antireflection coatings	147
A.8	User input file	148

B	Appendix B – Simulation of GLAD Antireflection Coatings	150
B.1	Effective medium theory	150
B.2	Characteristic Matrix Method	152
B.3	Rayleigh Scattering.....	154
B.4	Backside reflection	154
B.5	Matlab code files.....	155
B.5.1	Calculations for TE modes.....	155
B.5.2	Calculations for TM modes.....	158

List of Tables

Table 4.1 – Average effective rotatory powers of unfilled and NLC-filled films.	96
Table 5.1 – Characteristic dimensions of SiO ₂ GRIN GLAD films	112
Table A.1 – Input file example for deposition control	148

List of Figures

Figure 1.1 – Deposition at oblique incidence.....	7
Figure 1.2 – Initial shadowing of an obliquely deposited thin film.....	8
Figure 1.3 – Inclined columnar structure deposited at oblique incidence.....	9
Figure 1.4 – Slanted columnar SiO ₂ film.....	9
Figure 1.5 – GLAD deposition plane.....	12
Figure 1.6 – GLAD apparatus.....	13
Figure 1.7 – Basic GLAD nanostructures.....	15
Figure 1.8 – Substrate motion control block diagram.....	16
Figure 1.9 – GLAD software screen examples.....	17
Figure 2.1 – Comparison of photonic and electronic band structures.....	27
Figure 2.2 – Representative one, two and three-dimensional periodic crystals.....	28
Figure 2.3 – Electric field modes at high and low frequency band edges.....	29
Figure 2.4 – Yablonovitch-Gmitter-Leung photonic crystal structure.....	32
Figure 2.5 – Woodpile photonic crystal structure.....	33
Figure 2.6 – Self assembled opal and inverse opal photonic crystal structures.....	33
Figure 2.7 – Tetragonal square spiral photonic crystal structure.....	34
Figure 2.8 – Square spiral representation of the diamond lattice.....	36
Figure 2.9 – Comparison of individual ideal and fabricated square spirals.....	37
Figure 2.10 – Shadowing and deposition on a pre-seeded substrate.....	39
Figure 2.11 – Growth of slanted posts on a seeded substrate.....	40
Figure 2.12 – Square array of seeds fabricated by photolithography.....	41
Figure 2.13 – AFM image of 500 nm seeds.....	41
Figure 2.14 – Confinement of growth on a pre-patterned substrate.....	42
Figure 2.15 – A tetragonal square spiral PC structure.....	44
Figure 2.16 – Square spiral PC band diagram.....	45
Figure 2.17 – A 22.4 μm thick, 16 period square spiral crystal.....	46
Figure 2.18 – Engineered defects in a square spiral crystal.....	47
Figure 3.1 – Transmission electron microscope analysis of a silicon square spiral.....	49
Figure 3.2 – Energy dispersive x-ray analysis of a deposited silicon structure.....	52
Figure 3.3 – Square spiral film grown using the traditional method.....	54
Figure 3.4 – Representative schematic of the the slow corner method.....	55
Figure 3.5 – Comparison of traditional and slow corner growth techniques.....	56
Figure 3.6 – Relative flux distribution in, and normal to the deposition plane.....	57
Figure 3.7 – Comparison of the VAP and spin-pause methods.....	58
Figure 3.8 – Flux incidence for the ideal and actual VAP method.....	59

Figure 3.9 – Slanted posts grown with traditional and VAP methods.....	60
Figure 3.10 – SiO ₂ square spiral film	63
Figure 3.11 – Effects of annealing on a SiO ₂ square spiral film.....	64
Figure 3.12 – Silicon square spiral photonic crystal	67
Figure 3.13 – Band diagram for a silicon square spiral PC.....	68
Figure 3.14 – Normal incidence PC reflection spectra.....	69
Figure 3.15 – Grazing incidence FTIR PC reflectance spectrum	69
Figure 3.16 – In plane PC reflectance spectra	70
Figure 3.17 – Typical photonic band structures for two geometries of sq. spiral PC	71
Figure 3.18 – Variation with structure of PBG edges at normal incidence	73
Figure 3.19 – Large pitch square spiral PC and reflection spectra	74
Figure 4.1 – Linear and circularly polarized light.....	78
Figure 4.2 – Elliptically polarized light.....	82
Figure 4.3 – Chiral GLAD MgF ₂ film.....	84
Figure 4.4 – Phases of calamitic (rod-like) LCs.....	86
Figure 4.5 – Induced alignment of nematic LCs by a chiral GLAD film.....	88
Figure 4.6 – Filling of chiral GLAD films with NLCs.....	90
Figure 4.7 – Experimental setup for the measurement of optical activity	92
Figure 4.8 – Helical SiO ₂ GLAD films grown at varying angles	93
Figure 4.9 – Average effective rotatory power of chiral GLAD films	94
Figure 4.10 – Peak optical activity as a function of film thickness	95
Figure 4.11 – Optical rotation spectra of an NLC filled and unfilled MgF ₂ film	97
Figure 4.12 – Critical wavelength as a function of helical pitch	99
Figure 5.1 – Coordinate system used to describe the porous AR coatings.....	104
Figure 5.2 – Refractive index profiles for SiO ₂ GRIN GLAD coatings	106
Figure 5.3 – GLAD deposition of graded index films.....	108
Figure 5.4 – An SiO ₂ GRIN GLAD film.....	110
Figure 5.5 – Surface profile of a GRIN GLAD film	111
Figure 5.6 – Effective medium theory model representation of a GRIN GLAD film	114
Figure 5.7 – Transmission spectrum of a GRIN GLAD film	116
Figure 5.8 – Bandwidth results of GRIN GLAD AR films	119
Figure 5.9 – Index profile dependence of the wavelength of peak transmission.....	121
Figure 5.10 – Film thickness dependence of the wavelength of peak transmission	121
Figure 5.11 – Transmission spectra of AR films at oblique incidence	122
Figure B.1 – Coordinates used for GRIN GLAD modelling.....	152

List of Symbols and Abbreviations

a	Lattice period of a square spiral photonic crystal
AFM	Atomic force microscope
AR	Antireflection (used to refer to coatings that serve to reduce reflection and glare at an interface)
α	Flux incidence angle, measured from the substrate normal. $\alpha=0^\circ$ would be used in a traditional deposition while typical values for α in the GLAD regime are from $80 - 90^\circ$
\mathbf{B}	Magnetic induction field vector
β	Thin film column inclination angle
c	Vertical pitch of a square spiral, normalized to the lattice period, a
CMLL	Clausius-Mossotti-Lorenz-Lorentz (effective medium theory)
CVD	Chemical vapour deposition
\mathbf{D}	Displacement field vector
DC	Duty cycle
dz	Differential film thickness
e	Square spiral cross-section side length, normalized to the lattice period, a .
$\epsilon, \tilde{\epsilon}$	Dielectric constant
\mathbf{E}	Electric field vector
EMT	Effective medium theory
Φ	Pitch, for a chiral film corresponds to the amount of vertical growth per complete revolution of the microstructure
\mathbf{G}	Reciprocal lattice vector
GRIN	Graded index
GLAD	Glancing angle deposition
γ	Angle corresponding to the difference between the flux incidence angle, α , and the column inclination angle, β .
\mathbf{H}	Magnetic field vector
ϕ	Optical rotation, by an optically active medium
φ	Substrate rotation coordinate

k, \mathbf{k}	Wavenumber, wavevector
κ	Imaginary component of the index of refraction
L	Horizontal length parameter of a square spiral, normalized to the lattice period, a .
λ_{peak}	Wavelength corresponding to minimum reflection from an antireflection coating
LC	Liquid crystal
LPCVD	Low pressure chemical vapour deposition
m	Decay constant of films with gaussian density profile
MG	Maxwell Garnett (effective medium theory)
\tilde{N}	Complex index of refraction
$\hat{\mathbf{n}}$	Nematic director unit vector
n	Real component of the index of refraction
n_e	Extraordinary index of refraction
n_o	Ordinary index of refraction
NLC	Nematic liquid Crystal
PBG	Photonic band gap
PC	Photonic crystal
PVD	Physical vapour deposition
ρ	Film density
R	Reflectance
SEM	Scanning electron microscope
T	Transmittance
TEM	Transmission electron microscope
TE	Transverse electric
TM	Transverse magnetic
TN	Twisted nematic, orientation phase for nematic liquid crystals
VAP	Variable angle posts (method of fabrication used to produce more uniform inclined columns)
ω	Angular velocity
z_0	Physical film thickness

1 Chapter 1

Introduction

1.1 Motivation

Thin films are commonly found in a wide variety of optical devices due to the ability during fabrication to accurately control both the film's optical properties and thickness. For traditionally deposited thin films where the substrate is oriented perpendicular to incoming vapour flux, the device properties can be modified through both the physical thickness and the material properties of the deposited film. The film properties are determined by the choice of deposition material and conditions; however, for traditional substrate orientation there is relatively little control available from these variables. By depositing at non-traditional, highly oblique angles of incidence, porous thin films can be produced with accurately tailored micro- and nano-structures that provide another very powerful means of modifying the film's optical properties.

Glancing Angle Deposition (GLAD) is a thin film deposition technique implemented at highly oblique angles of incidence and developed to produce a variety of nanostructural shapes [1-3]. Although this technique has been used to fabricate devices for a wide variety of applications including sensors [4, 5] and micro-mechanical devices [6, 7], one of the most promising fields of application for these unique films is in the area of optics or photonics due to the size scale of the structures that is on the order of a wavelength of visible light. This thesis examines the development and fabrication of several new optical structures that can be produced using the GLAD technique and demonstrates the potential of these nanostructured thin films to the fields of optics and photonics.

Photonic band gap (PBG) crystals are a new generation of periodic dielectric structures whose importance to the field of photonics has been compared to the introduction of silicon to the fabrication of electronics. As they exhibit properties that are analogous to semiconductors, it has been proposed that in using PBG crystals, all-optical networks that avoid slow electronic conversion and processing will be possible. In

addition to networks used to transport information, optical transistors might be created using PBG crystal-based technology that can process photonic information in much the same way a modern computer processes electronic data, creating an optical computer with enormous bandwidth. Although the development of such science fiction-like devices is still far from being realized, the successful development of PBG structures has provided a great deal of enthusiasm for such ideas.

The capability of GLAD to accurately control the nanostructure of a thin film provides a natural ability to fabricate PBG crystals. A new generation of photonic crystals (PCs) has recently been proposed [8, 9] and using the GLAD technique the successful fabrication and characterization of such devices is shown. The ability to tailor the nanostructure of devices through the simple variation of deposition parameters allows for tuneable structures that can be readily optimized to produce the desired optical response.

Other optical devices such as chiral thin film/liquid crystal devices for application in flat panel displays are also investigated. Chiral thin films are easily produced using the GLAD technique and the combination of these structures made from optical materials and optically anisotropic nematic liquid crystal molecules shows a great deal of promise for highly versatile optical switches. By more thoroughly understanding the interaction of light with these hybrid devices it is possible to parameterize the optical response.

Other useful devices investigated with GLAD films are antireflection structures used to reduce glare and increase transmission through planar interfaces. The porosity of GLAD films is ideally suited to produce accurately tailored nanostructures that can virtually eliminate reflection from surfaces of high index materials. By parametrizing GLAD films for such applications, it is possible to tune the optical response and provide extremely broadband characteristics that can be implemented in a variety of applications.

All of the above optical devices fabricated by GLAD are extremely versatile and are easily modified through the control provided by the deposition technique. Properties such as wavelength response, wavefront differentiation and the overall magnitude of the specific optical response are readily altered through the choice of parameters specified in

the deposition control software. Consequently, GLAD provides a highly flexible method of producing a wide variety of photonic devices.

1.2 Scope

This thesis first introduces the general concept of GLAD and how it is implemented to produce porous nanostructures for optical applications. In the remainder of Chapter 1, the principles of oblique deposition, the development of the GLAD technique, the principle theory of the control software responsible for substrate motion, and finally some examples of other applications of GLAD films are introduced.

Chapter 2 highlights the revolutionary new square spiral photonic crystal structure that is produced using GLAD. The theory of PBG structures is introduced and several examples of other PBG structures are provided to compare the advantages of GLAD square spirals. The general fabrication techniques used to produce these complex dielectric structures are described and some examples of successfully fabricated structures are provided.

The more fundamental development of the fabrication process for producing square spiral PBG crystals is included in Chapter 3. The material properties, issues with fabrication, and some alternate or improved fabrication techniques are discussed. Also included in this chapter are optical characterization results of the square spiral structures demonstrating full three-dimensional band gaps in the infrared portion of the spectrum.

In Chapter 4, the study of hybrid chiral thin film/liquid crystal devices with enhanced optical activity and circular birefringence is discussed. The effect of thin film parameters and material on the optical response is investigated in an attempt to predict the properties of similar devices.

Broadband antireflection films with graded porosity fabricated using a modified GLAD technique are demonstrated in Chapter 5. Using the angle of incidence to control the film density, highly accurate index profiles are shown to provide extremely low reflectivity over a large range of wavelengths. In this chapter the fabrication technique and theoretical model are developed to provide highly predictable and favourable results.

Finally, in Chapter 6 the summary, conclusions and recommendations for future work in the field of optical porous thin films are provided.

1.3 Thin Films

1.3.1 Introduction

A thin film is a layer of material having one dimension, the thickness, which is much smaller than the other two. Fundamentally, it is a planar device where the effects and properties of confinement by the reduced thickness can be accounted for and measured independently of effects from the lateral dimensions. In the case of films used for optical or electronic applications, this definition can be further refined to quantify the maximum thickness in terms of wavelengths of electrons, periods of atoms, or optical thicknesses.

Although modern technology has provided an increase in the types and methods of producing thin films, they are far from being a new technology in themselves. Thousands of years ago, Egyptian craftsmen fabricated films by beating gold into sheets less than 1 μm thick to create ornately gilded items. The modern development of evaporated thin film technology started in the mid 19th century with Faraday when he exploded thin metal wires in an inert atmosphere [10]. The first use of a vacuum atmosphere to facilitate the evaporation of thin films was implemented by Nahrwold in 1887 [11] and subsequently in 1888 by Kundt [12] for the purpose of measuring the refractive indices of metal films. Subsequent developments in both vacuum and thin film technologies along with an increase in their use by reliant optics and microelectronics industries has thoroughly developed thin film processes, especially in the latter half of the 20th century. The modern use of both physical vapour and chemical vapour deposited films can be seen in an enormous variety of products ranging from high precision multi-layer coatings of dense wavelength division multiplexing optical communications filters to metallization coatings on plastic for potato chip packaging.

The concept of optical thin films was first spurred by the discovery of Newton's rings simultaneously and independently by Robert Hooke and Robert Boyle, however it was not until the lecture by Thomas Young in 1801 on his observation of the interference

of light that the development of optical thin films became a possibility. Following this discovery was the work by Fresnel on the laws of reflection and refraction, and in 1873 the seminal work by J. C. Maxwell [13] that provided the fundamental theory needed to fully develop the field of thin film optics [14]. These theoretical developments were followed by technological developments of the modern communications and microelectronics era to create multi-billion dollar industries concentrated on producing, among other types of thin film-based technologies, thin film optical devices. Although the work presented here is only concerned with a subdivision of optical thin film fabrication, the variety of thin film devices used in both optical and non-optical applications is enormous and many of the fabrication techniques can be found in references [15-17].

1.3.2 Thin film deposition

There exist two main classes of thin film deposition that provide the ability to produce thin, uniform coatings: physical vapour deposition (PVD) and chemical vapour deposition (CVD). The research presented in this thesis is concerned specifically with PVD films due to its directional dependence and as such the specifics of CVD processes will not be examined. PVD films result from a vapour of the thin film material produced by physical means that is allowed to condense on the substrate. Two of the most important PVD processes are evaporation [18] and sputtering [19]. In evaporation, vapour flux is produced by either resistively heating the film material in a refractory metal or Al₂O₃ coated boat, or an electron beam focused onto a crucible [20, 21] is used to heat the material to a temperature corresponding to a vapour pressure of approximately 10⁻² torr [18]. The evaporated atoms make their way unimpeded through a high vacuum atmosphere to the substrate where they can form the coating. In sputtering, a plasma discharge is most commonly used to produce gas ions that are accelerated toward the target material where the impact of the collision dislodges some of the target atoms and provides the vapour flux. Due to the requirement of higher pressures to supply enough gas to sustain the plasma discharge in sputtering, the mean free path of the vapour atoms is much shorter than in evaporation. Also, the kinetic energy of the atoms in sputtering is much higher than in evaporation (2-40 eV vs. 0.2-0.3 eV) resulting in different film

structures due to the more energetic impingement at the substrate. These two factors make sputtering generally unsuitable for the production of nanostructured thin films, although some success in fabrication has been shown [22], and thus evaporation is the chosen method of deposition for the films fabricated for this research.

To avoid collisions between ambient gas molecules and the evaporated vapour atoms, and to restrict contamination by unwanted reactive gases, PVD deposition by evaporation is performed in a high vacuum atmosphere. The mean free path of a vapour atom *in vacuo* is given by [23]

$$\lambda = \frac{kT}{p\pi\sqrt{2}d_0^2} \quad (1.1)$$

where T is the average temperature in Kelvin, k is the Boltzmann constant, p is the pressure and d_0 is the molecular diameter. To have a collision free trajectory between the source and substrate, the mean free path should be much greater than the distance separating the two, in the case of GLAD system this value is 42 cm. Using approximate values of room temperature and 3Å for the molecular diameter, a maximum pressure of approximately 1×10^{-5} torr needs to be maintained by a high vacuum pump such as a diffusion or cryo-pump to avoid scattering of vapour flux. The requirements on avoiding contamination by gas molecules such as oxygen are even more stringent and require pressures to be less than 1×10^{-6} torr. This second pressure is then the upper limit on the deposition of most elemental thin film materials.

Four processes characteristic of thin film growth can occur when vapour flux impinges on a substrate: surface diffusion, bulk diffusion, desorption and self-shadowing [17]. The first three are uniquely thermal processes and are reliant on the substrate temperature that can range from liquid nitrogen temperatures (77K) to several hundred degrees Celsius depending on the configuration of the deposition system. Structure zone models have been proposed for evaporated [24] and sputtered [25] films that provide insight into the role of temperature and pressure (for sputtered films) in producing films with varying structure and crystallinity. More recent models have also been proposed that predict both the micro- and nano-structure of the films giving a more comprehensive view of thin film morphology and growth under a wide range of deposition conditions

[26, 27]. The final process mentioned above, self-shadowing, is dependent only on the geometry of the deposition and includes factors such as flux energetics, collimation and distribution. This process is of critical importance to the fabrication of GLAD nanostructured porous thin films and given certain conditions its effect can overcome many of the characteristic effects of thermal processes.

1.3.3 Oblique incidence deposition

Deposition of films onto substrates oriented with the flux incident at an oblique angle accentuates the effects of self-shadowing and at highly oblique, or glancing angles, highly porous films with anisotropic structures are fabricated. Thermal processes such as the diffusion of adatoms tends to blur the fine structure produced by oblique deposition by filling in voids; however, increased self-shadowing serves to isolate the individual growths by preventing the impingement of flux in certain regions. As the angle of incidence is increased, so is the geometric self-shadowing and at a particular angle of incidence for a set of deposition parameters (material, flux distribution, temperature, vapour energetics, and background pressure) diffusion into void regions is overcome and individual, isolated structures are produced. This effect is shown in Figure 1.1 where the increased deposition angle creates more self-shadowing, resulting in isolated, slanted columns.

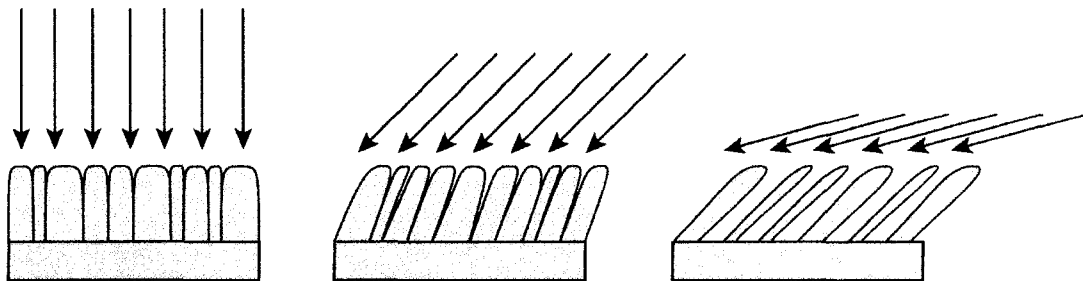


Figure 1.1 – Deposition at normal incidence, oblique incidence, and highly oblique incidence. As the deposition angle becomes more oblique, the columnar structure of the film becomes isolated due to self-shadowing. At highly oblique incidence, individual structures are grown.

1.3.4 History of oblique deposition

Oblique deposition was first reported in the late 1950's in applications of magnetically anisotropic films [28-30]. Simultaneously, optically anisotropic films were fabricated by Young and Kowal, where in addition to the use of non-normal angles of incidence, the substrate was rotated during deposition to produce optical activity [31]. Investigations of the magnetic films revealed that the anisotropy was due to restriction of growth by self-shadowing of the structures during deposition that, in turn, produced elongated growths in the direction of incident flux. In particular, three principal axes were found from measurements of both the optical and magnetic properties. The first is oriented along the axis of growth of the isolated column, lying in the deposition plane, the second, again in the deposition plane perpendicular to the inclined column, and the third parallel to the plane of the substrate perpendicular to the deposition plane [32]. Due to reduced shadowing along the direction of the last principal axis, chaining of slanted columns is often seen and results in a density intermediate to the other two principal directions [30].

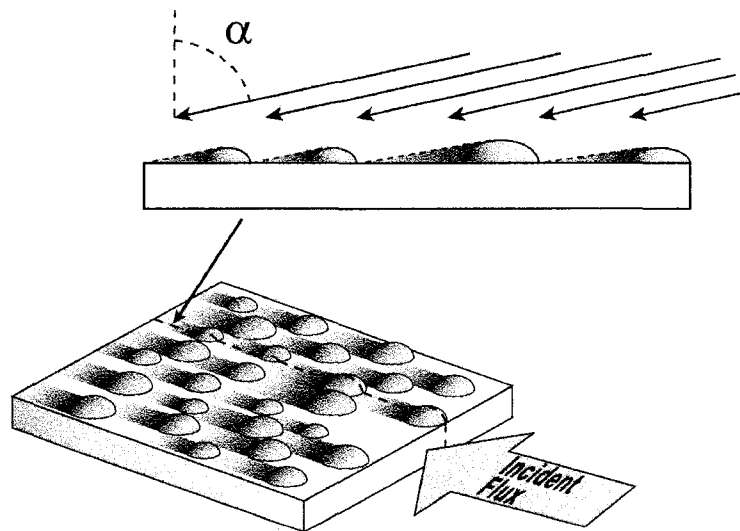


Figure 1.2 – Shadowing in the initial growth stage of an obliquely deposited film. Critical nuclei form and shadow the region behind them if the angle of incidence, α , is large enough. Because of self-shadowing, subsequent growth can only occur on the tops of existing growths.

In the initial stages of growth of an obliquely deposited thin film, forming nuclei shadow the region opposite the direction of incoming flux preventing growth in these

areas of the substrate. The example of Figure 1.2 demonstrates this initial shadowing in relation to the angle of incidence, denoted α , and measured from the substrate normal. As the film continues to grow under maintained oblique angles of incidence, a tilted columnar morphology results with the columns favouring the direction of the incoming flux. Self-shadowing is maintained by the film as it grows as seen in Figure 1.3, where

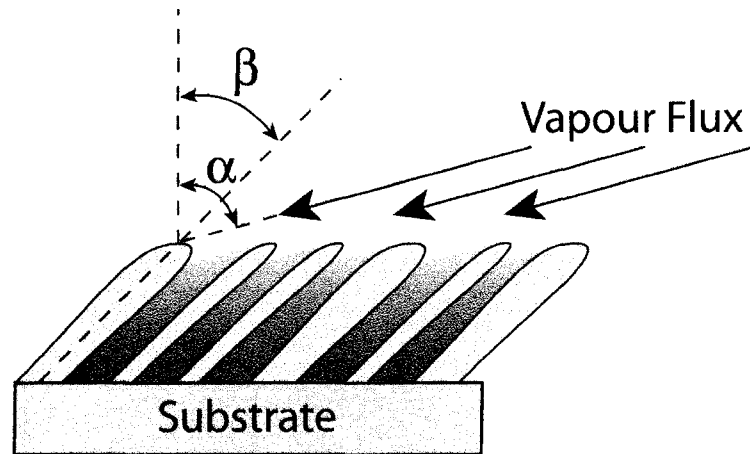


Figure 1.3 – Slanted columns of an obliquely deposited film. To maintain shadowing the growth angle, β , is less than the angle of incidence, α . Isolated structures are produced for large α .

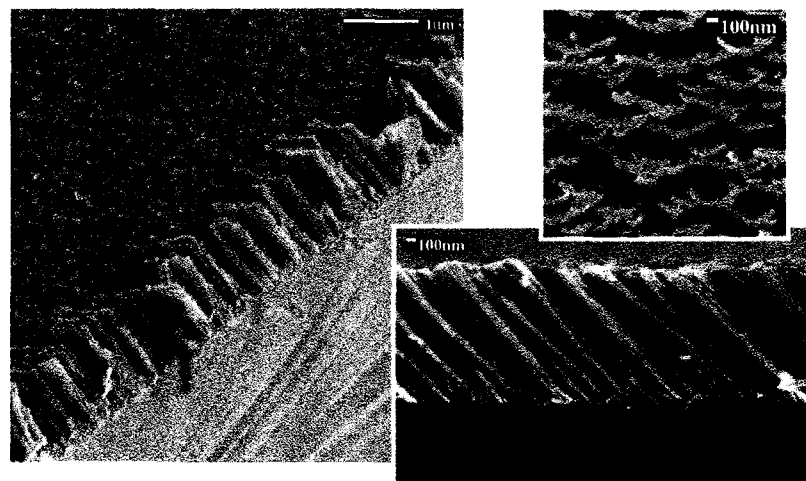


Figure 1.4 – Slanted column SiO₂ film grown at an angle of incidence of 85°. Shadowing in the deposition plane causes the growths to be isolated from the columns in front of them, while reduced shadowing perpendicular to the deposition plane causes chaining. Clockwise from left are an oblique view, an end-on view of the columns, and a substrate edge view.

only the top edges of each of the columns can accumulate impinging vapour particles. An SiO₂ film deposited at 85° is seen in Figure 1.4, demonstrating the most elementary obliquely deposited film composed of fine, tilted columns. The column tilt angle, β , for this film is much less oblique than the nearly perpendicular flux angle and is approximately 55°. The top right frame of Figure 1.4 shows chaining of columns perpendicular to the plane of incidence due to reduced self-shadowing in this direction.

1.3.5 Glancing angle deposition

1.3.5.1 Extreme angles of incidence

In earlier work, films grown by oblique deposition were maintained at more conservative angles of approximately 70°. At these angles the film structure is highly anisotropic, yet the overall film microstructure is not that of completely isolated individual growths. In 1995, a paper by Robbie *et al.* demonstrated the initial results of investigation into deposition at highly oblique angles, greater than 70° [33]. It was found that in this regime a unique class of films could be fabricated with highly porous and accurately tailored nanostructures [3, 34-37]. The extreme angles of incidence set this method apart from many other oblique deposition methods that either had already been performed or have been developed since [38-42], and due to the unorthodox substrate orientation, films deposited by this process with $\alpha > 70^\circ$ have been classified as Glancing Angle Deposition, or GLAD films.

Substantially different film structures can be fabricated in the GLAD regime depending on the angle of incidence. At angles closer to 70° the films are relatively dense and although the microstructure is still composed of individual growths, the spacing and porosity are much less than at angles approaching tangential incidence. The majority of GLAD films are deposited at angles ranging from 80 to 90°, producing the fine isolated structures similar to the slanted columns of Figure 1.4. Due to the inclined geometry of the columnar films, the deposition rate normal to the substrate is inefficient due to the accumulation of vapour flux on the sides of the growths as opposed to the tops. The cosine-like dependence of vertical growth on the column angle, β , results in a reduced effective deposition rate normal to the substrate and for typical deposition angles

of 80 to 85° corresponding to column growth angles of approximately 60°, the rate is reduced by a factor of approximately two-thirds.

1.3.5.2 Columnar nanostructure

The tilted columnar nanostructure of obliquely deposited thin films grows toward the direction of incoming flux, but as shown in Figure 1.3, the column angle, β , differs from the flux incidence angle due to the geometry imposed by self-shadowing. The exact orientation of the columns depends on many factors specific to the deposition conditions, however a general relationship was found between the column inclination and flux incidence angles early in the investigation of these unique films. This empirical expression, known as the Tangent Rule, and given by the expression [43],

$$\tan \beta = \frac{1}{2} \tan \alpha \quad (1.2)$$

was found to be in good agreement with results of aluminum films deposited at angles up to 80°. Initial modelling of oblique films confirmed this result through geometric arguments in conjunction with atomic relaxation of incidence hard sphere particles [44]. However, the dependence of columnar orientation on material properties, in particular adatom mobility and diffusion lengths, has led to more general models that replace the factor of one-half in Equation 1.2 with a material specific constant [45, 46]. These models provide reasonably accurate predictions for the inclination angle of the tilted columns, yet for deposition angles greater than 60° they were found to produce results that diverge from values obtained for actual deposited films. A new formulation for $\beta(\alpha)$ was subsequently developed by Tait *et al.*, based purely on geometric arguments at large angles of incidence and has proven to be accurate for incidence angles up to 90° and for a wide range of materials. The resulting function for the column inclination is known as Tait's Rule and is given by the expression [47]

$$\beta = \alpha - \sin^{-1} \left[\frac{1 - \cos \alpha}{2} \right] \quad (1.3)$$

This result is extremely useful when designing nanostructured thin films with applications that are reliant on precise control of the film structure. One application of

this result is shown in Chapter 5 with the design and fabrication of large bandwidth antireflection coatings.

1.3.5.3 Substrate rotation

The simplest form of GLAD thin film is the tilted columnar structure of Figure 1.3 where the columns grow toward the direction of incoming vapour flux in a manner prescribed by the relationships above. If a second degree of freedom is added to the motion of the substrate permitting it to rotate about an axis normal to the surface, the effect is to create a deposition plane with variable orientation relative to previous growth. A schematic of this case is shown in Figure 1.5 where rotation of the substrate is denoted by the angular quantity ϕ . As the growing columns tend to track the direction of incident flux, it is possible to create a wide variety of nanostructures by simply having the substrate rotate in a predetermined manner throughout the deposition.

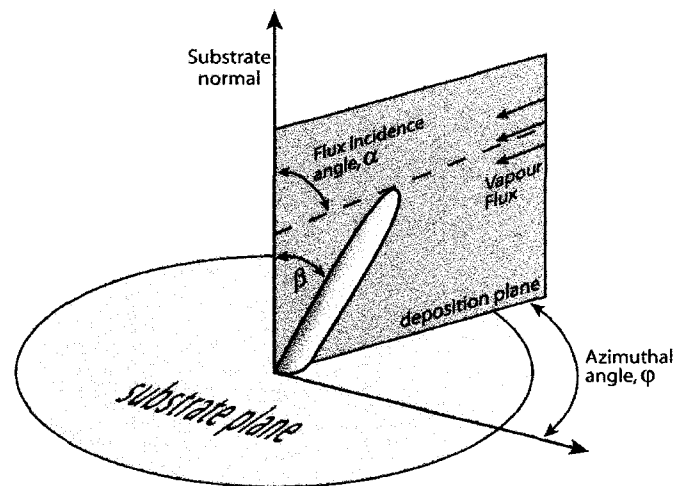


Figure 1.5 – Deposition plane representation for oblique incidence. By rotating the substrate through an angle ϕ , the deposition plane is moved. As the column growth tracks the substrate rotation, it is possible to create a wide variety of nanostructures through the combination of motion in α and ϕ .

The rotation of the substrate is ultimately responsible for the structure morphology whereas the angle of incidence alters only the porosity of the film through its control over self-shadowing. The combination of motion in the two dimensions allows for a wide variety of structures to be produced other than the simple columnar shapes. Spring-like helices or abruptly discontinuous zigzags can be uniquely fabricated through

the use of substrate rotation. Motion in the ϕ direction is used to control the handedness and resulting properties of some films in regards to interactions with linear or circularly polarized light, along with being able to create specific shapes for many other applications.

1.3.5.4 GLAD apparatus

To implement the GLAD process and control both the rotation, ϕ , and angle of incidence, α , of the substrate, a specially designed substrate mount with two high temperature vacuum compatible stepper motors is used.¹ Shown in Figure 1.6 is a schematic of the GLAD apparatus placed above an electron beam source, the most common method of deposition. The substrate is mounted with its centre positioned at the intersection of the two rotation axes and in an attempt to restrict the angular distribution of flux on the substrate, a large throw distance of 42 cm is used between the crucible where the vapour is produced, and this origin.

The stepper motors responsible for controlling the substrate orientation are wired in half-step mode corresponding to 400 steps per complete rotation or an angular resolution of 0.9° . The motor controlling the flux incidence angle is also used in conjunction with a 5:1 gearbox, further increasing the angular resolution of α to 0.18° . The angle of incidence is normally restricted to values from 0° to approximately 99° (facing slightly away from the source to prevent any flux from accumulating on the substrate) and the rotation, ϕ , can be any value in the set $(-\infty, \infty)$.

Several of the most common GLAD structures fabricated using the above apparatus are shown in Figure 1.7. A helical film is fabricated by constant, slow rotation in ϕ relative to the deposition rate. The vertical post nanostructure is a variant of the helix where the rotation is rapid and causes the helical arms to merge into a single column. The discontinuity of a zigzag film is created by rapid, instantaneous rotation by 180° when the film thickness reaches one half the pitch. Finally, by combining motion in

¹ Empire Magnetics, www.empiremagnetics.com
VC-U21P:10 flux angle motor (α)
VC-U23 rotation motor (ϕ)

the α and φ dimensions, a solid capping layer can be deposited on top of an existing highly porous film.

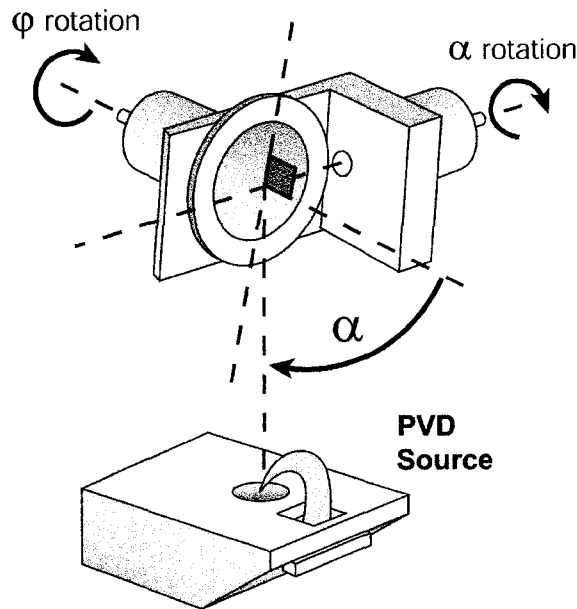


Figure 1.6 – Schematic of the GLAD apparatus. The substrate is mounted on a circular chuck at a large distance from the source. The α and φ stepper motors control the orientation of the substrate through outputs from the control computer.

For most film structures, the pitch is one of the most critical dimensions and can be set to tailor the resulting deposited film. The pitch, Φ , is defined as the film thickness of one complete nanostructure period. For helices and posts this corresponds to the completion of one rotation by the φ motor, while for the zigzag film, the pitch is composed of two arms and two 180° turns.

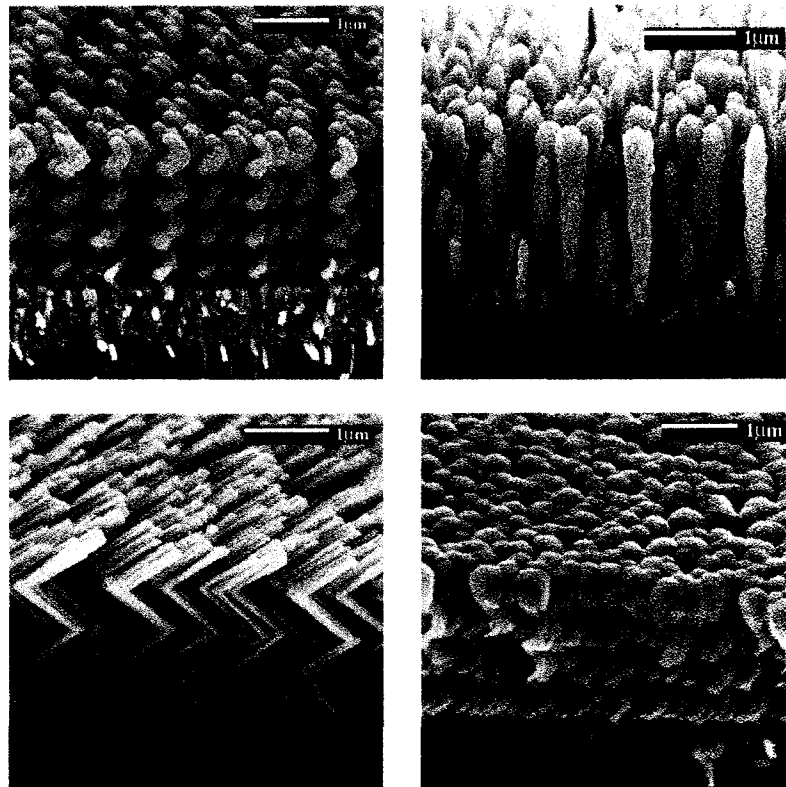


Figure 1.7 – Examples of basic GLAD nanostructures. From left to right, top to bottom are an SiO_2 helical film with 350 nm pitch, an SiO_2 vertical post film with a 20 nm pitch, an Si zigzag film with an 800 nm pitch and an exponentially capped Al_2O_3 helical film.

As GLAD uses traditional PVD methods for source material evaporation, the films can be fabricated from a wide variety of materials. Metals, semiconductors and dielectrics such as oxides and fluorides can be easily deposited by thermal or electron beam evaporation to produce an array of films for different applications. Some of the most common deposition materials with favourable deposition and film properties are silicon, silicon dioxide, aluminum, aluminum oxide, and magnesium fluoride. Although other complex compounds such as GaAs and LiNbO_3 must be avoided due to the dissociation of the constituent elements when heated, many films have been successfully fabricated using numerous other materials.

1.3.5.5 Control software

Positioning of the substrate at precise intervals during the deposition is critical to the fabrication of GLAD films with particularly designed nanostructures. The means by

which the desired orientation is implemented is through the use of stepper motors, which are in turn under the control of software running on a personal computer and linked via a custom built controller.

To provide the software with the information necessary to accurately manage the deposition, a control loop is used and is represented by the block diagram picture of Figure 1.8. The control system is divided into four main sections: the control software with the desired functions for α and ϕ with respect to the thickness, z , the computer hardware responsible for the physical input and output from the software, the interface electronics which drive the motors in response to the digital signals from the computer, and finally the deposition system which is composed of the two stepper motors and the crystal thickness monitor (CTM). This last item, the CTM is the critical feedback device that provides film thickness information to the computer software so that accurate nanostructures can be produced.

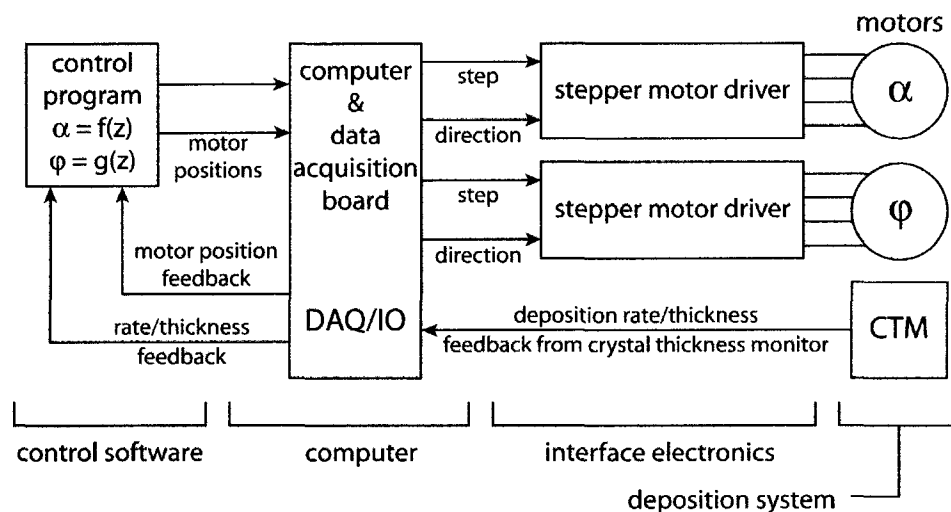


Figure 1.8 – Substrate motion control block diagram. A personal computer with the control software is interfaced with the stepper motors through custom drive electronics and deposition rate feedback is provided by a quartz crystal thickness monitor. From J. Sit [48].

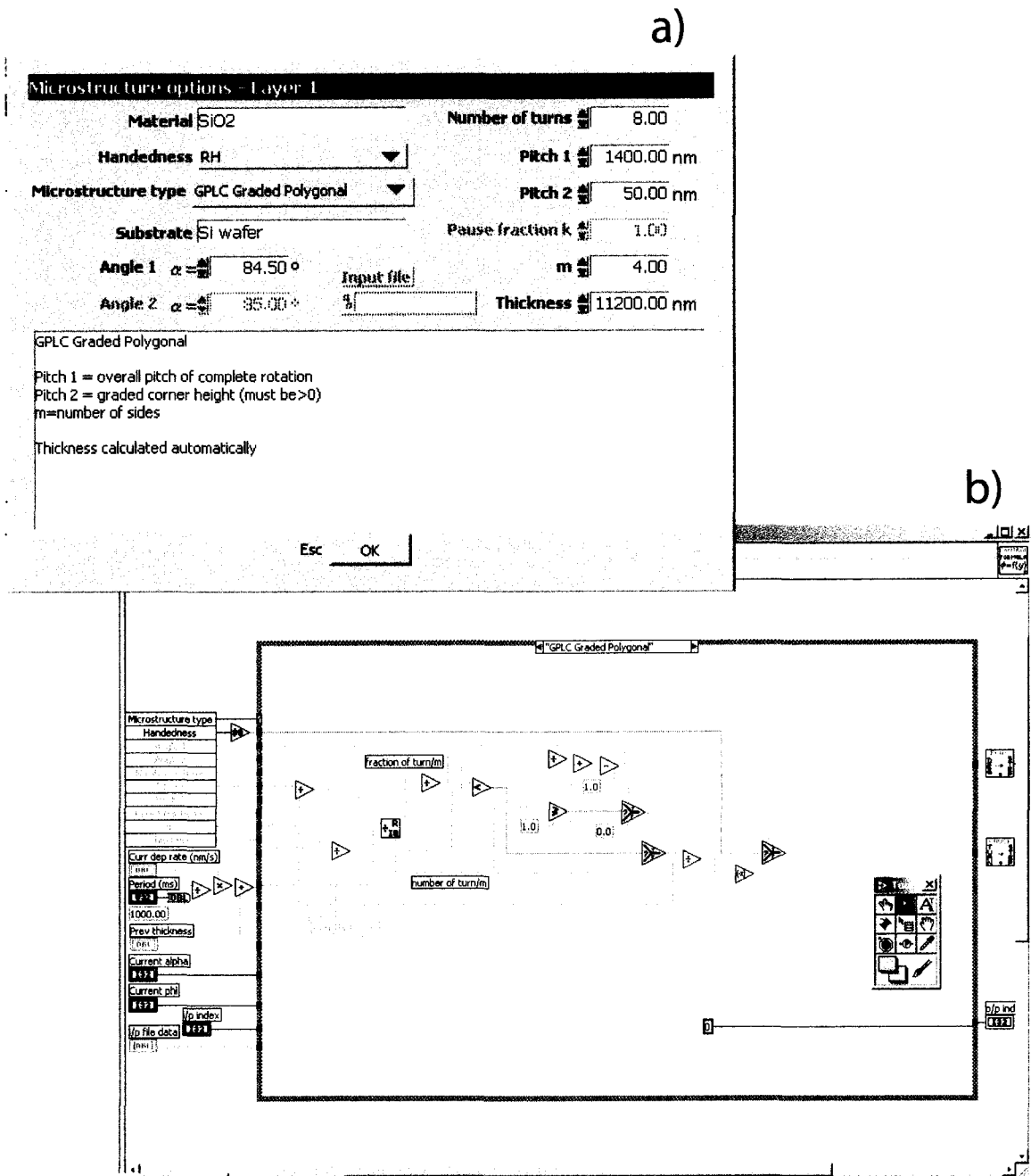


Figure 1.9 – GLAD software screen examples. a) User input screen where the nanostructure and parameters are specified. b) Graphical programming implementation of the selected nanostructure.

The CTM is placed as close to the film substrate as possible to avoid differences in the measured rate and the actual rate at the substrate and it is oriented with the flux incident normal to the crystal. The thickness of the actual deposited film is calculated by time integration of the deposition rate provided by the CTM. The integrated thickness is

indicative of a flat, or normally deposited film instead of the slanted columns that are produced in GLAD deposition and to calculate the actual film thickness including the cosine-like dependence on column angle, an empirical correction factor of approximately one-third is used.

The nanostructure of GLAD films is determined by the mathematical functions for the substrate motion, which are written and implemented by LabVIEW² control software. Shown in Figure 1.9 are examples of a user screen and the graphical programming used to control the motion of the substrate. Control routines for specific nanostructural shapes are programmed into the software and variables are used to allow for fine-tuning of the specific film features. The user input screen shown in Figure 1.9a allows for several parameters to be entered that are specific to the nanostructure. The general structure is selected from a list of pre-programmed structure types and is chosen from a drop-down menu. By selecting the general nanostructure class, the control formulas for the substrate motion are selected and the user inputs are passed to the appropriate control algorithm. Shown in Figure 1.9b is an example of the substrate motion implementation for a graded corner square spiral structure, a nanostructure that has been developed for applications in photonic band gap crystals and is the topic of Chapters 2 and 3. Some examples of the control routines for GLAD nanostructures developed throughout this research are also provided in Appendix A.

1.3.5.6 Applications of GLAD films

GLAD thin films are extremely versatile in the production of a wide variety of micro- and nanostructures. The applications of such film-based devices are often based on the nanometre scale structure and shape, which is controlled through the many available deposition parameters. As a wide variety of materials may be used to fabricate GLAD films, the applications can also be tailored by material properties.

The most prolific use of GLAD films has been in the fields of optics and photonics, and is the subject of much of the following research. As GLAD films can have nanostructures on the scale of a wavelength of visible light, the interaction between

² National Instruments Corporation, www.ni.com

incident electromagnetic wavefronts and the film structure is unique. Form birefringence is often seen in films deposited at oblique incidence for both linear and circular polarizations (the topic of Chapter 4) where optical dielectric materials are deposited in a variety of ways to produce filters or optically active devices [2, 42, 49-51]. More recently, photonic band gap crystals with complex three-dimensionally periodic high ϵ materials have been used to create stationary states for light and are the topic of Chapters 2 and 3 [52, 53]. Also, the controlled porosity of thin films has allowed for the fabrication of devices such as graded index antireflection coatings [54], the subject of Chapter 5.

The large surface area of porous GLAD films deposited at angles greater than 80° have aided in their application to sensing devices. By depositing platinum films at oblique angles of incidence, gas sensors with extremely high resolution have been fabricated [4]. Other structures such as vertical SiO₂ GLAD posts have allowed for rapid sensing of ambient humidity levels through the measured change in capacitance across the film [5, 55, 56]. The controlled porosity of these films can also be applied to other types of gas and liquid sensors and many new applications are currently under investigation. The high porosity of GLAD films has made them useful in applications to thermal insulation or thermal barrier coatings. Materials with low thermal conductivity such as ZrO₂ can be deposited with porosities greater than 50% providing thermal isolation of the substrate from harsh, high temperature environments [57]. Finally, the increased surface area of GLAD manganese films has shown promise in electrochemical charge storage devices, or supercapacitors, providing extremely large capacitance values for small areas of film material [58].

The individual, isolated vertical posts characteristic of many GLAD structures have also shown promise in applications to magnetic storage media. By depositing ferromagnetic metals such as nickel and cobalt, individually addressed structures can be produced and used to store digital data in a manner similar to the hard disks common to most computers [59]. The small size scale of GLAD films allows for increased storage density and the ease in fabrication makes this process suitable for large scale production.

The structure of GLAD films has also been implemented in emissive devices. By sharpening the tips of carbon and silicon vertical posts using energetic ion bombardment, substantial gain has been made with respect to the threshold voltage for vertical electron emission from the GLAD structures [60]. Such films could find use in applications to field emission displays. Luminescent emission is also possible from GLAD films when deposited using an appropriate material such as Y_2O_3 doped with Eu [61]. Using similar structures as those designed for chiral optical devices, the structural anisotropy is predicted to produce light emission with preferential polarizations.

The mechanical properties have been investigated for chiral or helical films. Such research was primarily initiated upon the recognition of similarities between the film structures and the shape of a macroscopic spring. Helical SiO films have been analyzed by compression to reveal extremely high spring constants, partially due to the large bulk modulus of the materials [7]. Resonant structures are currently being designed using similar films with characteristic frequencies expected in the communications range of many MHz.

Finally, a new class of GLAD film can be produced that results in an inverse of the original structure by the addition of a dissimilar matrix material to the voids of the film. In this method the original film can be used as a mould whereby the structure of the film is passed on to the inverse structure after removal by chemical etching [62]. Applications of these films include fields such as optics [63], photonics [9] and sensing technologies [5] where the characteristic structure of the inverse film is that of a solid thin film with highly structured vertical pores.

2 Chapter 2

Square Spiral Photonic Band Gap Crystals

³In this chapter, the development of a new generation of three-dimensional photonic band gap crystal, the tetragonal square spiral photonic crystal, is presented. An overview of the theory of photonic band gaps and photonic band gap crystals and its effect on the production and design of periodic dielectric materials is highlighted in the context of the square spiral structure. The successful fabrication of a square spiral crystal is also demonstrated, showing the unique ability to fabricate highly structured porous thin films using the GLAD technique.

2.1 Introduction – Photonic band gap crystals

The influence of periodic structures on wave phenomena has been important in the design and implementation of most modern electronic and optical devices. Revolutionary work by scientists such as Bragg [64] and Brillouin [65] in the early 20th century focused study principally on mineral crystal structures as they provided a naturally occurring form of regular, regimented structure easily obtained with a variety of bases. Similarly today, most periodic structures, whether assembled naturally or synthetically, are referred to as crystals due to their regular compositional arrangement and their electronic and/or optical properties can be described using theory developed in such pioneering work. In the 1980's, a new species of crystal was envisioned with unique properties for photons that had never before been possible with traditional structures.

In 1984, investigation into Anderson localization of spin quantized particles [66] led S. John to the observation that photon localization could occur in three dimensions when elastic scattering occurred from a random distribution of sites with sample dimensions less than the mean free path for photon absorption [67]. Such localization

³ Portions of this chapter were excerpted with permission from [52] S. R. Kennedy, M. J. Brett, O. Toader, and S. John, "Fabrication of Tetragonal Square Spiral Photonic Crystals," *Nano Lett.*, vol. 2, pp. 59-62, 2002. Copyright 2002 American Chemical Society.

was found to occur near photon mobility edges of frequency ω^* , designated by the characteristic dimensions of the scattering sites, while in the long wavelength regime where the length scale of the scattering sites was much smaller than the wavelength, a typical λ^{-4} Rayleigh scattering behaviour was predicted. Following this work, in 1987 two papers were written addressing a similar issue of the reduction of propagating photon states in a carefully prepared dielectric superlattice, the first by John who examined photon localization for states satisfying Bragg resonance conditions [68] and the second by Yablonovitch whose interest lay in the suppression of spontaneous emission from excited particles whose energy states corresponded to frequencies lying in the forbidden photon bands of the dielectric crystal [69]. From these observations an analogy between photon states in a carefully constructed periodic dielectric lattice and electron states in a perfect semiconductor crystal lattice was drawn, enabling many of the theories and ideas developed in the past century for electronic semiconductor devices to be investigated in the context of photons. The resulting periodic dielectric structure that was the foundation of the development of these theories was identified as a photonic band gap (PBG) crystal for its regular structure and properties of restricted bands of propagation.

2.1.1 Applications of photonic crystals

The conceptual development of PBG crystals coincided with intense popularity in the fields of optical communications and optical computing. The ability of light to carry signals more efficiently than electricity on a twisted copper wire has led to an era of photonic fibres that can handle enormous amounts of information but whose efficiency is limited by the mandatory electronic switching, shaping and translation devices at the ends of networks. Due to the analogous properties of PBG crystals with electronic semiconductor devices, a revolutionary cure for the deficiencies of optical communication networks was foreseen as all-optical networks that did not require electronic components could be created using PBG devices. Similar to the electronic devices currently used for electrical signals, PBG-based devices could process the flow of photons. Although such devices still exist as the ultimate goal of PBG crystals, fabrication, characterization and development of theory for PBG crystals have proven to be difficult processes requiring a great deal of research and development.

PBG crystals exhibit a band gap, or a band of frequencies in which light is forbidden from propagating within the structure. Similarly to an intrinsic semiconductor, the usefulness of such a material lies not in the perfection of the crystal, but in discrete flaws or engineered defects that allow for useful devices to be constructed. In a fully three-dimensional photonic crystal (PC), a defect can be placed within the lattice with parameters allowing modes that are disallowed elsewhere in the crystal. If the defect is formed in a line, the light can propagate down its length without any loss, and even around sharp bends not possible with fibre waveguides [70]. This is one example of the potential applications of PC devices, low loss optical microcircuitry. Another application of engineered PCs is the suppression of parasitic spontaneous emission from solid-state lasers by the confinement of emission to a defect mode within the crystal. As all other modes are forbidden within the PBG material, emission can only occur for the specific defect mode lying within the band gap and can result in high efficiency, zero-threshold lasers [71]. Using PC-based materials, more complex devices have also been proposed such as optical transistors and optical diodes, demonstrating the potential of this new technology [72].

2.1.2 Photonic band gap theory

The analogy of PBG crystals to the characteristics of semiconductors allows for much of the theory developed in the past few decades for electronic devices to be used in the analysis of new PBG structures. As crystal band structures typically form part of the field of solid-state physics, many of the techniques for solving and analyzing band behaviour have roots in this field while the analysis of electromagnetic wave propagation is in the domain of optics. The two fields converge in the study of PBG materials with many aspects of both used in the development of this new field.

The propagation of light in a periodic PBG medium differs from electron travel in the periodic potential of a semiconductor crystal lattice as light obeys Maxwell's equations instead of the quantum mechanical derivation of Schrodinger's equation. This discrepancy results in one significant advantage for PCs as Maxwell's equations are linear and hold no dependency on dimensions thus allowing solutions to be scaled to arbitrary length scales and frequencies. Such scalability means that structures can be

modelled at any normalized length scale and subsequently fabricated with the appropriate dimensions for the spectrum of interest. Assuming the ability to fabricate the complex structure with arbitrary sized features, PCs can be produced to have their band gap tuned for wavelengths ranging from the ultraviolet to the microwave spectrum.

The theory required to accurately simulate a PBG material is based on Maxwell's equations and using numerical techniques it is possible to predict the behaviour of a given periodic dielectric medium. As light is a transverse wave, vector solutions must be obtained for the two orthogonal polarization modes, increasing the complexity of the calculations; however, several methods have been developed to produce accurate predictions of the band properties of PCs [73-77]. The most common solutions rely on harmonic Fourier plane wave solutions that result naturally from the periodic arrangement of the underlying structure.

In the procedure for numerical analysis summarized by Joannopoulos [78], and based on the initial theory by Ho *et al.* [73], the prediction of band structure results from solutions to eigenvalue problems derived from Maxwell's equations. The derivation is quite simple and will be presented briefly. The four equations in cgs units are,

$$\vec{\nabla} \cdot \vec{B} = 0 \quad (2.1a)$$

$$\vec{\nabla} \times \vec{E} + \frac{1}{c} \frac{\partial \vec{B}}{\partial t} = 0 \quad (2.1b)$$

$$\vec{\nabla} \cdot \vec{D} = 4\pi\rho \quad (2.1c)$$

$$\vec{\nabla} \times \vec{H} - \frac{1}{c} \frac{\partial \vec{D}}{\partial t} = \frac{4\pi}{c} \vec{j} \quad (2.1d)$$

where \vec{E} and \vec{H} are the electric and magnetic fields, \vec{D} and \vec{B} are the displacement and magnetic induction fields, ρ and \vec{j} are the free charges and currents, and c is the speed of light. As we desire a lossless medium at optical frequencies, we choose linear isotropic dielectric materials with purely real dielectric constants. The electric field is then related to the displacement field by

$$\vec{D}(\vec{r}, t) = \epsilon(\vec{r})\vec{E}(\vec{r}, t) \quad (2.2)$$

and we assume that the magnetic permeability is close to unity, giving

$$\vec{B}(\vec{r}, t) = \vec{H}(\vec{r}, t) \quad (2.3)$$

Also, as the materials are traditionally non conductive and we avoid any source charges ($\mathbf{J}, \rho=0$), we obtain the following equations,

$$\vec{\nabla} \cdot \vec{H}(\vec{r}, t) = 0 \quad (2.4a)$$

$$\vec{\nabla} \cdot \epsilon(\vec{r}) \vec{E}(\vec{r}, t) = 0 \quad (2.4b)$$

$$\vec{\nabla} \times \vec{E}(\vec{r}, t) + \frac{1}{c} \frac{\partial \vec{H}(\vec{r}, t)}{\partial t} = 0 \quad (2.4c)$$

$$\vec{\nabla} \times \vec{H}(\vec{r}, t) - \frac{\epsilon(\vec{r})}{c} \frac{\partial \vec{E}(\vec{r}, t)}{\partial t} = 0 \quad (2.4d)$$

By Fourier analysis of \mathbf{E} and \mathbf{H} due to the linearity of the above equations we can write,

$$\vec{H}(\vec{r}, t) = \vec{H}(\vec{r}) e^{i\omega t} \quad (2.5)$$

$$\vec{E}(\vec{r}, t) = \vec{E}(\vec{r}) e^{i\omega t} \quad (2.6)$$

to separate the time dependence from the space dependence. The above two divergence Equations, 2.4a and 2.4b, indicate that the wave solutions must be transverse in nature, and is a condition that must be imposed to obtain correct solutions. Using Equations 1.4c and 1.4d, an eigenvalue equation can be obtained for \mathbf{H} ,

$$\vec{\nabla} \times \left(\frac{1}{\epsilon(\vec{r})} \vec{\nabla} \times \vec{H}(\vec{r}) \right) = \left(\frac{\omega}{c} \right)^2 \vec{H}(\vec{r}) \quad (2.7)$$

We choose to work with the \mathbf{H} field eigenvalue problem as it is Hermitian and simplifies calculations, and from solutions for \mathbf{H} , the electric field, \mathbf{E} , can be obtained from

$$\vec{E}(\vec{r}) = \left(\frac{-ic}{\omega \epsilon(\vec{r})} \right) \vec{\nabla} \times \vec{H}(\vec{r}) \quad (2.8)$$

Note that all of the information pertaining to the periodic dielectric structure is contained in the periodic dielectric function $\epsilon(\mathbf{r})$, and is the functional representation of the crystal structure. We must assume at this point that the crystal is perfect, that is, it is uniform in all directions, is without dislocations, defects or finite boundaries, and can be represented by an irreducible, repeated Wigner-Seitz cell. For calculations of modes near crystal defects, a much more intensive calculation must be performed involving processes set out in the finite-difference time-domain method [79]. Assuming that the crystal is periodic in all three dimensions, Bloch's theorem, most commonly seen in solid-state physics, can be employed and the \mathbf{H} field can be expanded into plane waves

$$\vec{H}(\vec{r}) = \sum_{\mathbf{G}} \sum_{\lambda=1}^2 h_{(\vec{G},\lambda)} \hat{e}_{\lambda} e^{i(\vec{k}+\vec{G})\vec{r}} \quad (2.9)$$

where \mathbf{k} is a wave vector in the Brillouin zone of the lattice, \mathbf{G} is a reciprocal-lattice vector, and \hat{e}_1 and \hat{e}_2 are unit vectors perpendicular to $\mathbf{k}+\mathbf{G}$ because of the transverse nature of \mathbf{E} and \mathbf{H} . From Equations 2.7 and 2.9, the resulting matrix eigenvalue problem has the form

$$\sum_{(\vec{G},\lambda)} \Theta_{(\vec{G},\lambda),(\vec{G}',\lambda')}^{\vec{k}} h_{(\vec{G}',\lambda')} = \left(\frac{\omega}{c}\right)^2 h_{(\vec{G},\lambda)} \quad (2.10)$$

with eigenvalues proportional to the square of the mode angular frequency, ω , where the matrix Θ is defined by

$$\Theta_{(\vec{G},\lambda),(\vec{G}',\lambda')}^{\vec{k}} = [(\vec{k} + \vec{G}) \times \hat{e}_{\lambda}] \cdot [(\vec{k} + \vec{G}') \times \hat{e}_{\lambda'}] \epsilon^{-1}(\vec{G} - \vec{G}') \quad (2.11)$$

and $\epsilon^{-1}(\mathbf{G}-\mathbf{G}')$ is the inverse of the Fourier transform of the dielectric function, $\epsilon(\mathbf{r})$. The matrix Equation 2.10 is solved numerically to find the mode frequencies, ω , as a function of the wavevector \mathbf{k} , indicating allowed and disallowed frequency bands of the PBG. Several techniques have been developed to speed convergence of this process, the most notable is to perform the Fourier transform of the dielectric function first before truncating and inverting it [77].

Upon inspection of the solution obtained in the above discussion and reviving the analogy of PCs to semiconductor crystals, it is natural to plot the solutions to

electromagnetic modes of a PBG crystal in a reduced zone scheme band diagram similar to that used to represent electron bands in a crystal lattice. Like atomic crystals, the crystal structure of a PBG material can be represented by its reciprocal Brillouin lattice with associated Brillouin zones in inverse space. Implementing this technique allows the efficient plotting of wavevectors, making the analogy between the two similar structures complete (notwithstanding the discrepancy in size scale that is on the order of 1000 times larger for PBGs in the visible spectrum). Shown in Figure 2.1 are examples of the band structure for a square spiral PC structure and one of the original calculated electronic band structures for the diamond-based silicon crystal lattice, for comparison.

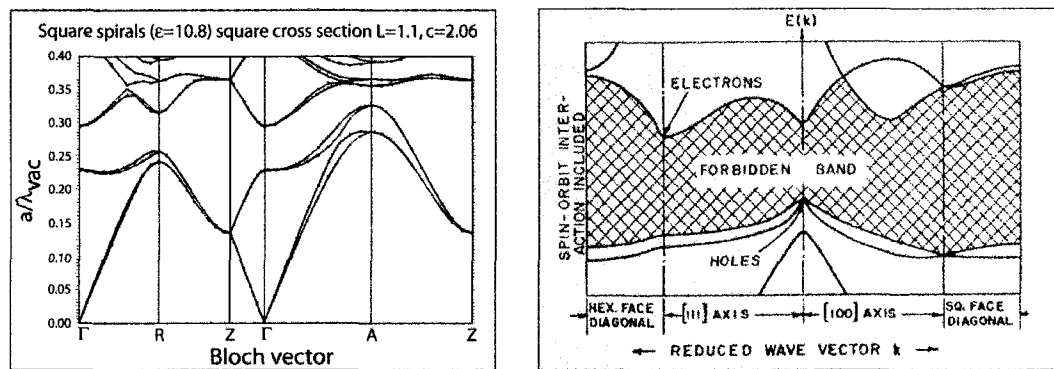


Figure 2.1 – Examples of photonic and electronic band structures for a silicon square spiral photonic crystal, left, and for the diamond lattice arrangement of silicon atoms, right [80]. The similarities between the two representations help cement the analogy between the two types of crystal structures.

To better understand the characteristics of fabricated crystals and in an attempt to optimize the thin film nanostructure, numerical simulations of PBG crystals were performed in collaboration with Sajeev John and Ovidiu Toader of the Department of Physics at the University of Toronto. All of the simulated band structures used in this thesis have been provided by S. John and O. Toader and result from their custom software. By working in close collaboration it was possible in several iterations to find a balance between the development of the optimal crystal morphology from theory, and the constraints imposed by the real-world fabrication processes.

2.1.3 Photonic crystal dimensionality

As with most complex structures, the intricacy of a fully three-dimensional crystal can be reduced to two or even a single dimension to help analyze the underlying physics. Ultimately, it is most desirable to fabricate PC structures with full three-dimensional band gaps; however, by reducing the problem to a single dimension, it is easier to understand the effects that contribute to the production of a band gap. By stacking slabs of alternating dielectric materials on top of each other, a one-dimensional PC can be produced that is simply a multi-layer half-wave film stack seen most commonly in the high reflectivity surfaces of many Fabry-Perot etalons. Interference of scattered waves from the film interfaces for light incident normal to the surface results in extremely high reflectivity values when the wavelength satisfies Bragg resonance conditions. Inside the film layers standing waves are produced which forbid propagation of the light and result in a band gap of disallowed frequencies. This filtering property of alternating dielectric layers is very well known [14], and is the basis for the optical properties of PCs with higher dimensionality. Two and three-dimensional PCs can be fabricated when the alternating dielectric layers are carefully arranged with two and three-dimensional symmetry respectively. As shown in the schematic of Figure 2.2, although the complexity of the structure increases, the optical effects responsible for the properties of PBG crystals with higher order are identical in all cases.

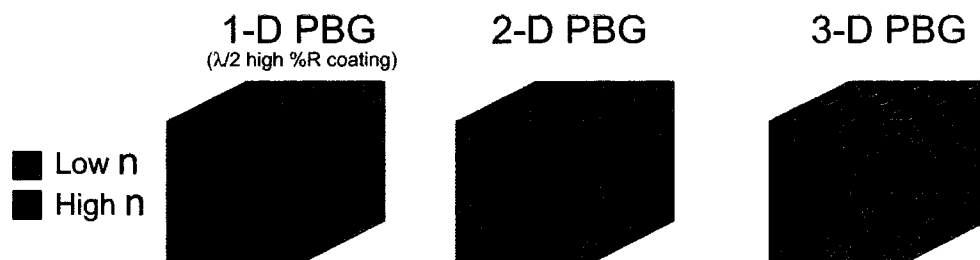


Figure 2.2 – Representative examples of the alternating high/low index of refraction materials needed to produce a one, two and three-dimensional PBG crystal. In one dimension the structure is a stack of layers or films, while in two and three-dimensions, to obtain full band gaps, the structures becomes much more complex. Adapted from [78].

2.1.4 Photonic band gap edges

For frequencies lying at the edges of a PBG, the modes appear as standing waves within the alternating structure. If the dielectric materials are chosen in such a way that they have contrasting optical properties characterized by a significant difference in refractive indices, a band gap will emerge. At the lower energy edge of the gap the electric field oscillations are found to be concentrated in the material of higher index of refraction while the high frequency mode above the gap is found to concentrate its energy in the material with the lower index. The lower index material is often chosen to be air due to its lowest possible index of unity. Consequently, the two bands which lie above and below the gap are known as the air band and the dielectric band respectively, in analogy to the conduction and valence bands of a semiconductor band structure. Results of numerical simulations can be seen in Figure 2.3 where a two-dimensional photonic crystal with a fundamental gap shows concentration of the displacement field in two distinct regions for the modes below and above the gap.

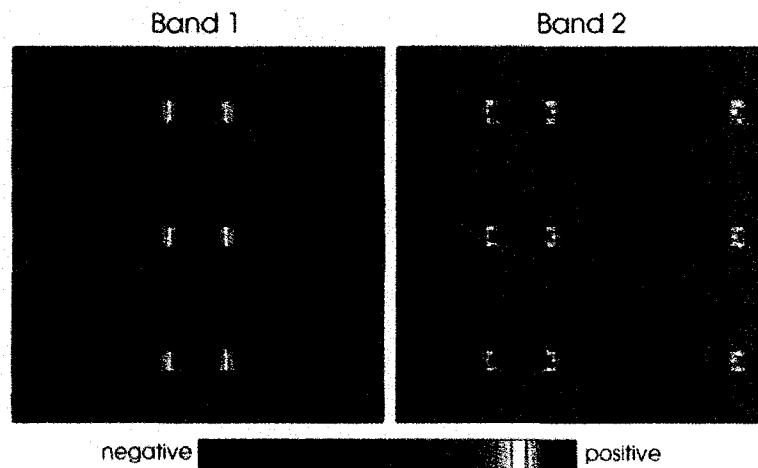


Figure 2.3 – The electric field of the lower energy dielectric band edge is concentrated in the high ϵ material (left), while for the higher energy air band edge the electric field is principally located in the regions associated with the air gaps of lower ϵ (right). From Joannopoulos [78].

2.1.5 Photonic crystal materials

The requirement of a large PBG relies on the properties of the materials chosen to form the alternating medium. From electron theory, a large gap results from crystals of

atoms with a high electron affinity or a larger periodic potential difference. In analogy to this result, the size of the photonic band gap in a PC is highly dependent on the index of refraction or dielectric constant of the materials, specifically the contrast between the two different species. Although the resulting band structure is also highly reliant on the physical crystal structure, the existence of a band gap requires a minimum contrast ratio defined by

$$n_c = \frac{n_h}{n_l} = \frac{\sqrt{\epsilon_h}}{\sqrt{\epsilon_l}} \quad (2.12)$$

where the subscripts ‘*h*’ and ‘*l*’ represent the high and low values for the appropriate materials used. Typically, index contrast ratios must be greater than approximately 2.1 for a PBG to emerge in a suitable PC structure [8, 81]. As mentioned earlier, it is desirable to use lossless materials for the frequencies near the designed PBG and dielectrics such as silicon, GaAs, and TiO₂ are often chosen to serve as the high dielectric material in the visible and near infrared (NIR) spectrums. Air, with an index of refraction of unity, is the material most often chosen as the low dielectric material, however, the difficulty in processing highly porous structures filled with a large concentration of air gaps makes many fabrication processes ineffective.

2.1.6 Three-dimensional photonic crystal structures

The requirement of complete, three-dimensional periodicity for a full, three-dimensional band gap requires a highly complex crystal structure. Ideally, the crystal should be symmetrical and identical regardless of the direction from which it is viewed. In terms of the common inverse space representation, the most desirable structures should have nearly spherical Brillouin zones so that the gaps arising in all directions coincide in frequency. The most common structures with large band gaps are the simple cubic, the FCC, and the most optimal among all known structures, the diamond lattice [82]. As the diamond structure is known to produce the largest band gaps, many attempts have been made to represent its complex assembly with macroscopic arrangements of material. Unlike the natural formation of atoms that coalesce into their lowest energy states and result in the tetrahedral bonding network of a diamond lattice, PBG structures are on a

much larger scale and must rely on structural members to interconnect and support the many sites of the diamond lattice. The principle issue with a macroscopic diamond structure, aside from arrangement of the material, is the fill factor, f , of the lattice, or the ratio of solid, high n material to the entire volume of the crystal. A critical balance between the nanostructural form and the fill factor must be struck to allow for the formation of standing waves within the given dimensions of the device. For Si/Air PCs, a fill factor of approximately 1/3 is required to account for the high index contrast.

2.1.7 Classes of three-dimensional photonic band gap structures

Many methods have been employed in the pursuit of fabricating PCs with band gaps in the visible or NIR spectrum. To a first-order approximation, the structure sizes required to produce a PBG centred at the vacuum wavelength λ_c is one half of the centre wavelength, or $\lambda_c/2$. Thus for structures with a band gap in the visible spectrum, the feature sizes should be on the order of a few hundred nanometres, requiring microfabrication tools and processes for their production. Four classes of three-dimensional photonic crystal structures have emerged that can be fabricated on the appropriate size scales and have been shown to provide a three-dimensional band gap: the Yablonovitch-Gmitter-Leung (YGL) structure, the woodpile structure, the inverse opal structure, and finally, the tetragonal square spiral structure, which is the newest structure and the topic of this research.

2.1.7.1 Yablonovitch-Gmitter-Leung structure

The YGL structure is based on an FCC lattice, the parent to the optimal diamond structure, and generally uses microfabrication processing to produce its complex structure. The principle behind its design is the placement of air ‘atoms’ in an FCC arrangement with a background of high index semiconductor such as silicon or GaAs [71, 81]. This structure is fabricated by careful lithography and precise drilling with reactive ion etching at specific angles along the $\langle 110 \rangle$ directions as shown in Figure 2.4 [83, 84]. As this process is performed from the top down, very few periods can be produced, many processing steps are required, and the lithography and etching orientation must be

extremely accurate. PBG widths of up to 20% of the centre frequency have been predicted for GaAs YGL structures.

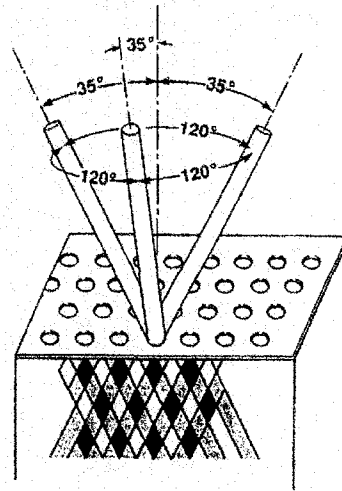


Figure 2.4 – The Yablonovitch-Gmitter-Leung (YGL) structure is fabricated by etching through a mask of hexagonally arranged pores at specific angles. The etching process must be highly anisotropic and the orientation of the channels accurately positioned. From Yablonovitch et al. [81].

2.1.7.2 The woodpile structure

The second class of three-dimensional PC, the woodpile structure, is based on the more favourable diamond lattice. Again employing intensive microfabrication processing, this structure is composed of alternating layers of crisscrossing rods with every second layer having a phase shift of one half a period over the previous layer of rods with parallel orientation. With carefully chosen geometries, the rods represent the tetragonal bonding network of a diamond lattice and are predicted to result in relative PBGs of up to 28% for Si in an air background [85, 86]. Shown in Figure 2.5 is an example of the woodpile structure fabricated by repeated lithography, etching, wafer alignment and fusion. The difficulties with the fabrication of woodpile PCs result from the careful control required over alignment, lithography and processing. In addition to the technical difficulties of fabrication, the process is extremely time-consuming requiring the production of four separate layers to obtain a thickness corresponding to a single unit cell.

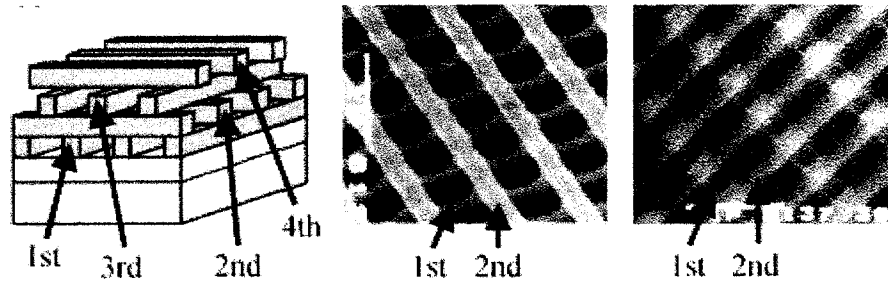


Figure 2.5 – Example of the woodpile structure fabricated through multi-step lithography and selective etching processes. Four layers are required to form a single lattice period. From Noda et al. [87].

2.1.7.3 Inverse opals

The third class of PC is the inverse opal structure that relies on self-assembly of spheres of a sacrificial material [88]. To fabricate such PCs, SiO_2 spheres are placed in suspension and slowly made to agglomerate into a close-packed FCC arrangement. Sintering of the array is then performed, causing the spheres to form necks at their contact points. This step is followed by deposition of a high dielectric material such as silicon by LPCVD into the voids of the structure, and finally the original template is removed by wet etching [89, 90]. The difficulty with this process lies in the potential for dislocations, vacancies or interstitial spheres to destroy the natural symmetry and propagate disorder throughout the crystal. Typically only very small crystal grains can be formed that are free of defects. Examples of both the original opal and the Si infiltrated inverse opal structure are shown in Figure 2.6 where the inverse structure is predicted to produce relative band gaps of up to 15% for Si or Ge in air.

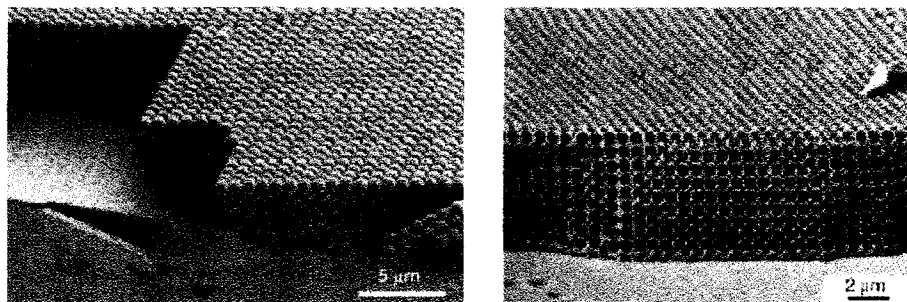


Figure 2.6 – Self assembled PC structures. The left figure is of an opal assembly of SiO_2 spheres and the right is of an inverse opal fabricated by infiltration of silicon and removal of the sphere template. From Vlasov et al. [91].

2.1.7.4 Square spirals

The fourth class of structure and the focus of this research is the tetragonal square spiral PC that will be described in the following sections. This new and innovative structure can be easily fabricated and is capable of producing large, tuneable three-dimensional band gaps superior in many ways to the structures mentioned above.

2.2 Tetragonal square spiral photonic crystals

Spiral symmetry was first observed in well-known PBG lattices by Chutinan and Noda where helical structures were found that connected the lattice sites of a simple cubic, FCC, diamond, or BCC lattice [92]. Depending on the connection scheme that determined the spiral radius, pitch, and phase, helices of high dielectric material arranged in regular arrays were found to produce large three-dimensional band gap PCs. For the diamond, FCC, and BCC lattices, the most desirable crystal structures, circular spirals are required to be phase shifted from their adjacent neighbours by one half period so that the interconnection forms the appropriate three-dimensional periodicity of the parent lattice. By implementing these structures, relative band gaps of up to 17% were predicted for Si spirals in an air background with fill factors of approximately 20%.

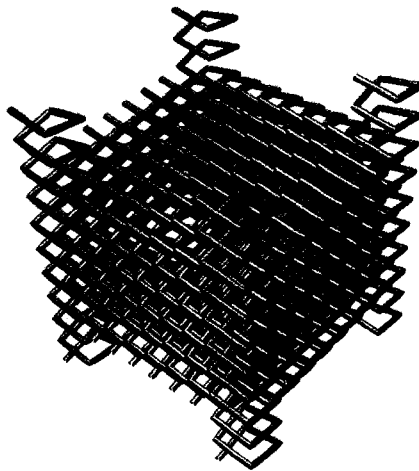


Figure 2.7 – Computer generated representation of the tetragonal square spiral photonic crystal structure. The staircase-like, high dielectric structures are interwoven to produce a full three-dimensionally periodic crystal lattice with favourable band properties. From Toader [9].

One complication with the circular spiral PC design, however, was that the non-uniformity of the structure due to the mandatory phase shift between neighbouring spirals makes fabrication extremely difficult. Foreseeing this problem, Toader and John first described a revolutionary new crystal structure composed of interwoven square-sided spirals and shown in Figure 2.7. When arranged in a tetragonal array, this structure avoided the requirement of phase shifts between adjacent spirals while providing extremely large band gaps [8, 9]. The advantages of the tetragonal square spiral PCs over other PBG structures are that they can be fabricated using GLAD oblique deposition techniques in a virtual single step, they are compatible with many micromachining and microfabrication techniques, they provide large, robust band gaps that are relatively insensitive to nanostructural variations, and they can easily incorporate engineered defects for device fabrication.

2.2.1 Diamond and FCC lattice mapping

Similar to the circular spiral PCs proposed by Chutinan and Noda, tetragonal square spirals create a periodic three-dimensional crystal by mapping out the lattice sites of FCC and diamond structures with high dielectric material. For the square spiral nanostructure, the abrupt corners are arranged to coincide with the atomic placement of the parent lattice, although it has been found that larger relative band gaps can be formed when the placement of the corners is allowed to deviate subtly from the traditional lattice sites [8]. To map either the FCC or the diamond lattice, a particular plane is first chosen whose normal forms the orientation of the spirals' central axes. Typically the (001) plane is used where the vertical z axis forms the direction of thin film growth and is the principal axis of the helical nanostructure. The connection of the lattice points then determines the square spiral structure, where typically the 1st, 3rd or 5th nearest neighbour connections are used. Using nomenclature developed for this novel PC structure, the crystals are labelled by $[\mathbf{m}_1\mathbf{m}_2\mathbf{m}_3]\text{-3Dlattice}:n$ where $[\mathbf{m}_1\mathbf{m}_2\mathbf{m}_3]$ denotes the orientation of the z axis normal to the crystallographic plane $(\mathbf{m}_1\mathbf{m}_2\mathbf{m}_3)$ of the substrate, n is the order of the neighbour connection (1, 3 or 5), and the 3D lattice can be either the diamond or the FCC type. Shown in Figure 2.8 is an example of the mapping of the diamond lattice by a **[001]-diamond:5** square spiral. When arranged in the regular tetragonal array of the

dashed lines of Figure 2.8b with spacing a , these polygonal spirals can completely map the diamond lattice, and provide a large PBG that has been shown from simulation to be very robust with respect to disorder effects [8].

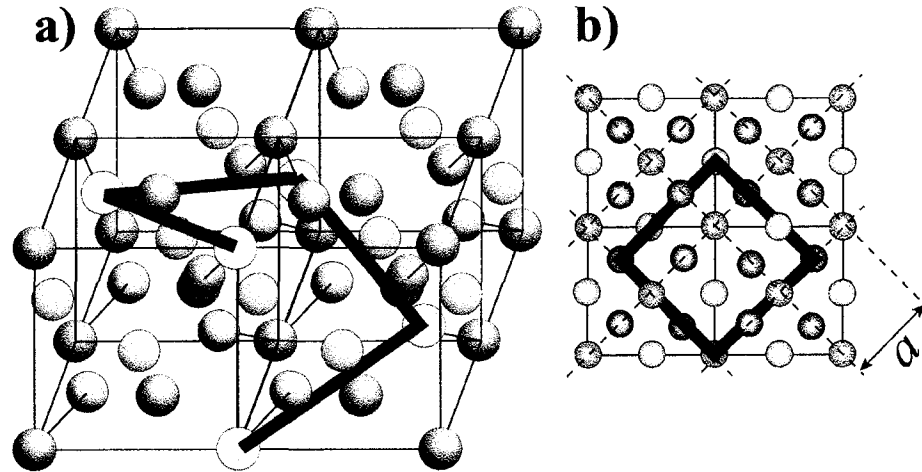


Figure 2.8 – a) A diamond lattice with each layer of lattice sites above the (001) plane shown in a different colour. The highlighted spiral demonstrates the geometry of a square spiral with $n=5$ connections. b) Looking down on the lattice in the [00-1] direction, the tetragonal array of lattice points from which each of the square spirals evolves can be seen.

2.2.2 Square spiral structure parameters.

The details of the individual square spirals that make up the periodic PC can be seen in Figure 2.9 where both a computer-generated (CG) and a fabricated silicon spiral are shown for comparison. The nanostructure of the square spiral is composed of inclined arms placed at right azimuthal angles to each other, wrapping around the central z axis. The corners corresponding to each turn serve as the lattice ‘sites’ in the assembled crystal. The individual spirals are completely parameterized by the triplet $[L,c,e]$, where L represents the spiral width in the xy plane, c represents the vertical pitch or height of one complete turn, and e denotes the cross-sectional width of the spiral arms. These values are mapped onto the figure of the CG spiral and are normalized to the lattice spacing or distance between adjacent spirals, a . Through normalization, the crystal properties can be generalized to any wavelength regime assuming little or no change in the dielectric constant of the material.

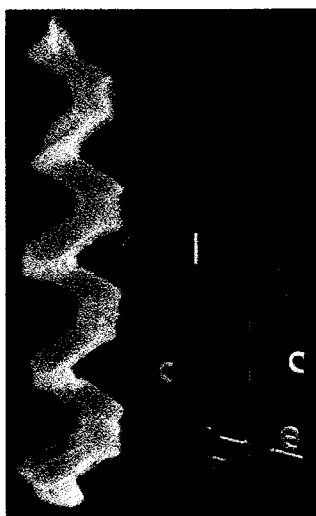


Figure 2.9 – Ideal, computer generated square spiral and an actual, fabricated silicon spiral viewed using the scanning electron microscope. The structure of the fabricated spiral is very close to the ideal shape.

One important parameter of the PC is the fill factor, f , which must be in a certain range for a given material and crystal structure to allow the proper phase delay across each unit cell. For silicon structures in an air background, values for f of 20 to 40% provide the optimal balance between the two mediums and as will be seen for GLAD films, this range conforms well to the natural density of the deposited porous films. When structures are fabricated with porosities outside of this range, the band gap is eliminated regardless of the precision of the spiral shape, demonstrating the importance of both the micro- and the macroscopic properties of the crystal.

For the direct square spiral structure, a maximum relative band gap of approximately 16% has been predicted for Si spirals in an air background and can be easily fabricated using the GLAD thin film deposition technique. Another related structure, the inverse square spiral, has also been proposed where the spiral structures are inverted to form tailored pores in a high dielectric background matrix. Extremely large band gaps of up to 24% have been predicted for this modified square spiral PC [8]. The advantage of the inverse structure is that the original template can also be easily fabricated with suitable materials such as SiO_2 using GLAD. After fabrication of a sacrificial spiral crystal, silicon can be deposited into the porous film and the original template removed by material selective wet chemical etching [62]. Again the fill factor is an important parameter in the fabrication of the inverse square spiral structure, and by

inverting a standard $f=35\%$ crystal, the result is an $f=65\%$ structure. Appropriate changes to the film density must be made to the original template to accommodate the inversion process and one potential solution is presented in the next chapter.

2.3 Fabrication of square spiral photonic crystals

The fabrication of a tetragonal square spiral PC requires the uniform assembly of a series of slanted arms placed at 90° to the previous growth orientation, relative to the substrate normal. As seen in chapter 1, the most elementary form of structure deposited using the GLAD technique is the slanted post morphology, making this deposition process a natural candidate for fabrication of these more complex devices. Another feature of GLAD that makes it suitable for PBG applications is the density of porous thin films deposited in the GLAD regime with α from 80 to 90° , is approximately 30 to 40% and results in fill factors close to the ideal range. Without this compatibility, the process would not be effective as the appropriate structural parameters of a candidate PC structure could not be obtained.

A three-dimensional square spiral PC must also have periodicity in all dimensions to obtain a full band gap. To accomplish this requires not only the correct fabrication of specifically shaped nanostructures, but also the particular arrangement of spirals in a tetragonal array. Using the mechanism of self-shadowing, the selective growth at specified locations can be easily obtained through the use of pre-patterned or seeded substrates.

2.3.1 Substrate seeding

In many applications of GLAD, including the production of PBG materials, it is desirable to restrict growth of the individual structures to specified locations on the substrate. As the deposition process blankets the entire substrate surface, the most obvious means of confining growth is to mask the areas where deposition of the material is not desired. This technique is impractical, however, as the mask must have a finite height, the mask could become plugged with deposited material, and the minimum feature size is limited to dimensions much greater than those required for most PC

devices. For GLAD thin films deposited at highly oblique angles of incidence and with average column sizes on the order of a few hundred nanometres, a seeding technique is used that takes advantage of the natural self-shadowing critical to the process [93-95]. During initial growth of an aperiodic GLAD film, the random impingement of atoms onto the substrate and the subsequent formation of critical nuclei determines the growth locations due to shadowing restrictions imposed by forming islands. For a film with periodically arranged structures, instead of allowing the growth to be determined randomly, a series of relief features are placed on the substrate before deposition to impose shadowing restrictions. The lower regions that are engulfed in the shadow of the higher topography receive little or no flux and thus growth is restricted to only the higher regions. This mechanism is shown in Figure 2.10 where the array of square seeds receives all of the flux and results in structures placed at regular intervals along the substrate surface. An example of seeding is shown in Figure 2.11 where square seeds have been used to grow an array of slanted posts.

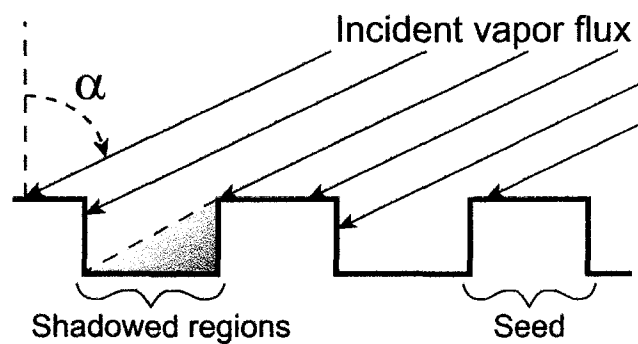


Figure 2.10 – Deposition on a pre-seeded substrate with specific topography imposes shadowing at highly oblique angles of incidence. The seeds are the only portion of the substrate to receive flux and hence the nanostructures are grown uniquely in those regions.

A wide variety of methods can be used to obtain the appropriate topography on the substrate surface for periodic GLAD structures. As the exact shape of the relief structures is not as critical as the aspect ratio, the size limits of most processes can be pushed to their lowest values provided the resulting seeds are high enough to shadow the region between them. Some of the more common methods of obtaining topography are electron beam lithography [93], photolithography, laser interference lithography [96] and plastic embossing [94]. The lower size limit of the seeds is limited by the adatom

diffusion length and is highly dependent on deposition parameters such as substrate temperature and deposition material. If the seeds are too small and are brought too close together, competition among adjacent structures and adatom mobility destroys the shadowing effect and results in the loss of periodicity.

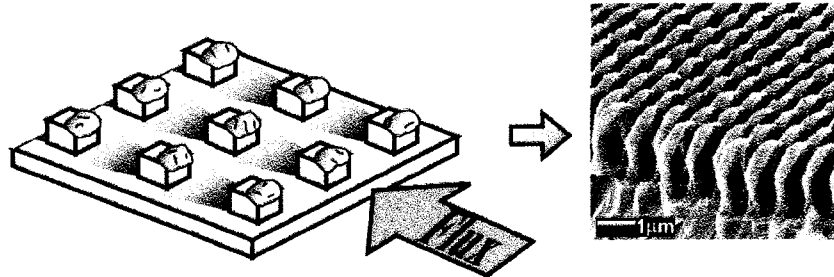


Figure 2.11 – Growth of slanted posts on a seeded substrate. As can be seen on the right in the SEM of the fabricated film, the structures are accurately located at the seed sites.

In the development of GLAD-based photonic crystals, photolithography was most commonly used to produce seed topographies due to its simplicity, reproducibility and its ability to provide regular arrays of seeds over areas large enough for optical characterization. This latter issue is the current limiting factor in the use of electron beam lithography for the production of topography for GLAD PBG structures even though it does offer the capability of producing much smaller features that would correspond to PCs in the visible spectrum. To produce the square array of seeds for tetragonal square spirals, a mask was fabricated with 500 nm square dots on a square lattice with periodicity $a=1 \mu\text{m}$. Silicon wafers were used as substrates and to allow for a greater seed aspect ratio, 500 nm of Si_3N_4 was first deposited by CVD onto the substrates before spinning on photoresist for photolithography processing. To fabricate the seeds, OCG HPR 504⁴ positive photoresist was spun to a thickness of approximately 1.2 μm and UV exposed through the contact mask for 1.2 s before being developed for 7 s in Shipley 354⁵ developer. As the spacing of the seeds was too small for accurate reproduction of the mask by the photoresist, reactive ion etching with an oxygen plasma was performed on the wafers to reduce the overall size of the seeds by isotropically removing a portion of the photoresist. Finally, to increase the aspect ratio of the seeds (i.e. the height-to-width

⁴ OCG Microelectronic Materials, 2070 Zwijndrecht, Belgium

⁵ Shipley Company L. L. C., www.shipley.com

ratio), an anisotropic reactive ion etch of the Si_3N_4 underlayer was performed, producing thermally stable structures with heights of approximately 400 nm. The resulting seed topography can be seen in

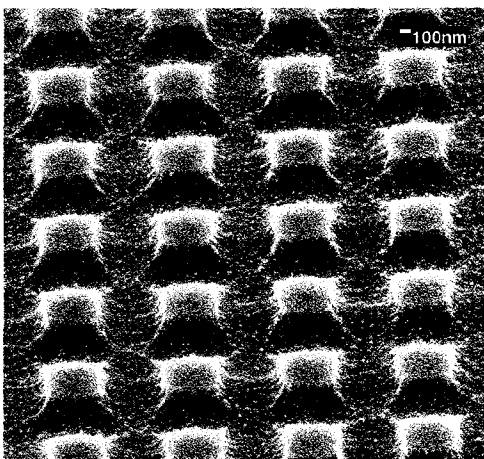


Figure 2.12 – SEM of a square array of 500 nm seeds. The seeds are fabricated using photolithography and to increase their aspect ratio an anisotropic reactive ion etch is used.

Figures 2.12 and 2.13 where both SEM and tapping mode AFM images of the relief structures are seen.

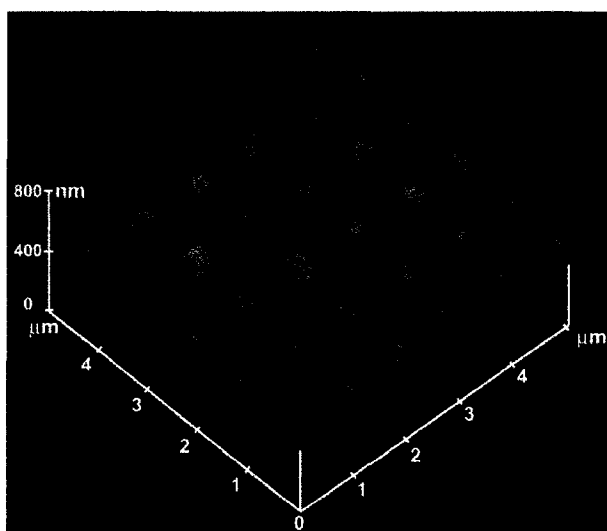


Figure 2.13 – Tapping mode AFM scan of the Si_3N_4 seeds. The seeds are approximately 400 nm high, 500 nm wide, and have a periodicity of 1000 nm.

The restriction of growth to the desired topography is an extremely powerful tool in the fabrication of GLAD thin films and can be used to severely restrict the shape of the

nanostructures. Shown in Figure 2.14 is an example of the growth confinement imposed on GLAD structures where 1 μm lettering used to identify the photolithography mask has served to confine growth of a slanted post film. The lettering patterned simultaneously onto the Si_3N_4 substrate with the square array of topography from above is accurately reproduced by the film structures even at this small size scale.

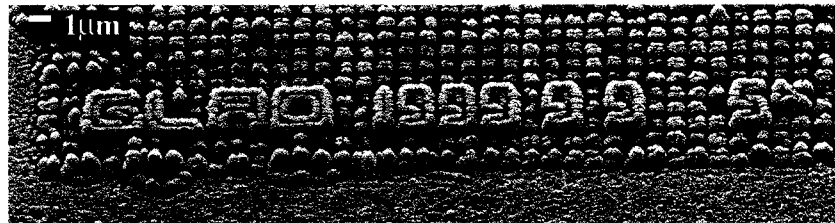


Figure 2.14 – 1 μm tall words written in a GLAD film by a pre-patterned substrate. The conformity of the film to the words is extremely good, showing very small feature sizes.

2.3.2 Tetragonal square spiral photonic crystals

To successfully fabricate a tetragonal square spiral PC structure, uniform, individual square spirals with appropriate dimensions must be produced in a regular, square array. As shown above, the two-dimensional constraint on growth in the plane of the substrate is easily obtained through the use of pre-seeded substrates with lattice spacing, a . To grow the appropriate polygonal spirals, however, involves the implementation of GLAD control algorithms.

As an individual square spiral is composed of a series of slanted posts with specific orientations, the basis of the most elementary fabrication of a square spiral PC by GLAD is rooted in this nanostructure. The production of a square spiral film involves the sequential deposition of slanted posts at right angles to the previous growth direction. Individual slanted posts are produced when the substrate is fixed with flux incident at approximately 80 to 90° from normal. As the orientation of the porous thin film structures track the apparent location of the source around the substrate, square spirals can be created by rotating the substrate abruptly by 90° at regular, fixed intervals during the deposition. A quartz crystal thickness monitor provides feedback of the deposited thickness so that deposition rate variations do not affect the nanostructure dimensions and

the substrate is rotated only after the specified thickness, equal to one quarter of the pitch, is reached.

The angle of incidence, which is held constant for the most basic square spiral fabrication, is typically set in the range from 84 to 85°, as for this geometry the density of the film is close to the desired value of 1/3 for the direct structure (other techniques are required for the fabrication of the template for inverse structure), individual structures can be formed, and the cosine dependence of vertical growth on deposition rate is still reasonable so that total deposition time is limited to a few hours. Typical column inclination angles, β , for these structures are approximately 55 to 60°. Depending on the vertical pitch of the spiral this results in values of L given by

$$L = \frac{c}{4 \tan(90 - \beta)} \quad (2.13)$$

Ignoring third nearest neighbour connections corresponding to the diamond lattice sites, $n=3$, as they do not provide large band gaps, the dependence of L on β restricts the type of structures produced. For an ideal diamond-based structure with $n=1$, β should equal 54.7° while for an $n=5$ structure β must have a much greater value of 76.7°. Using conventional GLAD fabrication techniques this latter highly oblique structure is not obtainable and thus only the fabrication of $n=1$ square spiral PCs is allowed.

For the original proposed tetragonal square spiral structure, the arms were simulated with circular cross-sections, however, the GLAD deposition process in its most basic and unoptimized form is much more suited to fabrication of spiral arms with square cross-sections. Theoretical simulations of fabricated spirals with square cross-sections yield large, three-dimensional band gaps, but with centre frequencies shifted to lower values from their counterpart ideal structures due to the larger fill factor of the modified spiral structure. For spirals with ideal circular arms, the parameter used to specify the radius of the circular cross-section is r , while for spiral arms with a square cross-section this parameter is replaced by the square side length, e . Simulations of arms with rectangular cross-sections have also been performed showing a maximum band gap for non-uniform structures with the arm height approximately 1.2 times its width [8].

The size of the arm cross-section for structures fabricated with normalized dimension e , is a function of the film density through the deposition angle, and of the lattice constant, a . As a denser film results when deposited at a less oblique angle of incidence, the cross-section of the spiral arms will increase accordingly. Similarly, the lattice spacing constrained by the substrate seed spacing can have a direct effect on the cross-section as the total areal density of the films is constant at a fixed angle of incidence. For smaller seeds placed closer together the cross section will be reduced, while increasing a will increase the cross-section. As the value e is normalized to the lattice period, its value might not change with a , however, the other dimensions of the spiral structure, L and c , are mostly independent of the cross-section and can be different in these two cases, resulting in a significantly different crystal.

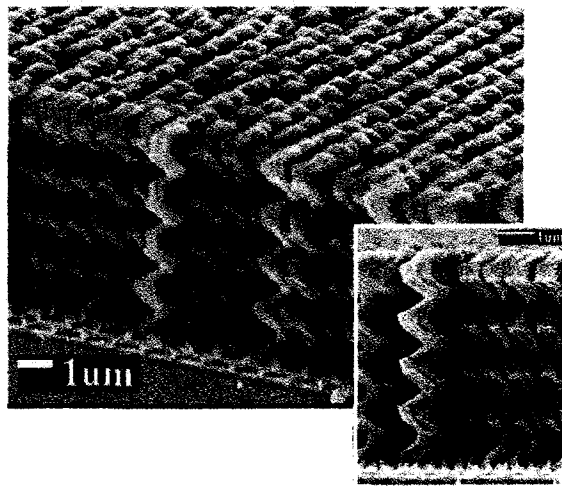


Figure 2.15 – Oblique and edge views of a tetragonal square spiral PC structure grown on a photolithography-patterned wafer.

Shown in Figure 2.15 is an example of a GLAD silicon square spiral PC structure deposited on a patterned wafer with $a = 1000$ nm. From the scanning electron micrograph it can be seen that the structure of the film is that of a series of square spiral staircases placed regularly across the substrate and the interweaving helical arms form a regular array of periodic dielectric material. Theoretical analysis by O. Toader and S. John of this structure indicates a full, three-dimensional relative band gap of 9.3% for this unoptimized film with $[L,c,e]=[0.70,1.3,0.44]$ [8, 73]. The calculated reduced zone band diagram is shown in Figure 2.16 with the inset indicating the principle directions of the

irreducible Brillouin zone. This calculation does not reflect the nanoscopic surface roughness characteristic of the deposited films, and although this property of fabricated films is predicted to reduce both transmission and reflection through diffuse scattering, the effect of such disorder on the resulting photonic bands is small in comparison to other classes of fabricated PBG structures [8].

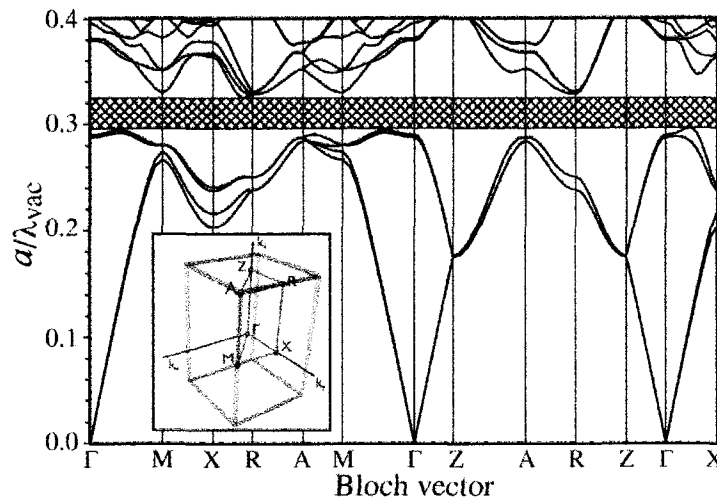


Figure 2.16 – Calculated band diagram for the square spiral photonic crystal of Figure 2.15. A full, three-dimensional band gap of 9.3% is predicted and is shown by the cross-hatched area.

2.3.3 Advantages of GLAD square spiral photonic crystals

The implementation of GLAD in the production of square spiral PCs allows for a large degree of versatility and improvement over the simple, first-generation square spirals. If these crystals are to be developed for small- to large-scale production, the major question that arises in their application is in regards to the limits to the size scales of square spiral PC devices. The band gap centre frequency is easily tuneable through the variation of both the nanostructural parameters and the characteristic lattice spacing of the substrate seeding, however the stability of the growth process must be such that many layers or several lattice periods can be deposited on the substrate without degrading the properties of the crystal. In traditional, aperiodic or random GLAD deposition, competition among columns causes the extinction of a large portion of the growths and the subsequent broadening of the surviving structures. In PC applications, such behaviour would destroy the properties of the crystal. However, for seeded, or periodic

GLAD, this effect can be virtually eliminated by the appropriate choice of seed sizes and spacing [97]. To demonstrate the stability of the growth process, a 16 turn, 22.4 μm thick square spiral PC was fabricated using the slow corner technique described in the next chapter. From Figure 2.17 showing the extremely thick structured silicon film, it can be noted that the spirals are very uniform throughout the entire crystal. The cleaving process has damaged some of the fragile spirals causing them to break or lean up against their neighbours, however the film was found to be uniform across most of the patterned area of the substrate. It has been shown that only four to five periods of a PC are all that are typically required for near elimination of the density of states within the band gap [98], making GLAD highly useful in the production of stacked devices with complex architecture.

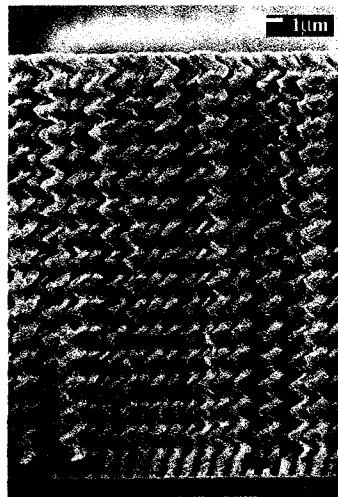


Figure 2.17 – A 22.4 μm thick square spiral film. Although several of the long spirals have been damaged in the cleaving process for SEM preparation, the regularity, order and uniformity of the spirals can be seen throughout the thickness of the film.

The compatibility of GLAD structures with many traditional processing techniques also lends the fabrication of square spiral PCs to implementation in complex devices. Recently, a hybrid 2D/3D device hierarchy has been proposed based uniquely on the GLAD process of fabrication [99]. By depositing solid capping layers directly on top of a three-dimensional PC, it is possible to create planar, two-dimensional band gap structures with simple microcircuitry and cavities that can be patterned using standard lithographic and etching techniques. Subsequent deposition of another 3D square spiral

PC on top of the planar layer confines propagating modes to the planar devices and prevents loss from leaky modes that are typically found in purely 2D PBG devices. This novel structure allows for multilayer device hierarchies that can be interconnected in a means analogous to many of the complex microelectronics devices produced today.

For future successful device production, the square spiral PBG structure must be compatible with the incorporation of controlled defects to allow for the interconnection of adjacent device regions of the optical microcircuit. One of the simplest forms of defect is the line defect, which is produced when a seed or line of seeds is omitted from the patterned substrate and prevents the growth of particular spiral structures leaving an air channel for propagating modes. Examples of several sizes of line defects patterned by electron beam lithography are shown in Figure 2.18 where the omission of seeds results in long, narrow channels with little effect on the surrounding spirals. By omitting a few spirals, vias or interconnects between 2D active layers can be achieved. Studies of defect fabrication are the subject of ongoing research by graduate student Martin O. Jensen.

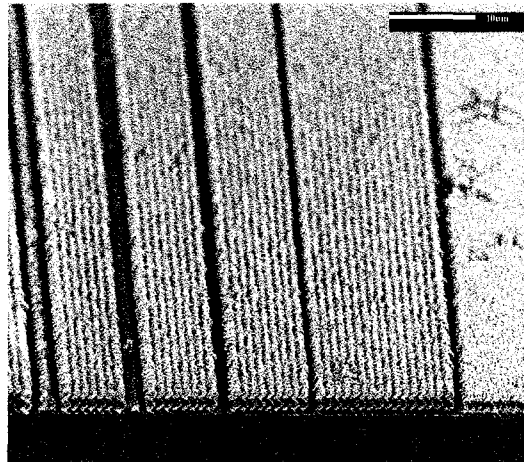


Figure 2.18 – Engineered defects in a square spiral crystal created by omitting specific rows of the patterned seeds. Low loss waveguides and optical microcircuitry can be readily fabricated using this technique that is unique to GLAD square spirals. Courtesy of M. O. Jensen.

3 Chapter 3

Properties of Square Spiral Photonic Crystals

^{6,7}In this Chapter, the properties of periodic square spiral films that are critical to the production of large band gap structures are presented along with thorough optical characterization of the three-dimensional structures. In creating a theoretical model to agree with results obtained for fabricated square spiral PCs, it was found that variations of up to 10% in the structure parameters had to be included and were found to corroborate with inspection of the crystals. It was observed that the overall structure and optical response of the square spirals can be significantly affected by crystallinity, material properties, and deposition conditions, and results of these are presented. By implementing advanced substrate motion algorithms, significant improvements to the overall crystal structure can also be obtained to enhance the optical response of the films. Finally, tuning of the properties of the band gap can be obtained simply through the variation of the parameters set forth in the GLAD control algorithm.

3.1 Deposited material characteristics of GLAD square spirals

Evaporated materials often have properties that differ substantially from their bulk counterparts [16]. This difference arises from the deposition process, which divides the original solid into individual atoms or molecules that must coalesce at the substrate some distance away. Depending on the gas species present, the temperature of the substrate, the deposition pressure, and even the material being deposited, different optical and structural properties can be obtained for the films. Two issues that must be addressed when fabricating optical thin film nanostructures are material crystallinity and

⁶ Portions of this chapter were excerpted with permission from [53] S. R. Kennedy, M. J. Brett, H. Miguez, O. Toader, and S. John, "Optical Properties of a Three-Dimensional Silicon Square Spiral Photonic Crystal," *Photonics and Nanostructures*, vol. www.elsevierphysics.com/photronics.html, in press 2003. Copyright 2003 Elsevier.

⁷ Portions of this chapter were excerpted with permission from [100] S. R. Kennedy and M. J. Brett, "Advanced Techniques for the Fabrication of Square Spiral Photonic Crystals by Glancing Angle Deposition," *submitted to J. Vac. Sci. Technol. B*, 2003. Copyright 2003 American Institute of Physics.

contamination by foreign materials. These factors are extremely important in the production of thin-film based, wide band gap PCs.

3.1.1 Deposited silicon crystallography

Direct structure tetragonal square spiral PCs are fabricated by GLAD with electron beam evaporated silicon due to its high dielectric constant and favourable deposition properties. Depending on the deposition conditions, silicon atoms can be arranged with high, medium or low order corresponding to crystalline, polycrystalline or amorphous phases. The three forms have considerably different optical, electronic, and structural properties due to the arrangement of atoms and electronic states in the solid. In the fabrication of photonic crystals, the two important material properties are the optical characteristics and the inherent growth tendencies imposed by crystallinity.

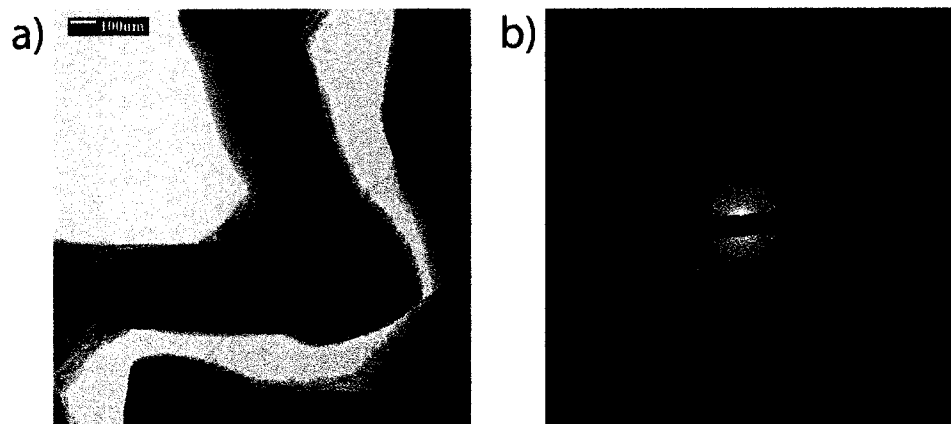


Figure 3.1 – a) High resolution transmission electron microscope bright field image of a silicon square spiral arm and elbow. b) Transmission electron diffraction pattern showing only a diffuse glow and indicating the amorphous nature of the deposited film material. Courtesy of B. Djurfors.

With assistance from colleague Barbara Djurfors, a transmission electron microscope (TEM) was used to determine the crystal structure of the deposited silicon square spirals. Due to the extremely small wavelengths of high-energy electrons in the TEM, it is capable of resolving extremely small grains in the structures and through the analysis of transmitted electron diffraction patterns accurate information on the crystallinity can be obtained. As the samples are required to be extremely thin to allow for transmission of some of the incident electrons, previously fabricated square spirals were removed from the original substrate and placed on a grid so that characterization

could be performed. Shown in Figure 3.1 are a bright field image of a portion of a silicon spiral and the associated diffraction pattern of transmitted electrons. As can be seen by the diffuse, isotropic glow of the diffraction pattern, the sample is highly amorphous with no regular atomic ordering characteristic of crystalline or polycrystalline phases. The lack of atomic regularity plays an important part in the fabrication of silicon square spiral PBG structures.

The optical properties of amorphous silicon are highly prone to effects from deposition conditions such as temperature, pressure and present gas species. Although the silicon square spiral structures are deposited in a high vacuum atmosphere, contamination by gases such as hydrogen can significantly affect the index of refraction of the deposited material [101]. As the index contrast in a PBG structure contributes significantly to the overall band gap, it is important to properly understand the optical characteristics of the materials so that accurate band structures can be predicted and fabricated. From early experiments performed on amorphous silicon, the index of refraction has been shown to vary from 2.8 to 3.8 in the wavelength range from 2.5 to 3.0 μm , and is dependent on the deposition conditions, particularly the presence of hydrogen and the formation of strong Si-H covalent bonds [101, 102]. Although it was not possible to determine the amount of hydrogen present in the square spiral films as this traditionally requires IR spectroscopy of the chemical species present which is also influenced by the film structure, it is a factor that must be considered if annealing or other post-deposition processing of the silicon films is to be performed. For all band calculations, the accepted average index of refraction for silicon of approximately 3.5 was used to represent its material properties.

The amorphous nature of silicon GLAD films also plays an important role in the formation of the square spiral nanostructure. Materials that exhibit preferred growth in specific crystallographic directions often result in film structures that are faceted and anisotropic [103, 104]. As the oblique GLAD deposition of silicon results in a highly amorphous film, migration of adatoms along the surface of the film is completely random and does not result from preferential growth along a particular crystal direction. This property of the deposited films allows for the fabrication of more uniform structures that

are not biased by preferential growth. By avoiding preferred condensation sites, the growth of specific morphologies can be controlled uniquely by shadowing and deposition conditions. This naturally occurring lack of crystal structure for substrates at low temperatures is ideal for the fabrication of GLAD morphologies that depend on uniform growth in the exposed regions of the substrate.

3.1.2 Oxygen contamination

From the previous section it can be noted that the material properties of the film can significantly affect both the fabrication and optical response of the square spiral PC structure, and although many of the detrimental properties of deposited materials may not be eliminated or avoided, by carefully analyzing their effect a more realistic and representative PC can be produced. Next to material crystallography, contamination by oxygen during the deposition process can have one of the most dramatic effects on the material properties of the as-deposited silicon spirals. Oxygen is always present in a practical vacuum deposition system either in gaseous form or as a component of water vapour and its strong affinity for oxidation means that a certain portion of the silicon deposited by PVD will have reacted to form an SiO_x complex. The most stable form of silicon oxide is SiO_2 , and as it has the lowest index of refraction it will have the greatest effect on the dielectric contrast and the resulting band gap of the crystal.

Deposition of silicon square spiral PCs was performed at an ambient pressure of 1×10^{-6} torr, and although residual gas analysis of this environment was not possible, it can be assumed that in the worst-case scenario the partial pressure of O_2 accounts for the entire ambient pressure. From Maxwell-Boltzmann theory, the monolayer formation time is given by [23]

$$\tau_m = \frac{\sqrt{2\pi mkT}}{p} \rho_a \quad (3.1)$$

where m is the mass of the gas molecule, k is the Boltzmann constant, T is the temperature in Kelvin, p is the partial pressure and ρ_a is the molecular packing density, which is approximately $8 \times 10^{18} \text{ m}^{-2}$. At a pressure of 1×10^{-6} torr, τ_m is approximately 1 s and given an approximate molecular diameter of 3 \AA , the deposition rate of oxygen at the

substrate is 3 Å/s. The deposition rate of evaporated silicon measured by the CTM was maintained at approximately 15 Å/s, which yields a maximum oxygen contamination value of 16%. Note that this value has been calculated in a worst-case scenario and results from assuming a uniform deposition rate along with the supposition that all of the residual gas in the system is oxygen. This will not be the case in the deposition of silicon square spirals as the actual percentage of oxygen will lie somewhere between 0% and this value, however it does provide a means of estimating its effect on the structures' material properties.

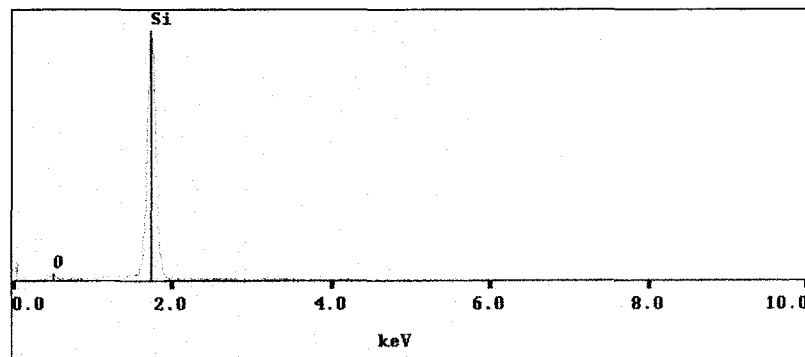


Figure 3.2 – Energy dispersive x-ray analysis of the deposited silicon structure. The presence of oxygen in the films is due to water and ambient gas in the deposition chamber contaminating the film. A relative composition of oxygen of approximately 8% was measured.

In an attempt to more accurately approximate the percentage of oxygen in the deposited silicon, energy dispersive x-ray analysis (EDX) was performed on a representative silicon square spiral sample. As the response of this technique is inversely proportional to the atomic number of the measured elements, the signal obtained from the oxygen present is approximately 1/5 that for equal parts of silicon. The results of the EDX are shown in Figure 3.2 where the only two notable peaks are from silicon and oxygen. To avoid obtaining an unwanted signal from the substrate, this measurement was taken on a small spot size of the cleaved edge of the film. Taking into account the difference in sensitivity for the two elements, the relative heights of the two peaks gives an approximate contamination by oxygen of 8%. This result is half of the worst-case value obtained from monolayer formation calculations and given the assumptions made above this value represents a reasonable approximation. The error in this value is, however, quite significant and is on the order of 5%.

Assuming an oxygen contamination of 8% distributed uniformly throughout the film structures, the effective dielectric constant of the deposited silicon can be calculated using Clausius-Mossotti-Lorentz-Lorenz effective medium theory [105, 106]. As the formalism of this theory is explained in detail in Chapter 5, the result will simply be quoted here. Before undertaking the calculations though, a final assumption was made in regards to the chemical form of the oxygen present in the film. For simplicity it was assumed that all of the oxygen was present as SiO₂ with a real dielectric constant of $\epsilon_{\text{SiO}_2}=2.07$. Using the dielectric constant for silicon of $\epsilon_{\text{Si}}=11.9$, the effective dielectric constant of the film material was calculated to be $\epsilon_{\text{film}}=11.3$. This value is used in all subsequent theoretical calculations of the band structure of deposited silicon square spirals to more accurately predict the optical properties of the fabricated crystals.

3.2 Advanced deposition control algorithms

The most basic method of depositing square spiral PC structures was highlighted in the previous chapter, however the resulting crystals exhibit many imperfections when compared to the ideal theoretical structure. These discrepancies become more pronounced as the number of deposited periods increases, so to counteract these deficiencies and improve the overall spiral and crystal structure, advanced substrate motion techniques were developed. These techniques are implemented to take advantage of the shadowing process characteristic of GLAD and to produce more favourable nanostructures.

3.2.1 Slow corner algorithm

The joint or elbow between successive square spiral arms can be one of the greatest sources of difficulty in the fabrication of quality square spiral PC structures. The most elementary method of forming the joint is by simple rotation of the substrate through 90° when the appropriate thickness is reached. This method, although simple to implement, is not ideal as the process is not stable and with successive turns the overall spiral structure degrades due to imperfect self-shadowing. Because the source can see a large portion of the previous arm when turned perpendicular to the incoming flux, subsequent growths are wider and often suffer from bifurcation, where an individual

column evolves into two independent growths, or severe broadening. An example of this is shown in Figure 3.3 where both bifurcation and the detrimental closing-in of the spiral structure have occurred due to unrestricted growth at the elbows. The spiral structure in this case has degraded from a set of square arms to an unidentifiable assortment of arms in a pseudo-random arrangement. This film no longer resembles the spiral structure of the original model nor do adjacent spirals overlap appropriately to produce a three dimensionally periodic structure.

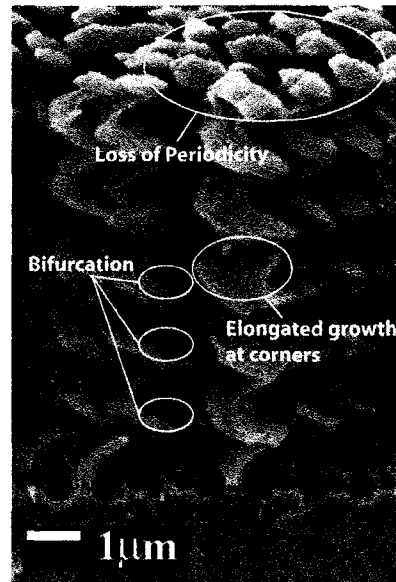


Figure 3.3 – Square spiral film grown using the traditional instantaneous turn method whereby the substrate is rotated abruptly by 90° at every quarter pitch. Due to imperfect shadowing, this method results in films with poor overall structure.

In an attempt to refine the fabrication of square spirals, a new algorithm was developed to impose greater restriction on the distribution of vapour flux at the arm joints. When individual inclined columns are grown by the traditional means, self-shadowing confines the flux to the ends of the arms. However, in the transition to a new growth direction, a great deal of this shadowing is lost and the structure diverges further from the ideal form. To counteract the loss of shadowing in these critical regions, a ‘slow corner’ technique was developed whereby rotation of the substrate occurs more slowly so as to maintain shadowing and confine growth to the tips of existing structures. A schematic example of this is shown in Figure 3.4 where the slow corner method results in finer and more uniform growth at the elbows. The rate at which the substrate is rotated is

determined by the corner pitch, Φ_c , and is the amount of vertical growth necessary for the substrate to rotate through 90° . When the appropriate arm height is reached and a new growth direction is required, the substrate is slowly and continuously rotated through one-quarter turn in a similar method used in the fabrication of a helical film. Once the thickness Φ_c has been reached, and the substrate is at right angles to the previous orientation, it is held stationary for the remainder of the arm growth.

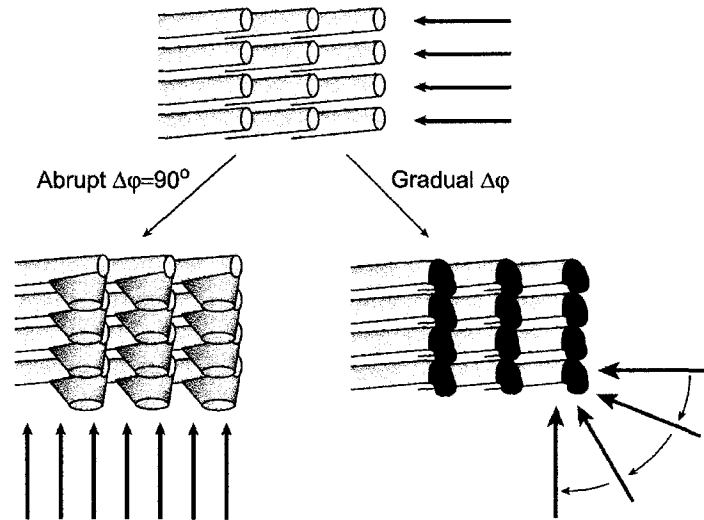


Figure 3.4 – Using the slow corner method (right), shadowing confines growth to the ends of the existing structures preventing bifurcation and broadening.

Typical values of the corner pitch, Φ_c , are most suitably given relative to the overall spiral arm height, $c/4$, and are generally from $1/6$ to $1/8$. This range of values has been found to be the optimal, providing the advantage of increased shadowing and more uniform corners with no detrimental effects to the overall spiral structure. For larger relative values for Φ_c , the square spiral structure degenerates into a pseudo-circular spiral that no longer provides the appropriate periodicity required for the generation of a large band gap, diamond or fcc lattice without the need for an introduction of a phase shift between adjacent spirals. The overall effect of this advanced technique on the film structure is shown Figure 3.5, where spirals have been grown using both the instantaneous turn and the slow corner methods. The periodic arrangement of fine spiral structures grown by the slow corner method and shown in Figure 3.5b is in stark contrast to the mass of bifurcated and broadened columns fabricated by the more simple

instantaneous turn method of Figure 3.5a. In this figure, both films have six complete arms grown with their appropriate method and to highlight the effect of this technique on the corners, only 100 nm of the 7th arm has been deposited, exposing the elbows. For the slow corner method used for the second film, a corner pitch of $\Phi_c=50$ nm was used resulting in an arm growth of 50 nm on top of the elbow. The slow corner method results in more uniform columns that maintain the periodicity originally imposed by the pre-patterned substrate. In addition to imposed periodicity, by avoiding severe broadening at the corners, the spiral structure of slow corner films is more defined and more closely emulates the simulated film structure of the ideal model.

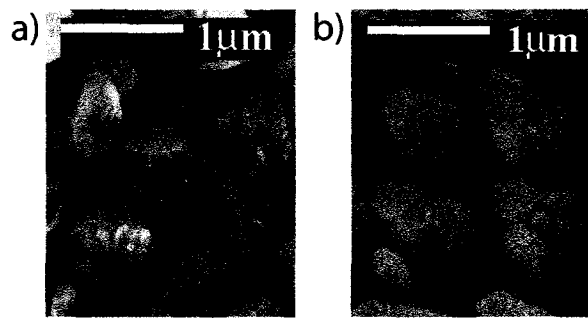


Figure 3.5 – Image of 2x2 square spirals grown by a) the instantaneous turn method, and b) the slow corner method. Using the slow corner method the film accurately follows the square pattern of the original substrate topography, and both bifurcation and broadening are greatly reduced.

As the ‘slow corner’ technique is easily implemented and serves only to improve the square spiral film nanostructure without any detrimental effects, this method was used to fabricate all successfully characterized square spiral films. Also, as the optical properties of the crystal structure are almost solely reliant on the film material and nanostructure, this simple but novel improvement represents a significant advance in the production of square spiral PCs.

3.2.2 Variable alpha post algorithm

Ideally, the cross-section of GLAD fabricated square spirals would be cylindrical and uniform throughout each arm length, meeting at each corner in succinct elbows. This is not the case, however, and as noted in Chapter 2 the cross-section of actual square spiral structures is closer to a square or rectangular shape. This anisotropy is due to the

restrictions on growth imposed by self-shadowing that occurs only in the deposition plane. As the flux is uniform perpendicular to this plane, no confinement of growth occurs laterally and for randomly seeded structures this effect can be seen by the chaining of the slanted posts of Figure 1.4. For seeded or periodically grown GLAD structures, the growth is confined to the seed locations; however, the uniformity of incoming flux perpendicular to the plane of incidence causes broadening and often extreme anisotropy for tall structures as shown in Figure 3.6. To overcome this natural discrepancy in flux distribution, self-shadowing must be imposed perpendicular to the traditional deposition plane. The most common means of creating slanted columns with more uniform cross-sections is through the use of a spin-pause algorithm where the angle of incidence is kept fixed while the substrate periodically rotates one full revolution and imposes some constraints on lateral column growth by imposing shadowing in directions other than simply parallel to the plane of deposition [35]. This technique is suitable for many applications; however, the distribution of flux about the axis normal to the substrate plane causes the posts to become more upright and to deviate substantially from the ideal inclination angle, β , of 54.7° for $n=1$ square spirals. In an attempt to produce columns with both large tilt angles and more ideal cross-sections, a new technique has been developed involving complex substrate motion in both the α and φ dimensions.

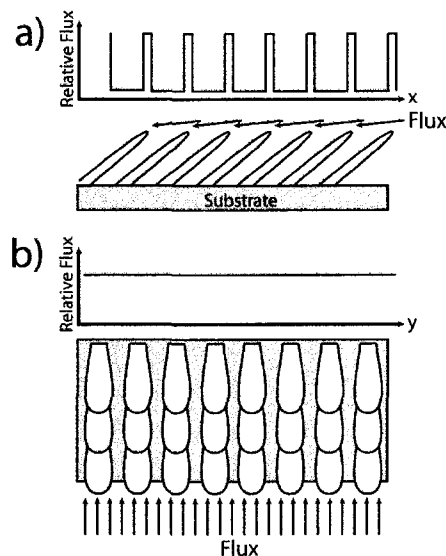


Figure 3.6 – Flux distribution resulting from self-shadowing a), in the deposition plane and b), perpendicular to the deposition plane. Due to the anisotropy of the shadowing that forms the nanostructures, they broaden perpendicular to the deposition plane.

Variable alpha posts (VAPs) are produced by the implementation of a technique similar to the spin-pause method, however their orientation with respect to the incoming vapour flux is held nearly constant rather than having them rotate periodically away from the source. The VAP method creates posts with a more ideal cylindrical shape due to imposed self-shadowing perpendicular to the traditional deposition plane. In the spin-pause technique, the angle of incidence is kept constant and the substrate is rotated about the φ axis while the VAP technique allows the vapour flux to precess uniformly around the traditional direction of column growth. By varying the deposition orientation in this way, a nearly constant value is obtained for difference between the flux incidence and the column growth angle. This difference, defined by γ , is given by

$$\gamma = \alpha - \beta \quad (3.2)$$

and is responsible for maintaining the oblique growth direction of the columns. A comparison of the the spin-pause and the VAP technique is shown in Figure 3.7 where in the spin-pause technique the angle between the incident flux direction and the column growth angle can be as large as $\alpha+\beta$, while for the VAP technique the difference is kept approximately constant.

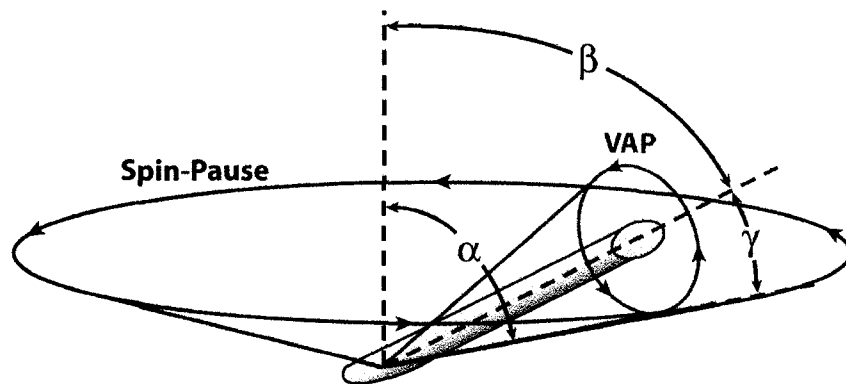


Figure 3.7 – Comparison of the VAP and spin-pause methods. In the ideal VAP method, the flux incidence vector is made to precess around the column growth direction. In the spin-pause method only φ is varied causing the column to become more vertical, resulting in smaller values for β

To implement the VAP algorithm, a GLAD system must be set up with 180° of freedom in α , with possible incidence angles ranging from -90° to $+90^\circ$ so that full substrate mobility is permitted. If we define the \hat{z} unit vector along the line from the

origin at the substrate surface to the vapour source, the direction cosine of the column axis with respect to this axis must be held constant to maintain the same value for γ . For a column of total length A , its projection along the z -axis, z_c , is given as a function of α , φ and β by

$$z_c = A \cos[\cos(\varphi)\alpha - \beta] \{ \sin(\alpha) \sin[\cos(\varphi)\alpha] \cos(\varphi) + \cos(\alpha) \cos[\cos(\varphi)\alpha] \} \quad (3.3)$$

Substituting this result into the expression for the z -axis direction cosine,

$$\cos \gamma = \frac{z_c}{A} \quad (3.4)$$

the column length cancels and results in an expression from which α and φ can be obtained for a given values of γ and β .

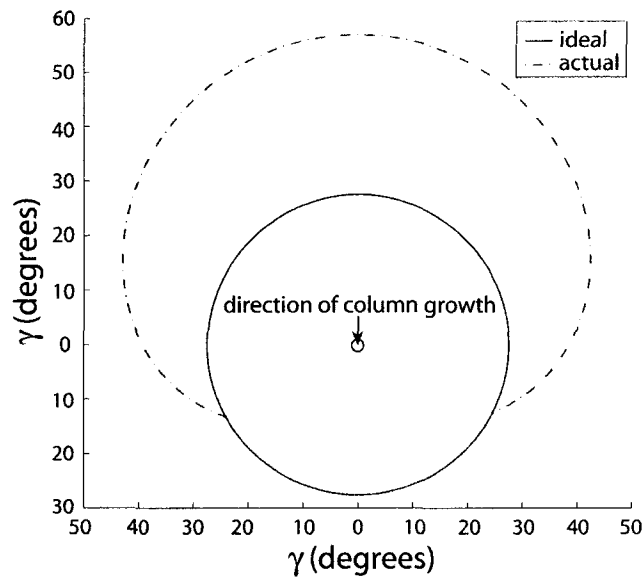


Figure 3.8 – Looking end on at the column (represented by the small circle at (0,0)), the ideal VAP method would have the incoming flux follow the solid line in precessing around the growth direction, in this case for $\beta=57.0^\circ$, $\gamma=27.5^\circ$. Due to the reduced number of degrees of freedom in the substrate motion, the dashed line is the approximated motion for the VAP algorithm.

To maintain a constant value for γ requires three independent degrees of freedom, yet with a standard GLAD system only two degrees of freedom are available. As the orientation of the column is not completely free due to this restriction, the error in γ was

minimized when calculating the values for α and ϕ . Standard deposition of slanted columns at $\alpha=84.5^\circ$ yields an inclination angle of $\beta=57.0^\circ$ and a value for γ of 27.5° . These results for β and γ were input into Equation 3.4 to calculate α for fixed integer values of ϕ from 0 to 359° . The actual profile of gamma with respect to the column growth angle can be seen in Figure 3.8, where the origin of the graph represents columnar growth directed at the observer, the solid line is the ideal, uniformly precessing flux distribution with $\gamma=27.5^\circ$ and the dashed line is the actual distribution of flux. As can be seen in the plot, the value of γ does vary from the 27.5° ideal circular profile and has a maximum value of 57° , however it is much more ideal than the obtuse angle extended by the spin-pause technique. Results of the success of this technique are shown in Figure 3.9 where traditional GLAD slanted posts are compared with two types of VAP algorithms.

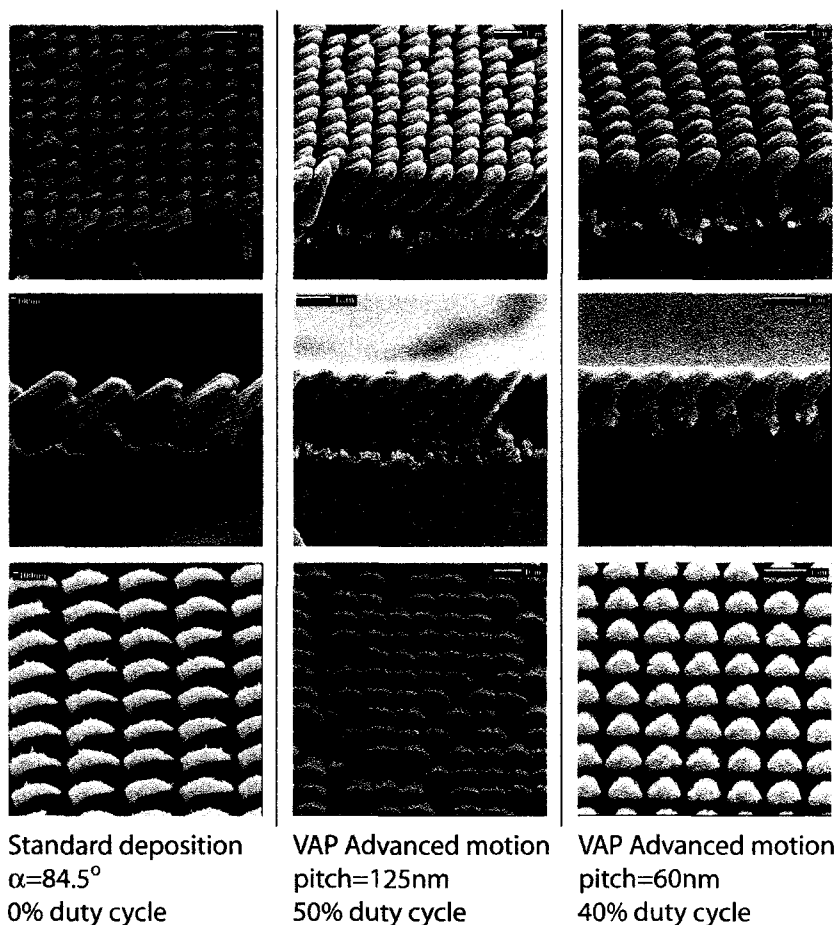


Figure 3.9 – Comparison of slanted posts grown using the fixed substrate method and the VAP algorithm. The films grown using VAP are much more uniform and have a more circular cross section. Due to the variation in α during deposition, the films are denser than the traditional slanted posts.

In the VAP technique used to produce the above structures, the angle of incidence is varied throughout the deposition from 84.5 to 0°. As a portion of the deposition is at or near normal incidence, the trade-off that must be made with the implementation of this technique is that the resulting films are more dense than traditional, obliquely deposited films. To counteract this effect, the control software was programmed with a pitch variable, Φ_{VAP} , which serves to control the rate of precession. Along with the speed of rotation, this technique is combined with fixed oblique deposition through the choice of a duty cycle, DC , where 100% represents continuous VAP substrate motion and 0% signifies standard, stationary oblique deposition. The duty cycle is imposed through the pitch by pausing at standard oblique incidence for a thickness given by

$$z_{pause} = \Phi_{VAP} \left(\frac{1}{DC} - 1 \right) \quad (3.5)$$

before proceeding to the next orbit of the deposition flux about the column. By varying the duty cycle, the density and associated structure of the film can be modified and the combination of these two variables, the rotation speed and the duty cycle, allows for fine-tuning of the overall film structure. The examples of Figure 3.9 show the effect of varying both the precession pitch and the duty cycle where the film on the right is composed of columns with nearly circular cross-sections and a density of approximately 60%.

Some difficulties are encountered when fabricating square spiral crystal structures by using the VAP algorithm due to the increased density of the films. As mentioned in Chapter 2, for a direct square spiral structure the fill factor should lie between 20 and 40%. The increase in the relative amount of high dielectric structure in the crystal to greater than 50% for the VAP structures would completely eliminate the band gap for a direct square spiral PC, however, this method does have advantages when fabricating inverse square spiral crystals. The ideal fill factor for an inverse structure is again in the range of 20 to 40%, however this constraint requires that the original template must have a fill factor of 60 to 80% with highly structured spirals. Using the appropriate pitch and duty cycle these densities can be readily obtained using VAP. The uniformity of the

column cross-sections produced in this way should also increase the overall symmetry of the crystal and aid in the production of a large band gap structures.

3.3 Fabrication of SiO₂ square spirals

The requirement of a large contrast in the index of refraction restricts the choice of material with which a direct square spiral PC can be fabricated to high ϵ semiconductors, however by using other materials such as SiO₂ it is possible to examine aspects of the crystals that are not otherwise observable. By depositing the films with materials other than silicon, the contribution of the material properties to the overall structure can be ascertained so that improvements can be made to the overall square spiral structure. Also, by fabricating PC nanostructures from arbitrary materials, it can potentially allow further processing of the materials for device fabrication. The effects of annealing can also be investigated, a process which can serve to produce more uniform crystal structures and predictable material properties.

3.3.1 SiO₂ square spirals as an inverse template

In Chapter 2, the inverse square spiral PC structure with its large PBG of up to 24% was introduced, however the specific method of fabrication was only alluded to. To produce an inverse square spiral, a template must be first created and must be filled with a high dielectric material such as silicon. Although infiltration of silicon into small pores is easily obtained through LPCVD [107, 108], a material which can be deposited initially using the GLAD technique and selectively etched after filling by the matrix material is required. SiO₂ is an ideal candidate for this process as it has been shown to have favourable deposition properties with respect to the fine structure of oblique incidence GLAD films and can be selectively removed by hydrofluoric acid-based solutions.

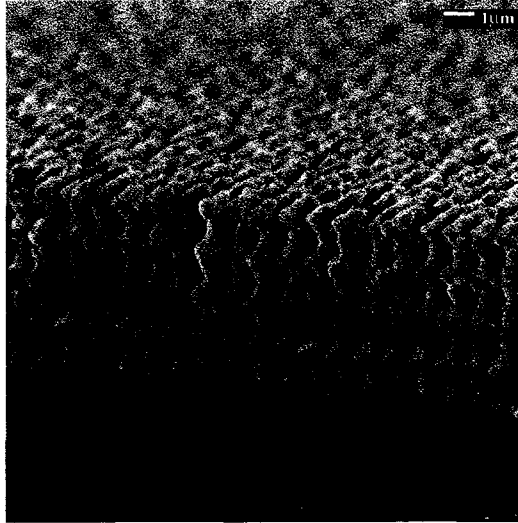


Figure 3.10 – *SiO₂ square spiral film deposited on a periodic substrate. Using SiO₂ instead of silicon it will be possible to create inverse crystals with enhanced band gaps.*

Shown in Figure 3.10 is an example of a SiO₂ square spiral film deposited on a tetragonally seeded substrate with $a=1000$ nm. SiO₂ structures were deposited under vacuum conditions of approximately 2×10^{-6} torr and at normal incidence rate of approximately 10 Å/s. The structure of the film, although substantially different from silicon nanostructures, is quite uniform throughout the film and the confinement of growth to the periodic grid of the substrate is very good. As can be seen in the figure, however, the spiral arms are broad in comparison to those of silicon films deposited under similar conditions. Diffusion of adatoms appears to have blurred the fine structure of the film, resulting in an overall increase in film density to approximately 50%. This material property would be highly detrimental to the fabrication of direct square spiral PCs, however as these films are to be used as templates for the inverse structure, the increase in density is actually favourable. To produce large band gap crystals, a final fill factor, f , of silicon in the inverse crystal should be in the range of 30 to 40%. This means that the original template must be deposited with a density of approximately 60 to 70%, values that are much larger than those traditionally assigned to GLAD films. To obtain these greater densities, the choice of material can be seen to play a large part in the overall deposited structure and the use of SiO₂, in combination with advanced substrate motion such as the variable alpha post algorithm, can likely accommodate these restrictions.

3.3.2 Post-deposition annealing

As demonstrated in the above section 3.1.1, GLAD deposited silicon structures are amorphous, a property that affects both the structure and the optical properties of the resultant crystal. By annealing the fabricated film at high temperatures, it is possible to reshape the film structure and modify the material properties after deposition. With the direct silicon PC structures, however, annealing requires a high vacuum environment as exposure of silicon structures to gases at high temperatures can result in the formation of undesirable oxygen or hydrogen compounds. By fabricating square spiral structures with SiO_2 , these problems can be circumvented, and it is possible to observe the effects of annealing on the structure in a regular atmospheric gas environment without the formation of undesirable compounds.

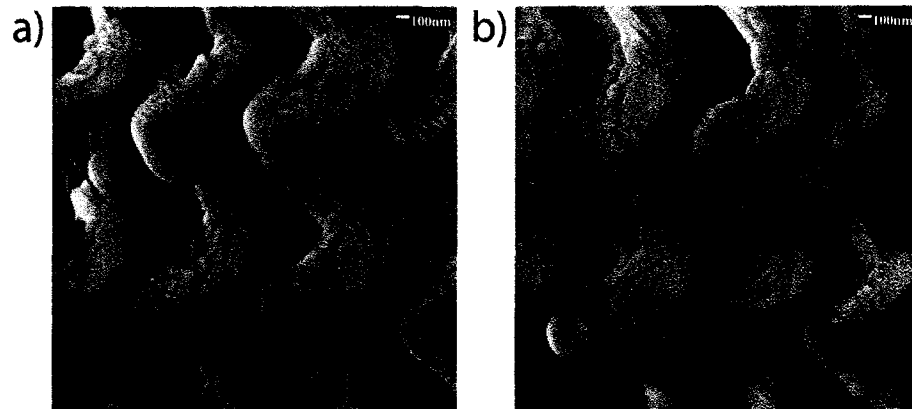


Figure 3.11 – a) As-deposited SiO_2 square spiral film and b) annealed SiO_2 film. The annealed film is seen to have a smoother surface without the feather-like rough elbows of the non-annealed film.

Shown in Figure 3.11 are the close up SEM images of a SiO_2 square spiral film before and after annealing. The film was placed in a furnace for 6 hours at 575 °C before being allowed to cool overnight. As can be seen by the difference between the two films, the high temperature has allowed for subtle reflow of the material, smoothing out the sides of the spiral arms and causing small projections to reform with the main structure. By permitting the film material to migrate at temperatures near the glass transition value, the roughness and anisotropy of the structures due to the deposition process can be significantly reduced and represents a potential solution to some of the deficiencies of the GLAD process. Also, by causing the spiral arms to reshape through surface tension it is

hoped that it will be possible to reform spiral arms with more uniform cross-sections across the entire crystal.

When the film material is heated to a point where atomic migration is abundant, for materials such as silicon with define crystallographic orientation it is possible that the material will re-form in a crystalline or poly-crystalline structure. Such re-crystallization has been shown in GLAD films for TiO_2 structures where annealing at high temperatures has significantly altered the properties of the film by the formation of polycrystalline grains [109]. For silicon thin film PBG structures, this improvement represents the potential to more accurately predict the band structures for periodic structures by the formation of crystalline domains within the silicon arms of the spirals. It is hoped that by more accurately defining the material properties of the spirals it will be possible to create a repeatable process with accurate predictions of the material properties that are more independent of deposition conditions.

3.4 Optical characterization of square spiral photonic crystals

The ultimate goal of developing a fabrication process for square spiral PCs is to provide a technique for producing structures with large, accurate and variable PBGs. The original theory of square spiral PCs confirms that, for ideal devices, this goal can be readily achieved, however, to create a practical device involves many tradeoffs. As seen in the previous sections of this chapter, some of these tradeoffs can potentially degrade or eliminate the band gap of the device through deviations of the structure from the ideal form as well as through the effects of material properties. Measurement of the optical properties of fabricated crystals is necessary to confirm the response of the device and to more thoroughly understand the effects of the disparities between ideal and fabricated structures.

Optical characterization of PBG crystals is traditionally done by the confirmation of both propagating and forbidden modes within the crystal through transmission and reflection measurements. Electromagnetic radiation with vacuum frequencies corresponding to disallowed modes within the crystal are reflected and are not allowed to

propagate through the periodic dielectric. Outside the band gap region, transmission is permitted as propagating modes exist within the crystal's nanostructure and large transmission values are expected. Thus, for reflection measurements of a PBG device, a characteristic peak in reflectivity is seen for frequencies within the band gap region where the transitions from low to high values correspond to the band edges. In practice, diffuse reflection from minor imperfections at the crystal surface reduce the detected reflectivity from its ideal value of 100% inside the PBG, and uncoupled bands may contribute to nonzero reflectivity outside the PBG. To confirm the periodicity and optical response in all directions for a full three-dimensional PBG, reflection or transmission measurements must be performed for all orientations in the 4π steradian unit sphere, or due to the reversible symmetry of optical systems measurements must be performed to cover a 2π hemisphere. In practical measurement systems, difficulties in accurate characterization arise due to the non-normal angle of incidence that is made with the exposed crystal surfaces. In addition to disruptions from coupling with surface modes, irradiation of the crystal surfaces at non-normal angles introduces errors due to the uncertain effective index of refraction of the crystal in the stop gap. To overcome some of these problems along with the loss due to scattering, the sensitivity of the measurement system must be great enough to provide good resolution of transmission or reflection values and in the analysis of obtained spectra these effects must be recognized for the accurate determination of band gap parameters.

3.4.1 Measurement of the three-dimensional band gap

A three-dimensional silicon square spiral photonic crystal was fabricated on a substrate seeded using photolithography with a principal lattice constant of $a=1000$ nm. The crystal was of the **[001]-diamond:1** type with $[L,c,e]=[0.72,1.40,0.37]$ and is shown in Figure 3.12 . The slow-corner technique of section 3.2.1 was implemented in the fabrication of the PC to maintain the accuracy of the structure throughout its growth with a corner pitch of $\Phi_c=45$ nm. A constant angle of incidence of $\alpha=84.5^\circ$ was maintained throughout the deposition to provide shadowing and a resultant fill factor, f , of approximately $1/3$. The spiral film was fabricated with eight complete turns resulting in a

total thickness of 11.2 μm and the structural parameters of the film were obtained using a JEOL field emission scanning electron microscope.

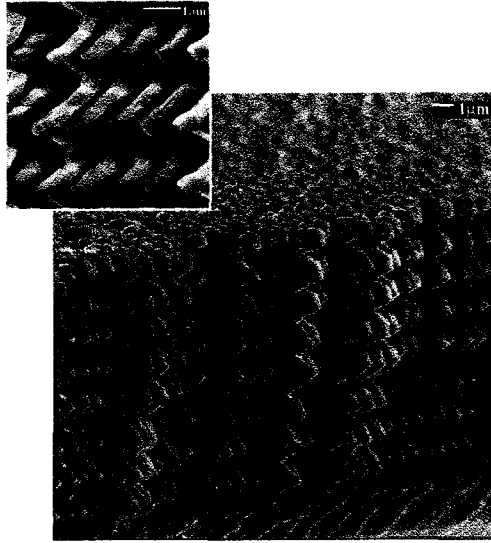


Figure 3.12 – Silicon square spiral photonic crystal fabricated on a photolithography patterned wafer with $a=1000$ nm and $[L,c,e]=[0.72,1.40,0.37]$. The slow corner method was used to improve the spiral structure with a corner pitch of $\Phi_c=45$ nm.

As with most appropriate square spiral PCs, this structure is predicted from theory to exhibit a robust, full three-dimensional band gap between the 4th and 5th bands. Shown in Figure 3.13 is the calculated band structure⁸ for this crystal with the cross hatched area indicating a relative three-dimensional band gap of 13% and a centre frequency corresponding to a wavelength of 2.7 μm in the infrared for $a=1000$ nm and for a deposited silicon dielectric constant of $\epsilon=11.3$. It is important to note that this theory is based on ideal square cross-section spiral structures with complete symmetry and uniformity throughout the lattice. As will be seen below, deviations from these assumptions substantially affect the optical properties of the crystal.

⁸ Calculated band structures provided by O. Toader and S. John of the Dept. of Physics at the University of Toronto.

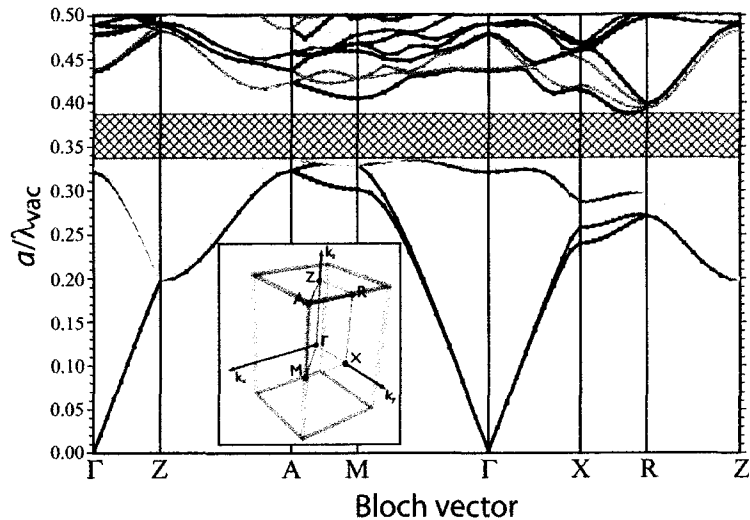


Figure 3.13 – *Calculated band diagram for the silicon $[L,c,e]=[0.72,1.40,0.37]$ $n=1$ structure for $\epsilon=11.3$. A full, three-dimensional band gap of approximately 13% is predicted.*

To characterize the full three-dimensional PBG of the crystal structure, reflection measurements were performed using several spectrometers in three independent orientations. The first measurement was performed using a Nicolet Magna-IR 750 Fourier transform infrared (FTIR) spectrometer normal to the substrate surface or centered around the Γ -Z direction of the Brillouin zone. The numerical aperture of the source/detector was 0.58 with a half-cone angle of 35° and the spot size of the optical system was approximately $250 \mu\text{m}$ in diameter, covering many basis units in the plane of the substrate. Although the structural characteristics of individual spiral arms may vary slightly over the surface of a large sample, one advantage that GLAD fabrication of square spiral PCs has over other PC fabrication techniques, such as self-assembly, is the ability to avoid flaws such as dislocations or stacking faults in the crystal lattice that can propagate throughout the crystal and destroy its symmetry. Due to the local nature of self-shadowing in GLAD films, defects tend to be limited to the scale of a lattice period and extremely large grains of several square millimetres can be fabricated and are easily characterized with instruments having a large spot size.

Results of the near normal reflection measurements are shown in Figure 3.14 with the peak in reflectivity characteristic of the disallowed PBG modes indicating a lower frequency band edge at a wavelength of $2.75 \mu\text{m}$. As the lower wavelength limit of the

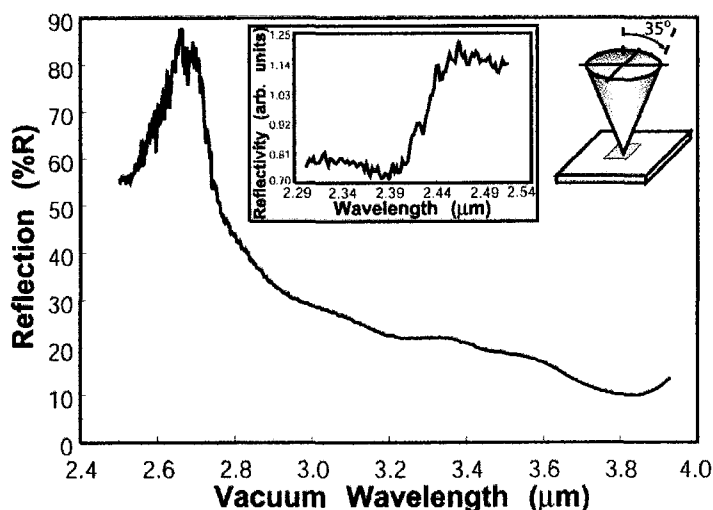


Figure 3.14 – Normal incidence reflection spectra for the photonic crystal of Figure 3.12. The inset shows the higher frequency band edge at 2.44 μm , while the lower frequency band edge can be seen in the main plot to be located at approximately 2.75 μm . The schematic in the upper right illustrates the experimental configuration.

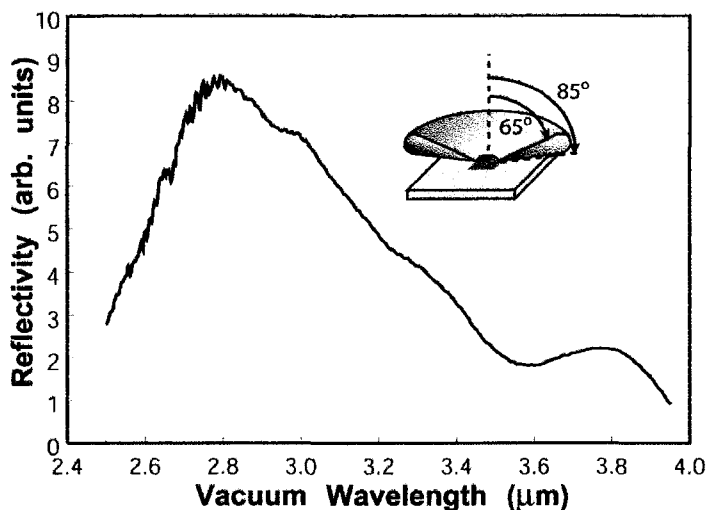


Figure 3.15 – FTIR reflectance spectrum for grazing angle incidence measurements. The oblique angles of incidence are uniformly distributed about the central axis of the optics and the result is the superposition of all directions within the annulus. A broad reflectivity peak emerges across the spectrum indicating a band gap from 2.5 to 2.9 μm .

FTIR spectrometer is 2.5 μm , a normal incidence reflection spectrum for the higher frequency band edge was measured using a Perkin-Elmer Lambda 900 spectrophotometer with an optical system closely replicating the conditions of the FTIR microscope. The

results of this measurement are shown in the inset of Figure 3.14 where a high frequency band edge of $2.44 \mu\text{m}$ can be seen.

To test the off-normal band characteristics of the three-dimensional crystal, a grazing angle incidence accessory was used with the FTIR spectrometer. This measurement is taken by an annular beam directed at a central point at angle from 65° to 85° from normal and the result is effectively an average of all measured propagation directions (see schematic in the inset of Figure 3.15). The resultant peak in the obtained spectrum of Figure 3.15 is an indication of the fact that the crystal has at least some omni-directional characteristics and is suggestive of a full photonic band gap. With this experimental configuration, it is possible that averaging of the spectrum over the azimuthal angles has blurred some of the detail of the band structure. Although difficult to determine exactly, the band edges at approximately 2.5 and $2.8 \mu\text{m}$ lie in the same region of the spectrum as those indicated by the near normal incidence measurements.

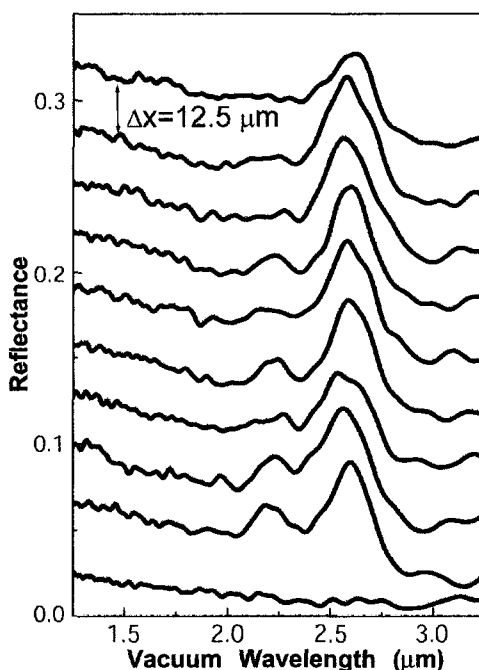


Figure 3.16 – In plane or edge measurements taken with a Cassegrain objective and an imaged spot size of $12.5 \mu\text{m}$. The plots represent the measured spectra at different locations on the edge of the sample with each taken at $12.5 \mu\text{m}$ intervals. The bottom spectrum was measured on an unpatterned region of the substrate corresponding to random spirals, while the reflectivity peak across the patterned region indicates a band gap from 2.50 to $2.70 \mu\text{m}$. The measurements on the patterned area near the bottom of the graph show the emergence of another stop gap at higher frequencies.

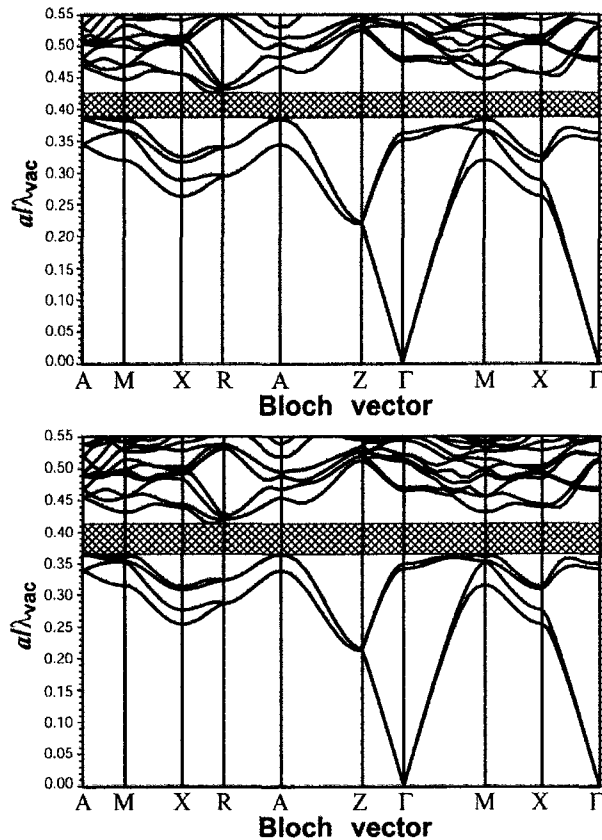


Figure 3.17 – Two typical photonic band structures for two different geometries of the spirals taken from the statistical distribution of spiral parameters used to fit the optical reflection spectra of the overall film. Top corresponds to $[L,c,e]=[0.71,1.40,0.33]$ with a 9% PBG and the bottom to $[L,c,e]=[0.73,1.39,0.34]$ with a 12% PBG. The bands above the photonic band gap change significantly with the structural parameters, however the overall gap shows little deviation.

A final set of reflection measurements was performed on the square spiral PC in the plane of the substrate. By cleaving the substrate along one of the lines of seeds, the side of the crystal was exposed permitting measurements to be made along the edge. As this measurement required a more sophisticated measurement apparatus due to the requirements of an extremely small spot size and the associated reduction in signal across a large spectrum of the infrared, this series of measurements was performed in collaboration with Hernan Miguez from the Universidad Polit cnica de Valencia in Spain. The samples were sent to the lab in Valencia where a series of high precision measurements were performed on them, allowing more thorough characterization of the GLAD PBG crystals.

An FTIR Bruker IFS-66 spectrophotometer with a 36X Cassegrain objective was used to image a spot size of 12.5 μm on the edge of the cleaved sample and the resulting spectra of Figure 3.16 were obtained. The series of curves were obtained by scanning across the edge of the patterned crystal at intervals of 12.5 μm with the bottom curve taken at a region outside of the patterned area of the substrate. The emergent peak again lies in the wavelength range of 2.50 to 2.75 μm and the frequency and width of the observed reflectivity peak exhibit small variations of roughly 10% from spot to spot. The precision of this instrument also shows the appearance at certain locations of a high reflectivity side lobe at higher frequencies. As shown in Figure 3.17 by the calculated band structures for crystals with structural parameters deviating slightly from the base configuration, the bands above the fundamental gap are sensitive to the changes in the crystal nanostructure.

3.4.2 Theoretical modelling of experimental results

As can be noted by the above results, the location and size of the crystal's PBG varies considerably from the ideal gap predicted by theory. The reduced reflection plateau width and broad wings of the reflection peaks for the near normal incidence and grazing incidence measurements are interpreted as a consequence of small fluctuations in the spiral arm properties over the larger spot sizes. The fluctuations lead to local variations of both the PBG and the local stop gaps across the sample and are a result of the non-idealities of the fabrication process.

The discrepancy between the band edges of simulations and experimental reflection measurements can be better understood when considering the graph of Figure 3.18. As indicated above, slight variations in the nanostructure across the crystal creates a local band gap that is shifted slightly from that of adjacent regions. To simulate the effect of this non-uniformity, the position of the stop gap edges in the Γ -Z direction were calculated for a set of structures with varying spiral arm properties. Each pair of points represents a particular $[L,c,e]$ uniformly distributed in the 3D volume $\Delta L \times \Delta c \times \Delta e = [0.70, 0.74] \times [1.39, 1.41] \times [0.33, 0.40]$, centred around the accepted average parameters for $[L,c,e]$ from above. The intersection of all stop gaps is highlighted in

Figure 3.18 and extends from 2.45 to 2.75 μm , closely matching the observed position and width of the reflectivity peak and indicating that subtle disorder does in fact play an important role in the optical response of the PC.

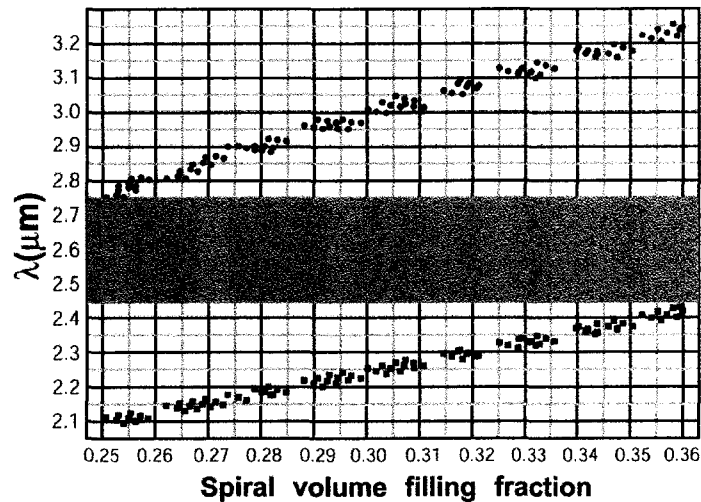


Figure 3.18 – The edges of normal incidence stop gap (Γ -Z direction) as a function of spiral fill factor. Each pair of points corresponds to a structure characterized by a dielectric constant of 11.3 and a particular $[L,c,e]$ uniformly distributed in the parameter space $\Delta L \times \Delta c \times \Delta e = [0.70, 0.74] \times [1.39, 1.41] \times [0.33, 0.40]$. The intersection of all stop gaps is highlighted and extends from 2.45 to 2.75 μm .

For the smaller spot size of the edge reflectivity measurements, the 10% variation among peak widths and centre frequencies is consistent with the theory that there exist local variations in the band gap due to local structure deviations. The fact that the variation is observed over a 12.5 μm range also suggests that the deposited square spiral film exhibits disorder on relatively short length scales and it is likely that portions of the PBGs for these deposited spiral crystals contain localized states of light rather than being completely devoid of electromagnetic waves. The coincidence of the above measurements essentially confirms the presence of a 10% three-dimensional band gap for IR wavelengths from 2.50 to 2.75 μm .

The disorder that is characteristic of the GLAD process, in particular the subtle variation in structure width of up to 10% across the crystal and the surface roughness of up to 20 nm for nanostructure feature sizes of one-half a micron, is one of the major downfalls of this process. The large band gap that is provided by these crystals can compensate for potential issues of bandwidth degradation due to disorder, however

scattering from microscopic roughness is an issue that is important in applications such as waveguides, and must be overcome by other techniques such as thermal annealing as mentioned in section 3.3.2 or by other post-deposition processing.

3.4.3 Shift of the photonic band gap

One advantage of the GLAD technique is its ability to vary the structure of deposited films through the simple variation of deposition parameters. To highlight the flexibility of this process, a square spiral PBG structure was fabricated with a similar structure to the crystal investigated in the previous section, only it was deposited with a larger vertical pitch (see Figure 3.19a). In particular, the crystal was fabricated with parameters $[L,c,e]=[0.74,1.53,0.38]$, and with a characteristic lattice period of $a=1000$ nm. From theory [8], the increase in c of approximately 9% with little deviation in L or e should result in a shift of the reflection peak characteristic of the stop gap to longer wavelengths. This would be the case for an ideal structure, however as seen in the normal incidence reflectivity peaks of Figure 3.19b the peak has shifted in the opposite direction with a centre wavelength of $2.1 \mu\text{m}$ and band edges corresponding to wavelengths of approximately 1.90 to $2.25 \mu\text{m}$.

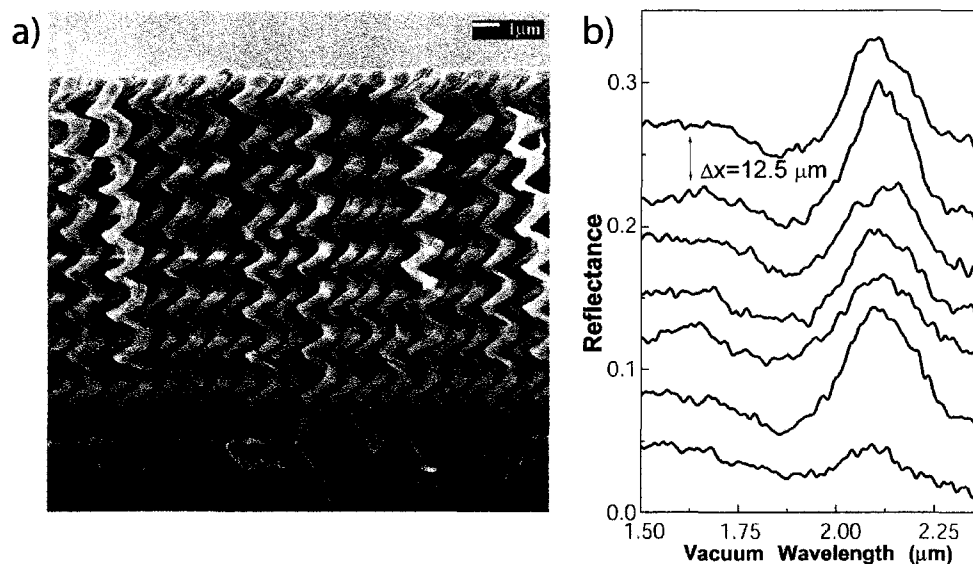


Figure 3.19 – a) Large pitch square spiral PC and b), normal incidence reflection measurements with the reflection peak corresponding to a directional band gap from 1.90 to $2.25 \mu\text{m}$.

The shift in the stop gap from the perturbation of film nanostructure is promising as it demonstrates the ability to tune the properties of the crystal simply through the GLAD control routine, however, the seemingly unpredictable behaviour of the crystal is initially troubling. If the nanostructure of the film is more carefully examined, the source of the discrepancy can be understood and is found to be due to the fabrication process. As mentioned in previous sections, broadening of the spiral arms occurs due to non-uniform shadowing perpendicular to the deposition plane. Although the slow corner algorithm is able to check this property of oblique growth for certain growth parameters, as the arms become longer, broadening can again become significant. The effect of broadening is to create arm cross-sections that are wider and shorter, and for measurements taken in the Γ -Z direction (incidence normal to the substrate plane) as in Figure 3.19, the incident beam sees a lower fill factor. The reduced arm size and fill factor in this direction causes a shift of the band gap to higher frequencies. Due to difficulties in cleaving the sample, in-plane reflection measurements were not obtained, however, it is expected that the band gap corresponding to this direction would be at the originally predicted longer wavelength. The non-uniform shift in the gap then serves to reduce the overall width of the combined three-dimensional gap due to structural anisotropy however by implementing more advanced fabrication techniques such as the VAP method it should be possible to accurately tune the location of the stop gap.

4 Chapter 4

Chiral Thin Film/Liquid Crystal Hybrids

⁹In this chapter, the similarities between the chiral or helical thin film morphology and circular polarizations of light are exploited to produce devices exhibiting optical activity through form circular birefringence. Parameterization of several deposition variables is performed, in particular, for hybrid devices employing liquid crystals to enhance their optical properties. The general theory of chiral mediums is discussed in the context of these unique film-based devices, and used to examine some of the unpredicted results of negative optical activity and the blue shift of wavelength properties upon the addition of liquid crystals to films made with certain materials.

4.1 Introduction to Chiral Optics

Chiral optics is the study of the interaction of light with structures having chiral or helical symmetry. ‘Chiral’ comes from the greek word for ‘handed’ and is derived from the unique property of a spiral that enantiomorphic pairs or mirror images (left- vs. right-handed spirals) cannot be made to coincide. This property of chiral objects means that the structure is unique and completely independent from its enantiomorph. One does not have to look far to find examples of chiral symmetry, for instance automotive coil springs or the threads of a screw are clearly helical structures. On a smaller scale, examples of chiral symmetry can be found in many natural molecular and crystal structures and in many cases is important to their functionality. This fact was of key importance in work by W. S. Knowles, R. Noyori and K. B. Sharpless who were awarded the 2001 Nobel Prize in chemistry for their work on the synthesis of uniquely chiral organic molecules, demonstrating the importance of ‘handed’ structures [110]. As will be shown, GLAD nanostructures can also exhibit helical symmetry on the scale of a wavelength of visible light resulting in interesting interactions between the unique nanostructures and electromagnetic radiation.

⁹ Portions of this chapter were excerpted with permission from [51] S. R. Kennedy, J. C. Sit, D. J. Broer, and M. J. Brett, "Optical activity of chiral thin film and liquid crystal hybrids," *Liquid Crystals*, vol. 28, pp. 1799-1803, 2001. Copyright 2003 Taylor & Francis Ltd, <http://www.tandf.co.uk>.

When a wavefront of light impinges on any type of chiral medium, many effects can be seen and can be inherent in the material, electrically induced or even magnetically induced [111-113]. The most common example of a chiral optical effect, optical activity, was first observed by D. Arago in 1811 when he noted that linearly polarized light underwent continuous rotation as it propagated down the optical axis of a quartz crystal [114]. This examination was followed by similar discoveries by Biot for substances such as turpentine and sugar solutions [115]. The rotation of linearly polarized light is a result of the spiral symmetry inherent in the crystal structure in the case of quartz, or in the molecular structure in the case of liquid solutions, and can be either right- or left-handed depending on the structural symmetry of the enantiomorph. Along with optical activity, chiral mediums exhibit other unique properties such as circular birefringence, circular dichroism and rotatory dispersion, all of which will be described in detail.

4.1.1 Optical activity and circular birefringence

When a monochromatic wavefront of linearly polarized light is incident on a chiral medium, three principle effects are often observed. The first effect is optical activity or the rotation of linearly polarized light and as will be shown, is a direct result of the second property of materials with helical symmetry, circular birefringence. Circular birefringence is a difference in the index of refraction as seen by the two independent circular polarization modes (left- and right-hand polarization) incident on a chiral medium. The third effect is circular dichroism, or the selective absorption of one of the two modes of circularly polarized light. These properties of the chiral medium are often inextricably linked and must be considered as a single macroscopic property of the medium responsible for the form of the emergent wavefront. The wavelength of incident light also plays an important role in all three effects resulting in dispersion functions for each property and for the case of optical activity the variation of the rotation of polarized light with wavelength is known as rotatory dispersion.

If one were to place a screen at a fixed position in space, perpendicular to the propagation vector of a polarized wave of light, and were able to observe the electric field vector as a function of time, one would see that for different polarizations of light the electric field traces out different, fixed patterns. In the case of linearly polarized light, the

electric field vector would oscillate back and forth in a straight line, making an angle θ relative to an arbitrary axis with the coordinate system defined looking back toward the source (see Figure 5.1a). As with any two-dimensional coordinate system, the electric field vector in the plane of the screen can be resolved into two orthogonal components, in

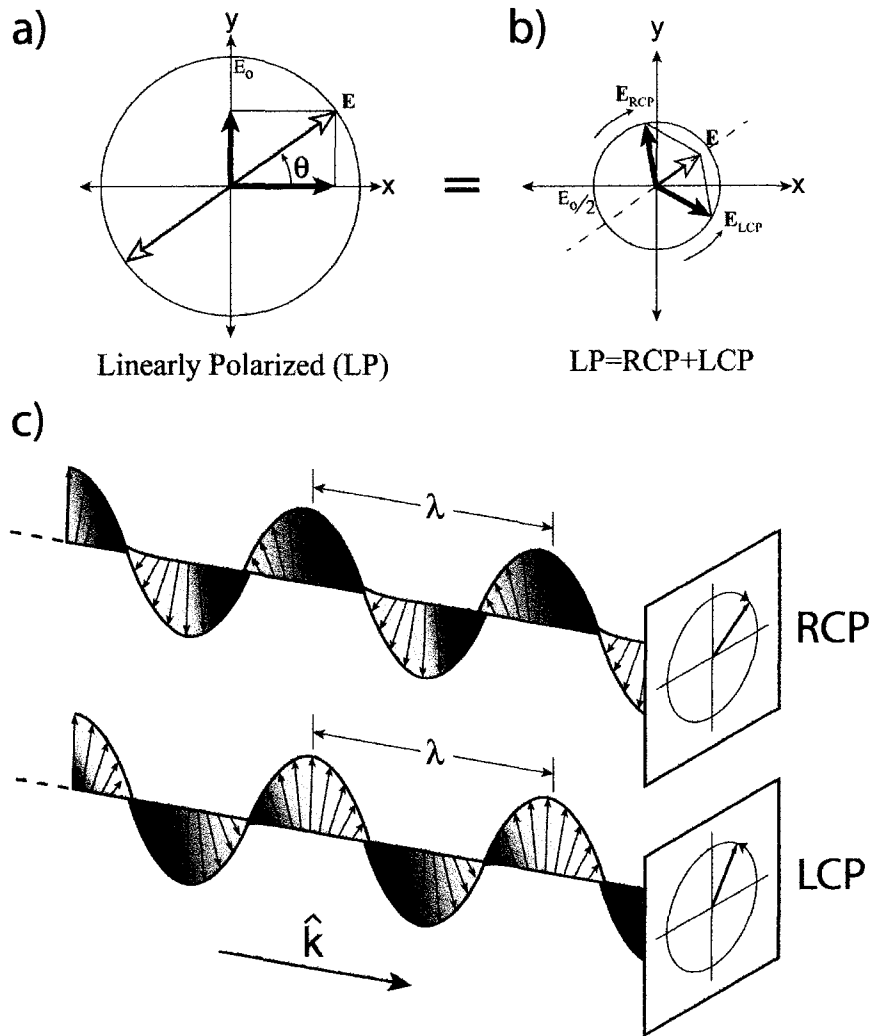


Figure 4.1 – The relation between linear and circularly polarized light. By resolving linearly polarized light, a), into two orthogonal components, b) of right- and left-circularly polarization, it is easier to understand the interaction of polarized light with a chiral medium.

the case of linear polarization of equal phase, and as shown in Figure 5.1a this is done using the standard Cartesian coordinate system with unit vectors in the x and y directions and positive z being the direction of propagation. Another representation of linearly polarized light is especially useful when chiral symmetry is involved whereby linearly

polarized light is resolved into two orthogonal components of left- and right- circular polarization. When imaged on a fixed screen, the electric field vector of circularly polarized light is represented by a vector of constant magnitude rotating in either a clockwise (right-handed) or counter-clockwise (left-handed) direction with angular velocity ω , equal to the angular frequency of the incident light (the convention used throughout this research defines handedness by looking back toward the source which is the historical physical convention and is opposite the convention adopted by the IEEE). The form of circularly polarized light as it propagates through space can be seen in Figure 5.1c and is helical or chiral in shape – a result that will become helpful when dealing with chiral mediums.

In a given medium the complex dielectric constant, $\tilde{\epsilon}$, serves to define the electrical properties, and is often a multi-dimensional quantity depending on the anisotropy of the material. We assume that the material is non-magnetic and has a permeability close to unity. Ignoring the tensor form of $\tilde{\epsilon}$ and examining only the quantity corresponding to the specific directionality of our situation, we can also define a complex index of refraction, \tilde{N} .

$$\tilde{\epsilon} = \epsilon_1 + i\epsilon_2 = \tilde{N}^2 \quad (4.1)$$

$$\tilde{N} = n + i\kappa \quad (4.2)$$

This definition can be applied to most situations as it has been written generally. As such it can be applied to both linear and chiral symmetry depending on the propagation mode. In general, for an optically active, or chiral material, we have $\tilde{N}_R \neq \tilde{N}_L$ for right- and left-handed polarizations respectively, or circular birefringence. As a circularly polarized wave passes through a birefringent material, its propagation depends uniquely on its handedness.

Mathematically, we can write linearly polarized light, \mathbf{E}_{LP} , in the form

$$\vec{E}_{LP}(z, t) = E_0 \cos(kz - \omega t) (\hat{\mathbf{i}} \cos \theta + \hat{\mathbf{j}} \sin \theta) \quad (4.3)$$

where θ is the angle that the electric field makes with the x axis as shown in Figure 4.1a. As the orientation of the axes is chosen arbitrarily, we set $\theta = 0$. The other propagation

constants of the wave are ω , the angular frequency, and the wavenumber, k , which is dependent on the incident wavelength, λ_o , and the material through the index of refraction. For a non-absorbing dielectric, the index of refraction is real, $\tilde{N} = n$, which is the situation of interest for optical materials and as such k can be written,

$$k = \frac{2\pi n}{\lambda_o} \quad (4.4)$$

To relate the propagating linearly polarized wavefront to the chiral structure having a similar helical shape, we write it as a sum of left- and right-handed orthogonal polarizations.

$$\vec{E}_{LP} = \vec{E}_R + \vec{E}_L \quad (4.5)$$

$$\vec{E}_R(z, t) = \frac{E_o}{2} [\hat{i} \cos(k_R z - \omega t) + \hat{j} \sin(k_R z - \omega t)] \quad (4.6)$$

$$\vec{E}_L(z, t) = \frac{E_o}{2} [\hat{i} \cos(k_L z - \omega t) - \hat{j} \sin(k_L z - \omega t)] \quad (4.7)$$

Note that the wavenumber for each handedness has been written with the appropriate subscript as the two values are not equal due to the anisotropy or circular birefringence of the material. In particular for chiral optical mediums,

$$k_R \neq k_L \text{ as } n_R \neq n_L \quad (4.8)$$

As the circular polarized wave travels through the material in question, the handedness that matches that of the underlying structure will see a higher index of refraction due to the similarities in shape of the wave to the nanostructure, while the opposite polarization will see principally the inverse medium enveloping the chiral forms.

We choose our coordinate system so that the wavefront is incident on the chiral material at $z = 0$, and define the thickness of the material to be z_o . The circular components of the linearly polarized light, as they emerge at $z = z_o$, have their relative phase altered due to the difference in optical path length from the circular birefringence of the chiral material. In particular, the resultant wave is given by

$$\begin{aligned}
\vec{E}_{LP}(z_0, t) &= \vec{E}_R(z_0, t) + \vec{E}_L(z_0, t) \\
&= E_O \cos[(k_R + k_L)z_0/2 - \omega t] [\hat{i} \cos(k_R - k_L)z_0/2 + \hat{j} \sin(k_R - k_L)z_0/2]
\end{aligned}
\tag{4.9}$$

Upon comparison of Equation 4.9 to Equation 4.3 we see that the resultant vector is again linearly polarized, but now makes an angle relative to the x -axis which is non-zero if $k_R \neq k_L$. Using the convention of defining a positive rotation as clockwise looking back toward the source [116], we define the rotation angle $\phi = -\theta$,

$$\tan \phi = -\frac{\sin[(k_R - k_L)z_0/2]}{\cos[(k_R - k_L)z_0/2]} = \tan[-(k_R - k_L)z_0/2]
\tag{4.10}$$

$$\begin{aligned}
\phi &= -(k_R - k_L)z_0/2 \\
&= \frac{\pi z_0}{\lambda_O} (n_L - n_R)
\end{aligned}
\tag{4.11}$$

Thus optical rotation is a function of the thickness, z_0 , through which the wavefront must pass, the wavelength of incident light, and most importantly the birefringence of the material defined by

$$\Delta n_c = n_L - n_R
\tag{4.12}$$

Given a fixed wavelength, the specific rotatory power or optical activity per unit thickness is dependent only on the difference in index as seen by the two circular polarizations. As will be shown, the ability to modify circular birefringence allows for the enhancement or reduction of optical activity exhibited by the structure.

4.1.2 Circular dichroism

In the above case we have assumed that the intensity of the two orthogonal modes of circularly polarized light is constant, as the medium is non-absorbing. This will be the case for many materials; however, circular dichroism or the selective absorption of one of the polarizations is observed in many situations. The result of the reduction in intensity of one of the modes on the emerging wavefront is elliptical polarization instead of linearly polarized light. Elliptically polarized light is a mode found to lie between the

two extremities of linear and circular polarization. Similar to linearly polarized light there is a major axis in which the largest component of the electric field oscillates back and forth, while similar to circularly polarized light, the electric field vector rotates around in either a clockwise or counter-clockwise manner. Comparing Figure 4.1b to Figure 4.2 we see that circularly polarized light is a special case of elliptically polarized light where the magnitude of the electric field is constant.

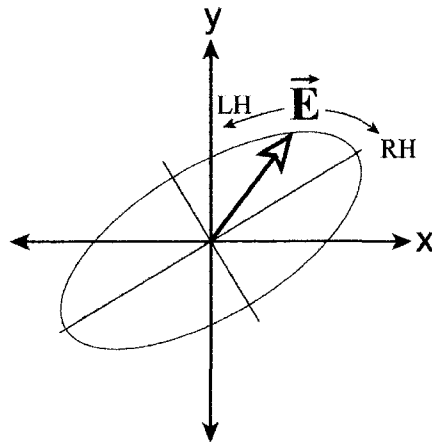


Figure 4.2 – Elliptically polarized light. A special case of elliptically polarized light is circularly polarized light where the magnitude of E is constant.

Elliptically polarized light results from interactions with biaxial chiral mediums, a class of helical materials that GLAD structures fall into. Biaxial mediums have a non-zero rise angle, or vertical pitch, while uniaxial mediums are strata of birefringent materials layered with their principle axes slightly rotated relative to the previous neighbouring layer to form their spiral symmetry [117]. Because of the inherent circular birefringence of both types of chiral mediums, there is often a natural selectivity of one of the two types of circular polarization. This selectivity means that if we consider dichroism as not only the absorption of light, but any mechanism by which one transmitted polarization has its intensity reduced relative to the other mode, it will occur in most chiral mediums due to selective reflection and scattering. When examining Fresnel reflection due to index mismatch at an interface for each mode, there will be different reflectivity as $n_R \neq n_L$ and looking simply at overall transmission the result will be elliptically polarized light. Depending on the form of the chiral material, selective scattering can also occur increasing its dichroic properties.

4.1.3 Rotatory dispersion

Examining the wavelength dependence or rotatory dispersion of chiral optical effects, we see that λ_o plays not only an important part in optical activity as shown in Equation 4.11, it has major contributions to the other chiral effects. As with most materials the index of refraction is a function of wavelength and in chiral mediums this is also the case. In addition to the material effect, the actual chiral structure interacts with different wavelengths in different ways and is strongly dependent on the underlying structural anisotropy. As the wavelength of circular polarization of similar handedness to that of the material becomes equal to the chiral pitch inherent in the structure, the circular birefringence becomes more pronounced. Following this argument, a Bragg resonance peak is predicted at a wavelength given by

$$\lambda_C = n_{eff} \Phi \quad (4.13)$$

where Φ is the pitch or vertical period of the helical structure and n_{eff} is an effective index of refraction as seen by the polarization matching the handedness of the material. At this critical wavelength maximum optical rotation and Bragg reflection will occur [118, 119]. Resultantly, optical activity and circular dichroism show a strong dependence on wavelength.

4.2 Chiral GLAD/liquid crystal hybrids

Helical GLAD nanostructures are inherently chiral objects from which chiral optical devices can be fabricated. Shown in Figure 4.3 is an example of a helical GLAD film of thermally evaporated MgF_2 . From this figure it is clear that the interaction of circularly polarized light with the similarly shaped structure will be highly anisotropic and dependent on the handedness of the film.

Obliquely deposited thin films with chiral symmetry are not new structures. In 1959 Young and Kowal first produced a chiral fluorite film by depositing onto a rotating substrate at a non-normal angle of incidence, resulting in an optically active device [31]. The deposition angle in this case was between 30° and 60° , rendering the films quite dense and as scanning electron microscopy was not available the exact structure was not

determined. However, their pioneering work obtained devices with specific rotatory powers of up to $0.155^\circ/\mu\text{m}$. Some time following this success, Azzam proposed some applications of obliquely deposited chiral thin films and refined the idea to be used in the fabrication of such films [120]. Lakhtakia and Weiglhofer subsequently developed a theoretical treatment for these novel film structures, classifying them as ‘helical bianisotropic mediums’ for their biaxial helical structure [121].

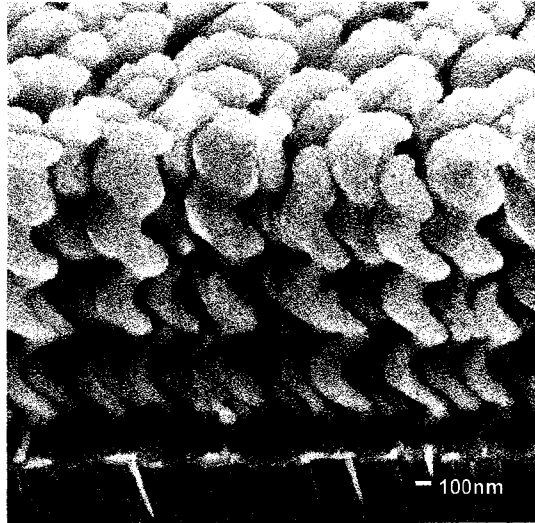


Figure 4.3 – Chiral GLAD MgF_2 film fabricated by thermal evaporation. Films with helical nanostructure are fabricated at a fixed, oblique angle of incidence and constant substrate rotation relative to the incoming flux rate.

Robbie *et al.* were first to use extreme oblique angles of incidence ($>80^\circ$ from normal) in the fabrication of optically active GLAD structures [1, 2]. Optical rotation and rotatory dispersion measurements along with ellipsometric characterization were performed on helical MgF_2 films, showing rotatory powers on the order of a $0.3^\circ/\mu\text{m}$ for visible wavelengths of light [2, 122, 123]. As these films were deposited at highly oblique angles of incidence the resulting films were extremely porous with densities less than 50% of bulk. In an effort to improve the magnitude of rotation of such thin-film-based devices, Hodgkinson *et al.* [42] fabricated denser titanium oxide (TiO_2) films and obtained rotatory powers of up to $5^\circ/\mu\text{m}$. The TiO_2 films were deposited at angles of 65 - 70° from normal using the serial bideposition technique, a technique similar to GLAD used to produce denser helical nanostructures [42, 124]. This advance showed a marked

improvement over GLAD-based optically active thin films, however these films lacked the flexibility to allow for dynamic control over the chiral optical properties of the device.

In 1999, Robbie *et al.* were able to take advantage of the unique porous nanostructure of GLAD films and show a significant improvement in circular birefringence of the films by the addition of nematic liquid crystals (NLCs) [125]. As the films were hydrophilic and contained a significant percentage of voids, the addition of liquids to create a hybrid device was a natural combination. Using the GLAD film as a backbone for alignment, the anisotropic NLC molecules enhanced the overall optical effects of the device. In addition to the enhancement offered by such a hybrid, and possibly the most important discovery, the addition of NLCs increased the device flexibility by allowing electro-optical switching of the optical properties [50, 126]. Such devices show promise in applications to flat panel display technologies and electro-optical modulation of optical signals as demonstrated in work by colleague J. Sit [127]. All of these results were preliminary investigations into the properties of the films, requiring a more comprehensive study so that the overall behaviour of such devices could be predicted. In the following sections of this chapter, a fundamental study of chiral GLAD/liquid crystal hybrids will be presented, investigating the effects of several film parameters on the optical properties of the device.

4.2.1 Liquid crystals

Thermotropic liquid crystals (LCs) are organic substances exhibiting molecular order similar to crystalline solids, yet, which at operating temperatures are fluid in nature similar to an amorphous liquid. Because of these unique properties LCs are highly anisotropic, particularly with respect to their optical properties [128, 129]. There are two major types of LC molecules classified by their molecular structure: rod-like (calamitic) and disc-like (discotic). These molecules are most commonly formed from chains of organic subgroups and monomers, which are responsible for not only their optical anisotropy, but also for their chemical functionality [130]. The structural anisotropy of the LC molecules allows for the definition of a director, \hat{n} , that corresponds to the orientation of the long axis of a calamitic LC molecule, or to the surface normal to a discotic molecule, and by the application of an external electric field, the electronic

anisotropy can be used to create a torque which serves to align the director with the applied field. In addition to the structural properties of the LC molecules, their optical anisotropy can also be defined along the two principle directions by n_o and n_e , the ordinary and extraordinary indices of refraction. In this research, the rod-like form of LCs is of primary interest because its functional shape is capable of infiltrating the small interstitial voids of a GLAD film.

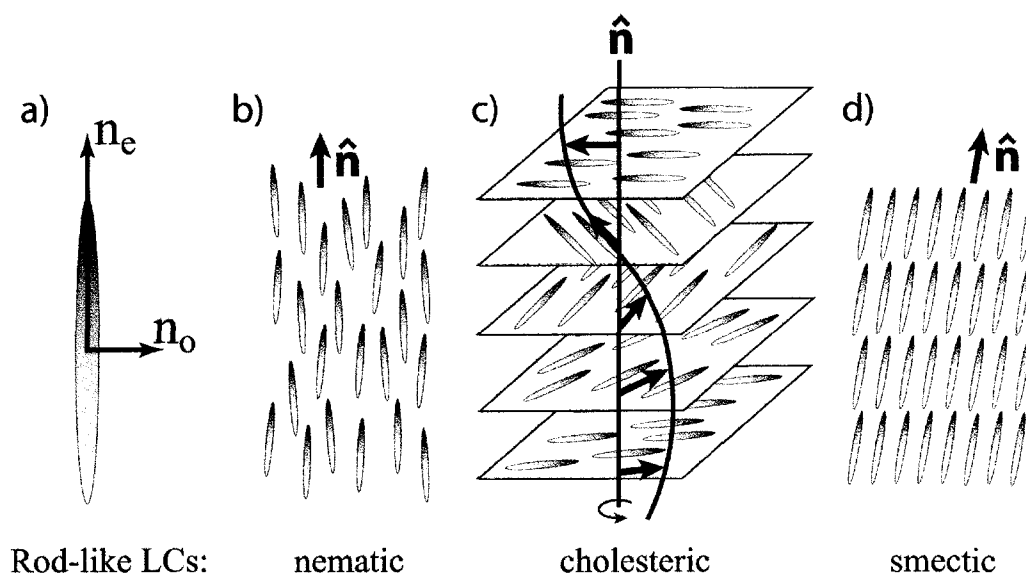


Figure 4.4 – Phases of calamitic (rod-like) LCs. a) Representation of a long, anisotropic rod-like LC molecule. b) In the nematic phase there is long range orientational order only, in the cholesteric or twisted nematic phase, c), the principle axis precesses around a central axis and in d), the smectic phase, there is both orientational and translational order.

Calamitic LCs are classified further by their long- and short-range ordering (see Figure 4.4). Not including the complete random ordering of elevated-temperature isotropic LCs, the most elementary arrangement is the nematic or ‘thread-like’ form having a high degree of long-range orientational order, but no long-range translational order (NLCs). These molecules are aligned with their long or principle axes approximately parallel, but with no translational symmetry. The next classification is the cholesteric phase composed of nematically ordered optically active molecules. Through such ordering the principle axes precess around a central axis making the liquid crystal highly optically active. In particular, cholesteric LCs have rotatory powers that are nearly a thousand times greater than other optically active substances due to their large circular

birefringence [128]. Finally, the most ordered form of rod-like LCs is the smectic phase having both long- and short-range orientational and translational order. This phase is often arranged in layers and within each layer several types of ordering are possible. All of these phases are highly dependent on temperature – at lower temperatures more ordered phases are seen and as the temperature is increased, so is tendency for disorder of the mesogens.

4.2.2 Chiral nematics

The cholesteric or chiral nematic phases are some of the more interesting LC structures and are most appropriate for applications in displays and communication devices, as well as in applications with GLAD films [131]. Shown in Figure 4.4a is a representation of an anisotropic rod-like LC molecule having two distinct indices of refraction for the two principle directions. In the chiral nematic phase these molecules are arranged as seen in Figure 4.4c where the director precesses around the central axis drawing out a helical shape. To align the molecules in this fashion, either chiral dopants can be added to the nematics [132, 133] or two substrates, one top and one bottom, are placed with their directors perpendicular to one another producing a twisted nematic (TN) configuration [134]. The result is a highly optically active medium due to chiral symmetry in the molecular ordering and thus by specifically controlling the orientation of the LC molecules one is able to tailor the chiral optical properties.

Orientalional control of LCs can be obtained in many ways. Some of the functional polymer groups of the LC molecule can be tailored to align with nearby surfaces and are especially sensitive to any defects or preferential directions favoured by the surface. Taking advantage of such properties, techniques such as rubbing [135], oblique thin film deposition [136, 137] and photoalignment [138] have been used with high degrees of success in restricting the alignment of LC molecules. The difficulty with these techniques is that the confinement is a surface effect and as the LC cell becomes thicker, the potential for misalignment increases with the distance from the interface. Using highly porous chiral GLAD films with inherent helical structure, it is possible to fill the films with nematic LCs and have surface alignment throughout the thickness of the cell from interactions with the GLAD nanostructure.

4.2.3 Alignment of NLCs by chiral GLAD films

Due to the natural chiral structure of a helical GLAD film, it is optically anisotropic with respect to circularly polarized light. As seen above, the magnitude of the chiral optical effects of a film is reliant on the circular birefringence and as such it is highly desirable to gain the ability to modify, or in particular increase, this property. The addition of NLCs to a helical GLAD film specifically allows the flexibility and enhancement of the properties of the hybrid device.

As NLC molecules favour alignment to preferential directions of surfaces, a chiral nematic-like phase is induced in the NLCs upon addition to helical GLAD films. Shown in Figure 4.5 is a schematic example of the alignment of the optically anisotropic molecules by the film nanostructure. Although the exact anchoring mechanism is not known and is most likely dependent on both NLC species and GLAD film material, this diagram gives an idea of the induced chiral nematic phase present in helical GLAD film/NLC hybrid devices. It is the combination of both the helical nanostructure of the film and the chiral NLC phase that results in the favourable properties of the device.

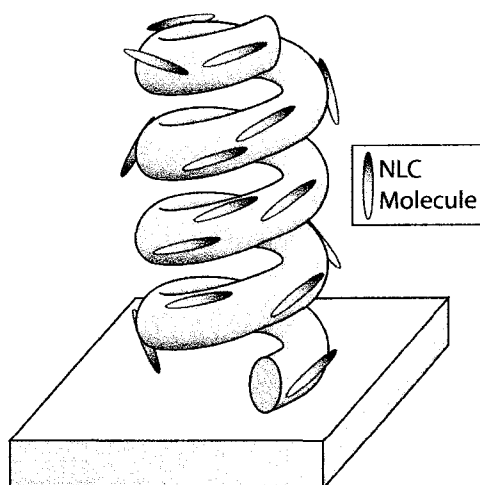


Figure 4.5 – Schematic representation the induced alignment of rod-like NLCs by a chiral GLAD film.

4.2.3.1 Fabrication of Chiral GLAD films

A comprehensive collection of helical GLAD films was fabricated to investigate the effect of several different parameters controlled by the GLAD deposition process.

Three common optical materials, magnesium fluoride (MgF_2 , $n=1.38$), silicon dioxide (SiO_2 , $n=1.47$), and aluminum oxide (Al_2O_3 , $n=1.66$) were deposited on 2.5cm x 2.5cm Corning 7059 glass substrates by thermal evaporation for MgF_2 films, and by electron beam evaporation for SiO_2 and Al_2O_3 films. By varying the material of the chiral films it was expected that the circular birefringence would be modified due to the changing the bulk index of refraction. In addition to the effect on the circular birefringence of unfilled or 'dry' films without added NLCs, by fabricating films using several compounds the interaction of the NLC molecules with the different materials could be investigated.

Helical GLAD nanostructures are some of the most easily fabricated nanostructures. Only three parameters are required as input to the control system, the angle of incidence, α , the helical pitch or amount of vertical film growth per complete revolution of the substrate, Φ , and finally the overall thickness specified through the total number of turns (fractions of a turn are allowed). To deposit the helical nanostructures, the angle of incidence is fixed and the substrate is rotated at a constant rate relative to incoming flux rate. This rotation rate is responsible for the helical pitch: a faster spin rate results in smaller pitches while a slower rate produces helices with larger pitches.

The angle of incidence, α , greatly influences the structure of GLAD films and is important in the production of chiral optical films. As the angle of incidence gets more oblique and α gets closer to 90° , the porosity of the films increases significantly. To investigate this effect, sets of SiO_2 and Al_2O_3 films were fabricated at a range of incidence angles from 83° to 86° , all still in the GLAD regime with highly porous structures.

In addition to the variation of material and angle of incidence, sets of films were fabricated to investigate the nanostructural parameters of helical pitch (vertical rise per complete turn of the helix), film thickness and handedness of the chiral structure. These parameters relate to the magnitude, wavelength dependence and direction of the chiral optical effects, respectively.

4.2.3.2 Addition of NLCs

A regimented procedure was used to create hybrid devices of NLC filled GLAD films. To fill the films, the square substrate with deposited chiral GLAD film was first placed on a hotplate and heated to 65°C. This step was included to drive off any water condensation from ambient humidity that might be present in the porous film structure and would prevent complete filling by the NLC molecules. After several minutes the film was then placed on a photoresist spinner where approximately 200 μL of NLCs were dropped by micropipette onto the spinning substrate (see representative schematic, Figure 4.6). The spinner was set to spin in two stages, first a slow spread setting of 500 rpm while the NLCs were added, followed by a faster spin at 2200 rpm for 40 seconds to remove any excess NLC sitting on top of the film structure. The results showed good uniformity with little evidence of ‘domains’ commonly associated with the filling process.

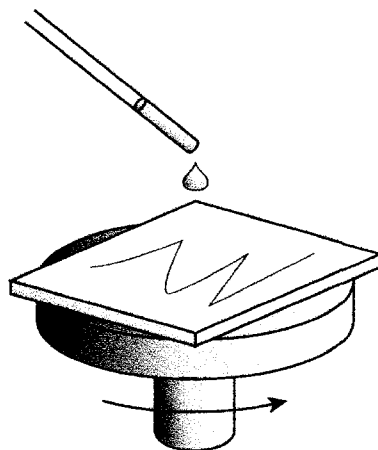


Figure 4.6 – Filling of chiral GLAD films with NLCs. The film was first heated to drive off any condensed moisture, and the NLC was dropped onto the rotating sample. As the films are hydrophilic the NLC is easily incorporated into the nanostructure. A final high-speed spin was used to remove any excess NLCs.

The NLCs used throughout this research were the nematic variety, Merck ZLI-4792. These molecules have an average index of refraction of 1.531 at 550nm with anisotropic molecular birefringence of $\Delta n = n_e - n_o$ from 0.105 to 0.095 across the visible spectrum. They have an isotropic clearing temperature of 92°C, slightly higher than the temperature to which the films were heated before the addition of the NLCs.

There are several benefits to the addition of NLCs to GLAD films. First, the high porosity of the films in combination with the optical materials used to fabricate them creates a hydrophilic structure whose optical properties may be influenced by environmental conditions. By filling the film with NLCs and preventing the water from ambient humidity from entering the structure, we expect to reduce the sensitivity to humidity observed in porous, unfilled films [139]. Second, the contrast of high/low index of refraction at the many film-air interfaces of the unfilled cells produces a large amount of scattering, reducing overall transmission. By reducing the difference in the index of refraction across these interfaces by the addition of liquid crystals, the appearance of the films changes from a frosty white characteristic of scattered light (unfilled), to nearly transparent (filled). Finally, as mentioned above, the anisotropy of the NLC molecules can be ordered by the structure of the film, aligning the NLCs to create cells with larger rotatory power.

4.2.3.3 Measurement of optical activity

To characterize the optical response of both the chiral GLAD films and the GLAD/NLC hybrids, optical activity, or the rotation of linearly polarized light, was measured in transmission mode. Shown in Figure 4.7 is a schematic of the optical setup. The light source and detector were integrated components of a Perkin Elmer Lambda 900 spectrophotometer providing intensity measurements as a function of the specified, monochromatic wavelength. The beam path was from the output of the spectrophotometer (depolarized) into the closed magnetic optical bench housing the rotating polarizer, film sample, fixed analyzing polarizer and integrating sphere detector. Typically, in optical activity measurements the analyzer is rotated to determine the outgoing polarization vector; however, in this system it was only possible to rotate the initial polarizer, thus the analyzer was fixed at a known orientation.

The samples were placed with the glass substrate perpendicular to the beam path and the beam incident on the film side. The polarization vector of the incoming light was known from the polarizer position and the angle made relative to the fast axis of the analyzer was determined from an initialization scan performed without a sample present. The extinction method was used to find the orientation of the polarization emerging from

the film whereby the minimum in transmission for each wavelength corresponded to the fast axis of the analyzer being at 90° to the polarization vector. The form of the emerging wavefront was not truly linearly polarized due to the effects of circular dichroism, however this method allowed for the determination of the orientation of the major axis of the ellipse corresponding to pseudo-linearly polarized light. The orientation of this axis relative to the polarizer orientation was defined as the optical rotation due to the sample.

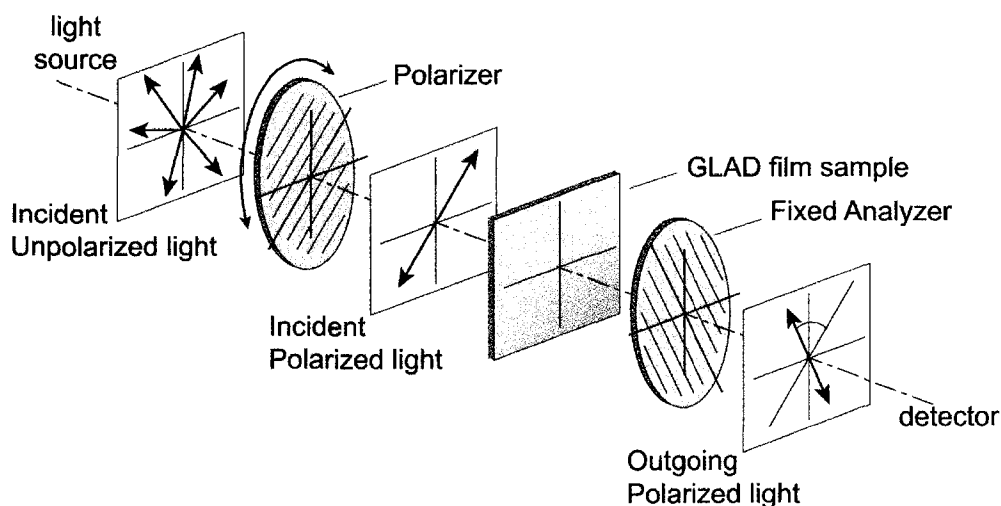


Figure 4.7 – Experimental setup for measurement of optical activity in chiral GLAD films. The apparatus consisted of two achromatic polarizers, one serving as a rotating polarization source and the other as a fixed analyzer with a known orientation. When an optically active film is placed in the beam path, the orientation of the incident polarizer was adjusted to minimize the signal at the detector.

4.3 Results

The following sections evaluate the effect of underlying structural changes on the optical activity and associated chiral optical response of GLAD thin films and NLC hybrids. These results were compiled in an attempt to predict the optical properties of various films both with and without the addition of NLC molecules so that it might be possible in the future to accurately engineer thin film-based devices with the desired characteristics.

4.3.1 Film density manipulation by deposition angle

GLAD films are unique in that they are deposited at extremely oblique angles of incidence so that self-shadowing dominates the growth and produces highly porous films. The structure of the films is very sensitive to the angle of incidence in the GLAD regime (80-90° from normal), as can be seen in the films of Figure 4.8. In addition to the nanostructural differences of changing α , the increased porosity means that for ‘wet’ films with added NLCs, a larger amount of liquid can be added. This effect was investigated to determine the optimal balance between these factors.

Helical films of SiO_2 and Al_2O_3 were deposited at deposition angles from 83° to 86°, and the rotatory powers of the films, defined as the magnitude of maximum rotation per unit thickness of film, were plotted against these angles. It is important to note that in an anisotropic chiral medium, rotatory power is not exclusive and independent of the film thickness due to the non-zero rise angle of the chiral structure that quantizes the number of helical rotations of the film. However, in the short wavelength regime, it has been shown to be a valid means of comparison with other types of mediums [124]. This range of angles was chosen for α as at smaller angles the films become too dense to allow for filling by liquids such as NLCs, the main focus of this research, and at larger angles the deposition rate is too slow to be practical due to the cosine dependence of flux on the tilted substrate.

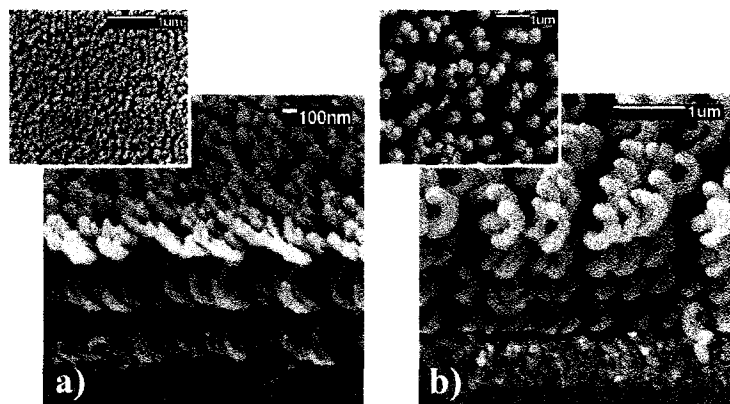


Figure 4.8 – Example of two helical SiO_2 GLAD films, a) a film deposited at 83° and b) a film deposited at 85°. The insets show the difference in porosity from a top view.

Shown in Figure 4.9 are the results of the variation of deposition angle for both unfilled and NLC filled films. For the unfilled films it can be seen that the more distinct helical structure of the films deposited at higher angles results in a subtle, but consistent increase in rotatory power. The difference in nanostructure results in greater circular birefringence as implied by the results. For the NLC filled films it is first noted that there is a substantial increase in rotatory power over the unfilled films. This increase is greater for films deposited at higher angles which is as expected due the higher porosity of these films that allows more infiltration by NLC molecules. The structure of the more oblique films may also enable a stronger chiral nematic phase to be induced in the NLC molecular order, aiding in the increase in rotatory power. Inconclusive measurements were obtained from the Al_2O_3 film deposited at 86° and as such are not included in the results. From Figure 4.9 it can be seen that ideally films should be deposited at 85° to obtain the greatest efficiency from both unfilled and NLC filled devices.

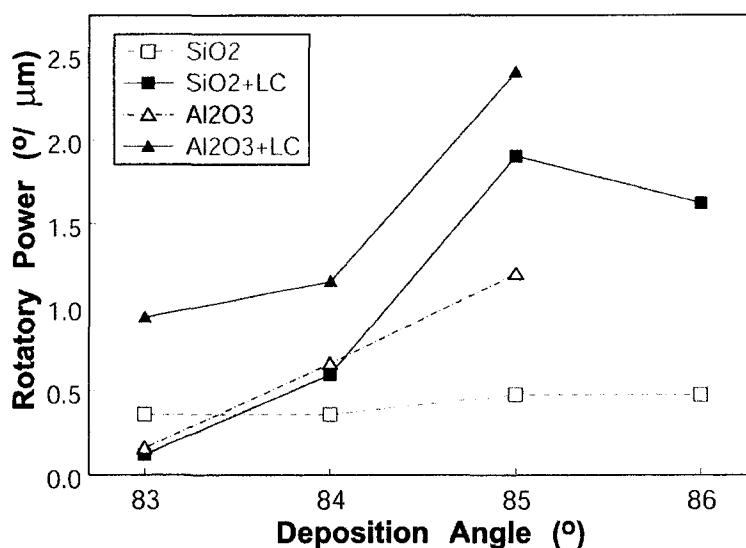


Figure 4.9 – Specific rotatory power of chiral GLAD films as a function of angle of flux incidence for both unfilled and NLC-filled Al_2O_3 and SiO_2 films.

4.3.2 Film thickness

In the previous section the specific rotatory powers of the film/NLC devices were plotted, and in doing so it was assumed these values were a constant function of film thickness. This reasoning results from the derivation of Equation 4.11, is typical for most optically active mediums, and is the expected result for both unfilled chiral GLAD films

and NLC filled hybrid devices. In an attempt to verify this result several sets of films were fabricated with increasing thicknesses and their optical activity was measured.

Three sets of helical films were fabricated from SiO_2 , MgF_2 , and Al_2O_3 and were deposited at an angle of incidence of 85° , a result of the investigation in the previous section. All films had an equal pitch of 450 ± 10 nm and their thickness was varied by the number of turns. As predicted for the unfilled films and shown in Figure 4.10 where the maximum or peak rotation for each film is plotted, the magnitude of the rotation increases linearly with thickness. Note that the rotation was taken to be positive if the direction of the rotation was opposite the handedness of the film (i.e. for a left-handed film a right-handed rotation would be taken as positive) as

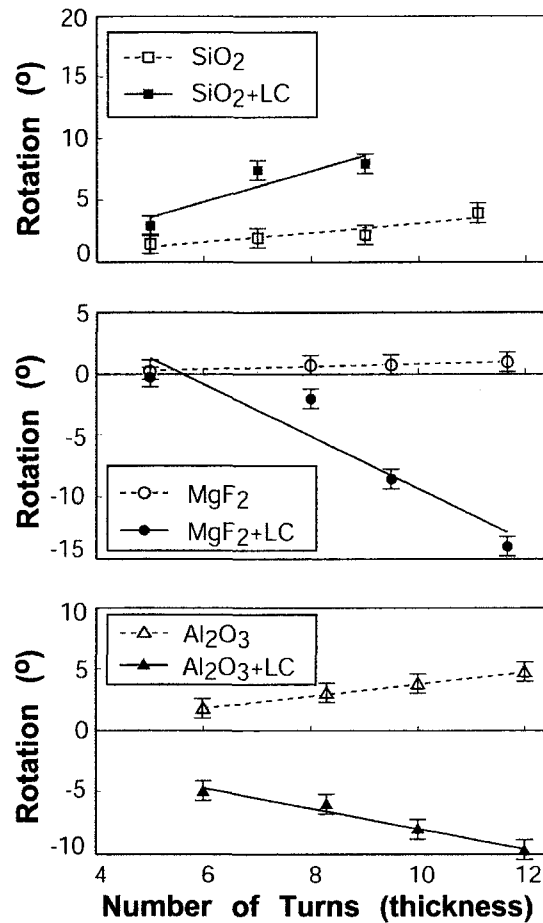


Figure 4.10 – Peak optical activity measurements as a function of film thickness for both unfilled and NLC-filled, MgF_2 , SiO_2 , and Al_2O_3 films. The addition of NLCs results in an overall increase in rotation for all film materials, while there is a reversal in direction of rotation for the NLC-filled MgF_2 and Al_2O_3 films.

predicted by the derivation of section 4.1.1. It has been shown previously [2, 48], and was confirmed in this research that the rotation direction from enantiomeric films with similar structure and opposite helical handedness is in the opposite direction. Results for the rotatory power of the unfilled films are given in the middle column of Table 4.1 along with the corresponding circular birefringence obtained at the average wavelength of peak rotation for each series of films. The index of refraction of the film materials can be seen to play an important part in the magnitude of rotation through its effect on circular birefringence. The greater rotation exhibited by the SiO₂ over the MgF₂ films, and even greater by the Al₂O₃ films, is as expected due to the higher bulk index of refraction of those materials resulting in greater optical anisotropy as seen by incident circularly polarized light.

Material	Measured effective rotatory power, °/μm		Circular Birefringence $ n_L - n_R $	
	Film	Film + LC	Film	Film + LC
MgF ₂	0.16	-2.42	0.028	0.42
SiO ₂	0.67	1.34	0.12	0.23
Al ₂ O ₃	1.05	-2.30	0.18	0.40

Table 4.1 – Measured rotatory powers for both unfilled and NLC-filled MgF₂, SiO₂, and Al₂O₃ films. Also included are calculated values of the corresponding circular birefringence. Note that the reversal in sign for rotation by the filled films represents a rotation in the opposite direction from the convention.

The addition of NLCs to the films results in several important observations. Shown in Figure 4.10 are the results of optical rotation measurements performed on the NLC filled films and they are seen to agree with the predicted linear relationship between device thickness and optical rotation. As expected, there is also a significant enhancement in the overall performance of the hybrid devices. In Table 4.1 are the comparisons of specific rotatory powers of the ‘dry’, unfilled films with the NLC filled devices. In particular, there was a large increase in the rotation obtained from NLC filled MgF₂ films while the SiO₂ and Al₂O₃ film-based devices saw a doubling of the rotation upon the addition of NLCs. The difference in the amount of increase among film

materials is possibly due to a saturation of the optical properties by the NLCs whereby the relative volume of film to NLC molecules sets the upper limit on the maximum rotation and the remainder of the response is then governed by the index of refraction of the film material itself.

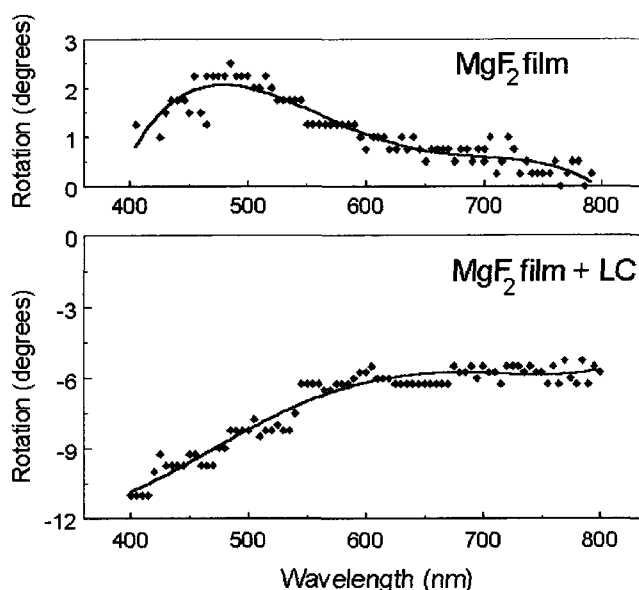


Figure 4.11 – Rotation measurements for a 6 μm thick MgF_2 film on glass, without the addition of NLCs (top), and with the addition of NLCs (bottom). The hybrid device gives almost six times the rotation of the film alone. Note the reversal in rotational direction along with the shift in wavelength of peak rotation to lower values after the addition of the NLCs.

Aside from the increase in the magnitude of rotation by the NLC filled films over the unfilled films, the most significant observation of these tests was the existence of a reversal in the direction of rotation upon the addition of NLCs to the MgF_2 and Al_2O_3 films. The graphs of Figure 4.10 have been plotted using the convention for positive rotation mentioned above, where a negative rotation is indicative of the rotation direction being opposite to that predicted by the form birefringence of the film. The SiO_2 films did not show a similar reversal in the direction of rotation, yet films of all three materials with included NLC molecules exhibited a similar increase in the magnitude of rotation. The trend of gradually decreasing rotation with increasing wavelength was observed in all measurements, implying that the visible spectrum under investigation lay to the right

of the Bragg resonance wavelength for all films, in tests with and without NLCs (see Figure 4.11), and that the change in rotation direction was not simply characteristic of a wavelength shift of optical response to the opposite side of the resonance peak. Although the exact mechanism of NLC/thin film interaction is not well understood, it is possible that the material interface with NLC domains is responsible for the unpredicted behaviour. It has been suggested by colleague Andy van Popta that given a particular nanostructure and helical spacing (dependent on the material), the NLC molecules may be oriented such that they rotate the polarization in the direction opposite to the film structure due to NLC domain interactions with individual helical structures [140]. It is likely that the spacing and structure of the MgF₂ and Al₂O₃ films suits this type of alignment and results in a rotation opposite that of the unfilled film. A comprehensive study of this phenomenon is underway to more accurately predict such behaviour.

4.3.3 Wavelength properties of chiral thin films

The response of a chiral medium to different wavelengths of incident light varies significantly due to dimension-specific structural effects. As mentioned above in section 4.1.3 for a biaxial chiral medium such as a helical GLAD film, there is a predicted peak in rotation for the critical wavelength, λ_c , satisfying the Bragg condition, of Equation 4.13 [118, 119]. At this critical wavelength, resonance should occur where the rotation is a maximum (ideally infinite corresponding to the emergence of purely circularly polarized light) or, for transmission measurements of the films, where there is the largest difference between transmission of left and right circular polarizations of light. In an ideal model of optical activity, the rotation should change from $+\infty$ to $-\infty$ as one proceeds to lower wavelengths from the critical value; however, for mediums with a finite thickness and minor surface imperfections due to microscopic roughness like the films tested in this research, only a finite rotation is seen.

For unfilled biaxial chiral GLAD films, a plot of wavelength of maximum rotation, or critical wavelength, versus helical pitch of the film structure is shown in Figure 4.12. As the peak in each rotation spectrum is difficult to determine accurately, large error bars are present and were a result of the uncertainty in determining the global maximum for the peak response; however, the increasing trend in critical wavelength

with increasing pitch implies some accuracy of Equation 4.13. Such ease in tuning of the wavelength properties makes chiral GLAD films suitable for many applications, and modified structures such as graded pitch helices can be used to increase the bandwidth of the devices [125, 141].

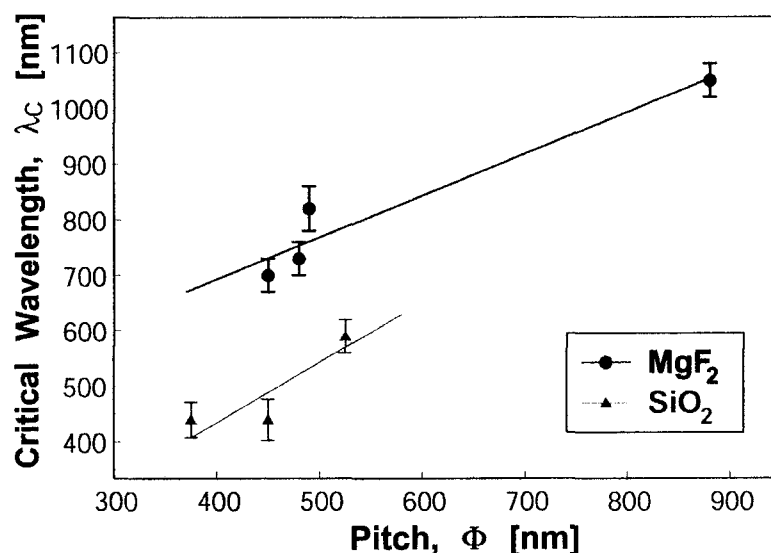


Figure 4.12 – Critical wavelength as a function of helical pitch for unfilled MgF_2 and SiO_2 films. A linear relation between these two quantities is predicted by theory.

The wavelength properties of NLC filled devices are expected to follow a similar relationship to that of the unfilled films, particularly given that the structural backbone of the GLAD films provides a mechanism for ordering of NLC domains. By changing the pitch of the underlying helical film, the wavelength response should change appropriately. This trend was, in general, observed for NLC filled films although the critical wavelength was not as clearly defined for hybrid devices as a peak in the spectra was somewhat ambiguous. As the effective index of refraction of the thin film hybrid device changes due to the addition of NLCs, one expects an associated shift in the critical wavelength for the filled films over the unfilled films as per Equation 4.13. The average index of refraction of the ZLI-4792 NLCs is much higher than the air of the gaps of the unfilled film, and as such one would expect the critical wavelength to shift to higher values upon the addition of NLCs to the films. A shift in wavelength was consistently observed, however it was to smaller wavelengths, opposite the direction predicted. Shown in Figure 4.11 are plots of the optical rotation as a function of wavelength for an

MgF₂ film with, and without added NLCs. The peak for the unfilled film appears at 490 nm, while the peak for the NLC filled film lies to the left of the visible spectrum under investigation (400-800 nm), shifted to lower wavelengths. Note that the reversal in direction of rotation is also shown in this figure for the NLC filled film. The unpredicted shift in critical wavelength to lower wavelengths at this time is not fully understood, but the root of such behaviour might lie in interaction mechanisms similar to that responsible for the negative rotation of NLC filled films.

4.4 Conclusions

Porous, helical thin films deposited using the GLAD technique have been shown to exhibit circular birefringence and optical activity through their natural chiral nanostructure. The addition of NLCs to the porous thin films, a procedure not possible with many other chiral mediums, represents a method of not only enhancing, but also of dynamically controlling the optical properties of the hybrid devices. Chiral GLAD thin films are easily tailored through the custom substrate motion parameters and it has been found that a wide range of optical properties can be modified using this variable structure-based technique.

The porosity of the films that uniquely allows for filling by liquid crystals was seen to reach a compromise between nanostructural ordering and film density when deposited at angles of 85°. This angle lies in the middle of the GLAD range, and allows for accurate control over other variables such as structure and pitch. By altering the chiral pitch of the helices, it was found that the wavelength properties of the device could be altered within the visible spectrum. This ability to tune the structure can provide control over the colour properties of a display based on similar fabrication technologies.

The addition of NLCs to the structured thin films showed a marked improvement in the optical response of the films, particularly for low index materials such as MgF₂. Other higher index materials such as Al₂O₃ and SiO₂ exhibited a similar, albeit smaller improvement in the response, which was possibly due to the saturation of the optical properties by the NLCs. For the MgF₂ and Al₂O₃ films, the enhancement accompanied a reversal in the direction of rotation that was possibly due to a chiral nematic order

induced by the film nanostructure in the direction opposite the handedness of the film. In addition to the direction reversal, for all films the addition of NLCs caused a shift of the wavelength properties to smaller values, in a direction opposite from the predictions based on traditional chiral mediums.

Although a great deal more study is required to accurately produce devices for imaging and photonics applications, this initial research provides insight into the response of chiral thin film/NLC hybrids. The tuneable nanostructure of the films and the ability to externally control the transmission and polarization characteristics will undoubtedly allow for the future fabrication of devices based on this dynamic technique.

5 Chapter 5

Graded Index Antireflection Coatings

¹⁰In this chapter the design, fabrication and characterization of a novel porous antireflection coating is presented. Using a modified GLAD technique, SiO₂ films were deposited on glass to provide extremely high transmission over a large range of wavelengths. The optical response of the films is characterized by the structural parameters to determine the ideal deposition parameters for producing tailored devices. The wavelength properties are investigated along with transmittance at oblique incidence and both show significant improvements over single layer interference coatings.

5.1 Antireflection coatings

When light is incident upon an interface between two different mediums, Fresnel reflection of a portion of the wavefront can occur due to the mismatch in refractive indices. We can see this effect on a calm lake surface where the light travelling through the air reflects from the surface of the water having a higher index of refraction. Although in this case the effect is desirable, other more unwelcome instances can be found where reflections from transparent materials such as glass can reduce the transmission of light by more than 4% per surface, causing glare. To reduce the reflection from these interfaces and increase overall transmission, antireflection (AR) coatings are often applied to the surfaces of glasses and other materials. Applications of AR coatings can be found in such fields as solar cells where the overall efficiency depends on maximizing the amount of light passing through the protective glass covering [143, 144], in high powered lasers where even a fraction of a percent reflection from windows can be hazardous or can degrade its performance [145, 146], or even more simply in the production of window glazing or prescription glasses [147]. AR coatings can also be applied to higher index materials such as silicon where interfaces with air can

¹⁰ Portions of this chapter were excerpted with permission from [54] S. R. Kennedy and M. J. Brett, "Porous Broadband Antireflection Coatings by Glancing Angle Deposition," *Appl. Opt.*, vol. 42, pp. 4573-4579, 2003. Copyright 2003 Optical Society of America.

be problematic and produce large reflections due to the significant mismatch in propagation speeds on either side of the interface [148].

AR layers are typically divided into two types. The first type uses the principle of interference from reflected wavefronts at the interfaces in combination with precise phase shifts from one or many thin film layers to eliminate backward reflection. This technique can produce favourable coatings with virtually 100% transmission, however, it often requires the deposition of many layers with precise thicknesses and properties [14, 149]. One downfall to this technique is the dependence of interference on the relative phase shifts of each layer. At wavelengths far from the design specifications, as well as non-normal angles of incidence, the associated phase shift for each film layer deviates considerably from the desired value and the overall transmission is reduced due to imperfect destructive interference. The second type of AR interface avoids the requirement of precise thicknesses by employing an intermediate layer that forms a gradient between the two different types of propagation mediums [150]. This gradual change in index reduces reflection by avoiding interfaces with large index mismatches. To create such an AR layer, mixtures of materials in the case of the interface between two solids, or porous materials in the case of an interface with air, is applied in such a way as to create a gradual change in the optical properties throughout the intermediate AR layer. Graded index coatings do not suffer from the same limited bandwidths and angular dependence that solid thin film layers do as there is not the same emphasis on precise phase relations, however they do have some tradeoffs as they are more delicate due to their fine structure, they suffer from scattering, and cannot be easily fabricated to attain perfect 100% transmission. In the following chapter, a new fabrication technique is presented using GLAD to produce high quality graded index coatings for large bandwidth AR applications.

5.2 Porous antireflection coatings

5.2.1 Graded index AR coatings

Graded index AR coatings were first observed over a hundred years ago by Fraunhofer when he etched a piece of glass with an acid solution to produce a porous

interface [151]. By creating small pores in the glass surface, the mixture of mediums (air and glass) served to decrease the macroscopic index of refraction of the layer. Such a reduction is due to an averaging of the indices of the two constituents in a manner described by an effective medium theory (EMT). It can be noted that most structured surfaces with high porosity can be used as an antireflection layer, and this effect was investigated in a biological system where the regular array of projections on the surface of a moth's eye served to reduce reflected light [152]. From this discovery, the term 'moth eye' surfaces was coined to describe antireflection layers that used a graded interface composed of vertical projections to reduce the index mismatch [153].

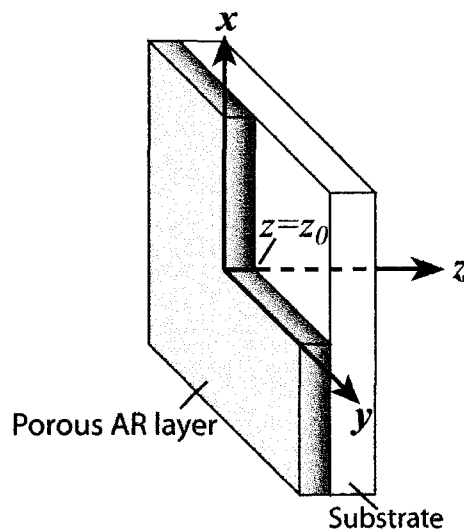


Figure 5.1 – Coordinate system used to describe the porous AR coatings. The film has thickness z_0 and the xy plane is parallel to the substrate.

As reflection is primarily due to discontinuities in material properties manifested by a difference in phase velocity and hence index of refraction at the surface of interest, an ideal antireflection coating would eliminate any abrupt change in the refractive index. In addition to this requirement, to obtain higher transmission values through the layer it is desirable that higher order derivatives of the index of refraction be continuous throughout its thickness, most notably at the interfaces between the air and coating, and the coating and substrate. These secondary requirements are a result of constraints on the phase continuity of the incident wave. Using these constraints it has been shown that the improvement in reflectivity offered by the continuity of higher order derivatives is limited by an increasing gradient at the midpoint of the film thickness, and the optimal

compromise between these effects is found when requiring continuity of only the first two derivatives [154, 155]. If, we define our coordinate system such that the plane of the film is the xy plane, and $z = 0$ is the interface between the AR film and air, as shown in Figure 5.1, with the positive direction normal and toward the surface of the substrate, the boundary conditions can be written for the index of refraction as a function of optical thickness, $n(u)$:

$$n(0) = 1 \quad (5.1)$$

$$n(u_0) = n_s \quad (5.2)$$

$$\left. \frac{dn}{du} \right|_{u=0} = \left. \frac{dn}{du} \right|_{u=u_0} = 0 \quad (5.3)$$

$$\left. \frac{d^2n}{du^2} \right|_{u=0} = \left. \frac{d^2n}{du^2} \right|_{u=u_0} = 0 \quad (5.4)$$

where u_0 is the total optical thickness of the AR layer, and the overall interface is between the substrate with index of refraction n_s , and air with $n = 1$. Optical thickness is used instead of physical thickness in these definitions to simplify calculations, and is defined by

$$u = \int_0^z n(z') dz' \quad (5.5)$$

A candidate functional profile for the index of refraction that satisfies these conditions is a fifth order polynomial [154],

$$n = n_s - (n_s - 1) \left\{ 10 \left(\frac{u_0 - u}{u_0} \right)^3 - 15 \left(\frac{u_0 - u}{u_0} \right)^4 + 6 \left(\frac{u_0 - u}{u_0} \right)^5 \right\} \quad (5.6)$$

As it is often more convenient to work with physical thickness rather than optical thickness when considering the actual fabricated films, we use the definition of optical thickness to obtain the index of refraction as a function of physical thickness by solving

$$z = \int_0^u \frac{du'}{n(u')} \quad (5.7)$$

The result has an index of refraction profile shown by the dashed line in Figure 5.2.

The quintic, or fifth order polynomial as a function of optical thickness, although ideal, does not, however, allow for the simple mathematical calculations needed to produce actual film density profiles. For this reason, the gaussian function has been used with much success and as seen by the continuous curves of Figure 5.2, its profile closely matches that of the ideal quintic polynomial [156, 157]. One advantage of the gaussian profile is the ability to tune the profile of the density through a single decay parameter. As here we are concerned with fabricating actual coatings with characteristics that may deviate slightly from the ideal model, this variable allows for fine-tuning of the AR film's optical response.

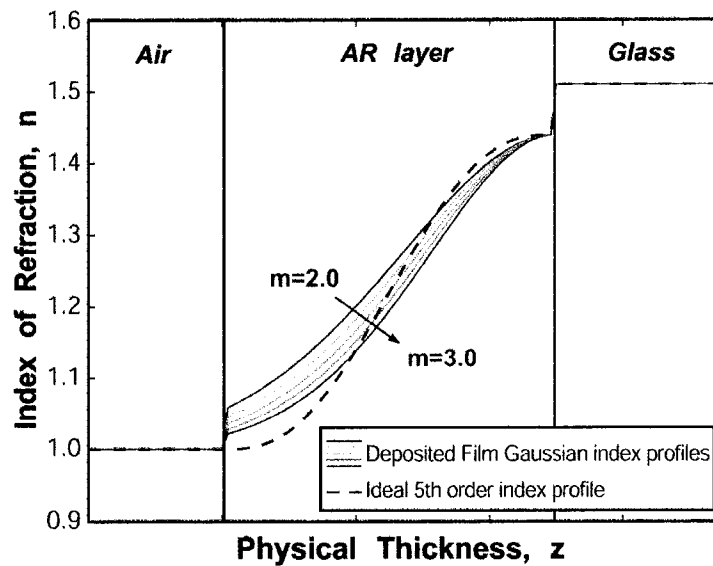


Figure 5.2 – Refractive index profiles for SiO₂ GRIN GLAD antireflection coatings on 7059 glass. The solid lines show the gaussian profiles for the fabricated films with profiles varied through the variable decay constant, m , while the dashed line is the profile given by the 5th order polynomial constrained by the practical limitations of the system.

5.2.2 GLAD graded index AR films

Traditionally, porous broadband AR coatings for high dielectric materials have been fabricated by chemical etching of the substrate [156, 158], however GLAD offers a

new technique for fabricating films with the precise porosities and structure necessary for high quality coatings. As highlighted in the previous chapters, thin films deposited at non-normal angles of incidence have densities less than that of the bulk material due to the effects of self-shadowing, a process that is critical to the fabrication of GLAD nanostructures. The angle of incidence thus offers the ability to control the density of a film and produce vertical projections characteristic of porous ‘moth eye’ AR coatings. For the GRIN GLAD films produced in this research, SiO₂ was deposited by electron beam evaporation onto 7059 glass substrates with known optical properties.

5.2.2.1 Fabrication of customized density profiles

To produce the gradual change in porosity required for graded index GLAD films (GRIN GLAD), the angle of incidence is varied from normal ($\alpha=0^\circ$) to highly oblique angles ($\alpha\approx 90^\circ$) resulting in films with porosities graded from low to high respectively. This concept was fundamental in work by Robbie *et al.* [49] where sinusoidal variations in density were produced by depositing at a range of oblique angles resulting in rugate filters. From work by Tait *et al.* [47] described in section 1.3.5.2, the density of an obliquely deposited film was modeled as a function of the angle of incidence. Shown in Figure 5.3 is a schematic of the effects of film fabrication at a range of deposition angles, where one can see that by increasing α as the deposition progresses, a gradation in the density profile is produced. By inverting Tait’s density equation, we can obtain a guide for the angle of incidence as a function of a chosen density profile, $\rho_r(z)$. The result is given by the expression

$$\alpha(z) = \cos^{-1} \left\{ \left(2\rho_r(z)^{-1} - 1 \right)^{-1} \right\} \quad (5.8)$$

This formula then provides a means of controlling the functional shape of the density simply by changing the angle of incidence, α , while the density profile is the gaussian described above and is given by the expression

$$\rho_r(z) = \frac{\rho(z)}{\rho_0} = e^{-m \left(\frac{z_0 - z}{z_0} \right)^2} \quad (5.9)$$

where m is the decay constant responsible for tuning the optical response. Note that the density is relative and is normalized to the bulk density of the material so that this result may be used for AR coatings fabricated from a wide variety of materials. The gaussian function of Equation 5.9 is plotted in Figure 5.2 with a range of values for m and is compared to the more ideal quintic polynomial function to show its likeness.

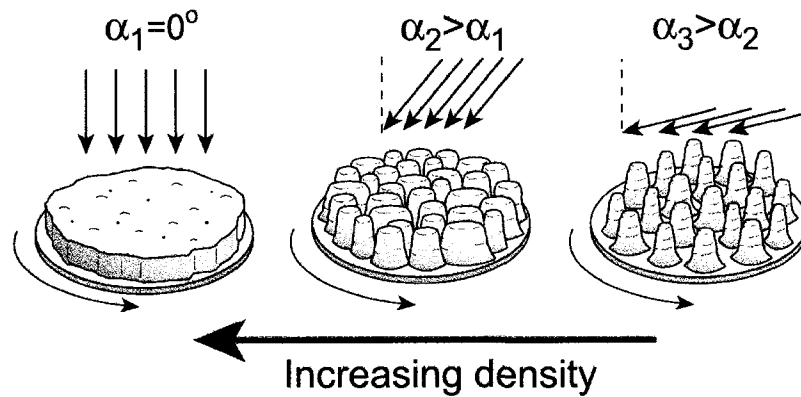


Figure 5.3 – Schematic of how the GLAD process is used to fabricate graded index films. By increasing the angle of incidence the deposited film decreases in density while rotating the substrate throughout the deposition produces vertical projections.

Two discontinuities in the profile of the index of refraction for the AR layer can be seen in the plot of the gaussian density profile, Figure 5.2. As has been mentioned above, discontinuities in the index are undesirable due to Fresnel reflection and can reduce overall transmission through the device, however when fabricating actual devices practical constraints limit our ability to create a perfectly smooth transition across the layer. At the air/AR interface the minimum density of the film is found to be approximately 17%, somewhat larger than the fractional percentage desired for a smooth function. This step in density cannot be overcome by the simple one step process used to produce GRIN GLAD films; however, from calculations the difference in the index across this interface is less than $\Delta n=0.05$, producing a Fresnel reflection of only 0.06%. At the AR/glass interface the step in the index profile is due to a mismatch of materials. Ideally one would deposit the same material as the substrate for a perfect index match at the interface; however, to maintain stoichiometry of deposited materials, simpler compounds must be used. In this research, SiO_2 ($n_{\text{SiO}_2}=1.44$) was deposited on Corning 7059 barium borosilicate glass ($n_{\text{glass}}=1.53$), producing a step discontinuity of $\Delta n=0.09$

that from calculation results in a reflectivity of only 0.09%. From these two imperfections in the profile, the predicted reflectivity is small at 0.14% resulting in a theoretical maximum transmission for the worst-case films of 99.86%. As will be seen in the results obtained from actual films, this maximum was obtained and even surpassed for optimal films with profiles carefully chosen to reduce the minimum film density at the air interface.

From Equation 5.8, for a chosen density profile given by $\rho_r(z)$, the motion for α is set when fabricating a GRIN GLAD AR coating. One difficulty, however, when fabricating films for a wide range of angles of incidence is that the non-normal growth angle at more oblique angles of incidence results in different deposition rates relative to that measured by the CTM during the deposition. To overcome this difficulty that would result in greater deposition rates at lower values of α and cause the film produced to have a density profile differing substantially from the desired function, an empirical correction factor as a function of α was included in the control software so that film thickness calculated by integration of the deposition rate matched that of the actual film. This ratio of rates for the system used in these depositions was found from experiment to be

$$\frac{R_{film}}{R_{CTM}} = -0.00014\alpha^2 + 0.0033\alpha + 0.98 \quad (5.10)$$

The varying geometry in different systems along with the deposition of different materials will undoubtedly result in different functional values for this ratio used in correcting the input deposition rate, but the expression above is included as an indication of the form of the relationship.

5.2.2.2 Fabrication of vertical projections

A high quality AR coating should allow for the transmission of all polarizations of light regardless of its form and thus the layer should show no linear or circular birefringence. The rotation of the substrate about the axis normal to its surface is responsible for the ultimate shape of the resulting structure and it is this shape that is subsequently responsible for the form birefringence of these types of porous films, as seen in Chapter 4. To remove any structural anisotropy that would create a birefringent

or dichroic film, the film structure should be uniform with respect to the in-plane dimensions. Ideally, the projections would have the form of inverted cones arrayed randomly across the surface with the relative density for a cross section taken at height z corresponding to the function $\rho_r(z)$ used to set the angle of incidence, α . To produce such structures, the substrate is spun rapidly at approximately 3 rpm (ϕ motion) so that the flux is distributed evenly around each of the projections. For the fabricated GRIN GLAD AR films the pitch, or vertical growth per complete rotation, of the substrate was 30 nm, and was limited by the maximum rotation speed of the stepper motor at a reasonable CTM deposition rate of approximately 10Å/s. An example of the resulting structure is shown in Figure 5.4 and as can be seen from the scanning electron micrograph the film did show some chiral structure due to the nature of the deposition process. The small pitch did not produce any measurable circular birefringence for the visible wavelengths under investigation, and no linear birefringence was seen for incident wavefronts parallel to the plane of the substrate. Both measurements were performed with an achromatic Glan-Taylor polarizer, while an achromatic quarter-wave plate was used to produce the two circular polarizations. Within the noise resolution of 0.1%, no discernable difference between orthogonal modes was seen for transmission measurements. From Figure 5.4 the gradation in density can also be seen where the portion of the film near the substrate is composed of more dense structure while at the air interface there are large pores separating individual nanostructures.

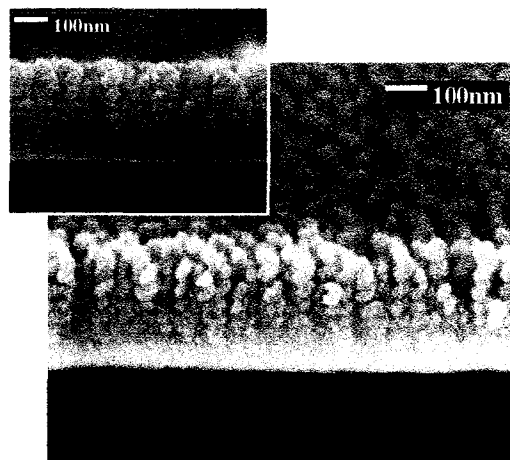


Figure 5.4 – Scanning electron micrographs of a sample GRIN GLAD film. Note the higher density of the film closer to the substrate shown by the change in contrast of that part of the image.

5.2.2.3 GRIN GLAD characteristic dimensions

The production of graded index AR films relies heavily on the ability to produce high porosities with small characteristic dimensions. Both the optical interactions with the layer and the EMT used to substitute the porous layer with a continuous one are dependent on the dimensions of the projections of a moth-eye AR coating. To avoid non-zero order diffraction effects and differentiation of the wavefronts across the surface of the AR layer, the characteristic dimensions must be much smaller than the visible wavelengths for which the coating is designed. ‘Small structures’ are typically described as being of such dimensions that it requires several periods to equal one wavelength of light [105]. For AR coatings on glass the desired spectral window has a minimum wavelength of 400 nm, thus requiring dimensions to be small in comparison.

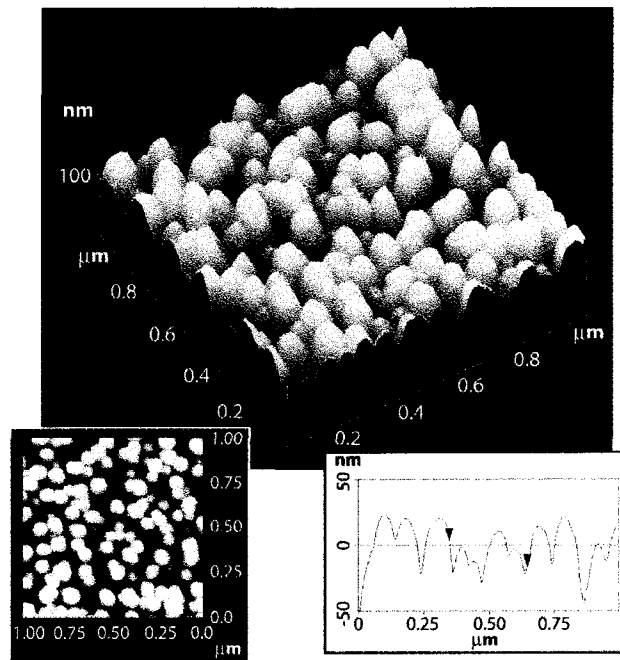


Figure 5.5 – Surface profile of a GRIN GLAD film produced by tapping mode atomic force microscopy. The two insets show top and cross-sectional views.

A tapping mode atomic force microscope (AFM) scan was performed on the surface of the GRIN GLAD AR films to determine the characteristic dimensions and shape of the vertical projections used to reduce the index mismatch. Shown in Figure 5.5 is an isometric reconstruction of the surface from an AFM scan on a gaussian profile film

with $m=2.5$. Shown in the inset on the left is a top view while on the right is a cross section taken through the middle of the $1\ \mu\text{m} \times 1\ \mu\text{m}$ sample area. It is important to note that the stylus tip of the AFM cannot always penetrate to the bottom of each void and as such the representation of Figure 5.5 below the top surface must not be considered as completely accurate. As can be seen in the figure, the projections are in the form of inverted cones with dull tips, close to the desirable form. At the top surface, Fourier harmonic analysis of the data resulted in values of 31 nm and 143 nm for the average diameter and spacing of the projections respectively. These values are small when compared to the visible wavelengths of importance for AR coatings and permit the use of EMT in modelling the index of refraction for the porous layers. Table 5.1 presents a summary of the GRIN GLAD structure dimensions.

Film Property	Value (nm)
Avg. Column Spacing	143
Avg. Column Diameter	31
RMS Roughness	19

Table 5.1 – Characteristic dimension values of an SiO₂ GRIN GLAD film obtained from Fourier analysis of a tapping mode AFM scan.

5.3 Effective medium theory

5.3.1 Fundamentals of EMT

Graded index AR layers are fundamentally based on the application of an appropriate effective medium theory (EMT) that reduces the porous mixture of the coating to a homogenous layer with dielectric properties representing some average of the constituent materials [105, 106, 159-162]. For mixtures of a dielectric such as SiO₂ and air, the polarizability of individual dielectric particles reduces the electric field within the inclusions, consequently increasing the field outside the polarizable entities to a value greater than the space average field. Resultantly, the dielectric constant of the layer is increased. This change in the macroscopic properties of the material due to microscopic inclusions results in an overall effective index of refraction for the layer, assuming the

wavelength of excitation is much larger than the individual particles. As has been shown above, it has been determined that for GRIN GLAD coatings illuminated with visible light, the size and shape of the individual projections meet this criterion permitting the application of EMT to the porous film structure.

EMT was first quantitatively described in works developing the molecular field concept by the 19th century researchers Clausius, Mossotti, Lorenz and Lorentz [163-166]. Their description of the effective field in a heterogeneous medium was restricted to spherical inclusions of foreign materials or voids, where the effective ‘Lorentz field’ in the mixture due to the polarizable inclusions was found to be

$$\vec{E}_{eff} = \vec{E} + \frac{4\pi}{3} \vec{P} \quad (5.11)$$

an expression that has proven to be fundamental to EMT development. In this expression \vec{E} is the space average field applied to the medium and \vec{P} is the total polarization of the medium. In the early 1900’s, J. C. Maxwell-Garnett re-derived the Clausius-Mossotti-Lorentz-Lorentz (CMLL) theory [159, 160] but based his derivation on Maxwell’s equations for propagating waves, distinguishing it from the static behaviour investigated in the original work. The majority of modern effective medium theories are based on a later paper by Bruggeman [161] in which two theories, fundamentally similar to the CMLL approach, are derived whereby the constituents of the medium are treated symmetrically and non-symmetrically respectively. For the former derivation, focus is placed on balancing the space average field from contributions both inside and outside the void while for the latter, the derivation is based solely on the effect of the random replacement of portions of a continuous medium. Both treatments may be used depending on the circumstance, but for most applications the symmetric approach is most useful.

The last, and most simple EMT was put forth by Drude [105] and can be reduced to a simple mixing equation. In this model the polarization of small inclusions is assumed to be negligible and has no effect on the surrounding electric field. Due to its simplicity, this method can be used to approximate the effective dielectric constant of a

mixture, however its accuracy for complex materials is poor compared to the Bruggeman or Maxwell Garnett (MG) derivation.

5.3.2 EMT simulation of GRIN GLAD films

For the fundamental EMTs mentioned above, with the exception of the Drude model, the inclusions of the secondary material in the background matrix are assumed to be spherical. Corrections to the derivations of effective mediums can be made for varying cases, for example, in the case of anisotropic inclusions such as elliptical cavities, three individual effective indices of refraction can be found for the three principle axes [106]. In the case of GRIN GLAD AR coatings, however, for normal incidence illumination the thin slabs of thickness dz used in calculating the overall index profile can be viewed as inclusions of circular discs taken from the cross section of the inverted cone-like projections. When light is incident normal to the substrate surface, the electric field is in the plane of these discs, corroborating the assumption that the inclusions are circular in a two-dimensional analogy. For this reason MG theory can be used for GRIN GLAD layers without any additional factors to accommodate the effect of perturbations on the electric field.

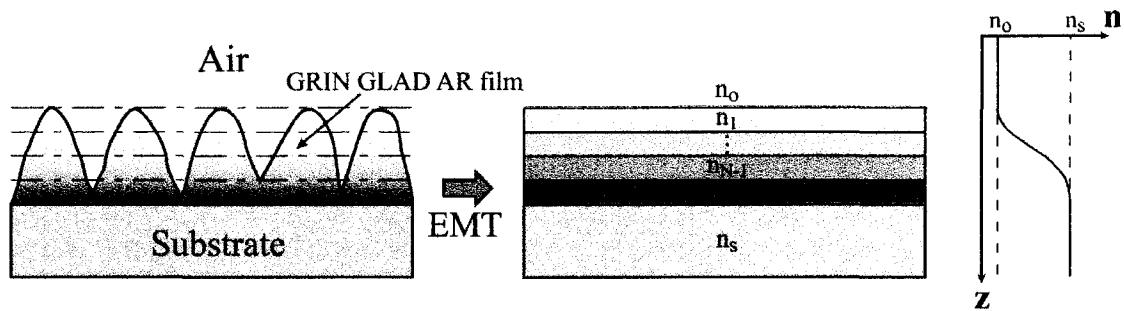


Figure 5.6 – Schematic representation of the application of effective medium theory to a GRIN GLAD film. The film is divided into a series of slabs of thickness dz , each with a calculated effective index of refraction. The profile of the index is due to variations in the film density over its thickness.

As the profile of GRIN GLAD films is a continuous function of density, the overall coating to be modelled must be broken up by reducing the layer to a series of stacked sub-layers of thickness dz . The value of $\rho_r(z)$ is calculated at the midpoint of each sub-layer and this relative density is used in the calculation of the effective index of

refraction for that segment. Shown in Figure 5.6 is a representation of the overall modelling process where the porous film is reduced to a stack of films with known index of refraction and an overall profile given by Equation 5.9.

5.3.3 Application of EMT models to GRIN GLAD

In modelling the effective index for GRIN GLAD AR coatings, two fundamental theories are used: the MG and Drude models. From Jacobssen [105], an expression for the effective dielectric constant as a function of relative density is given by

$$\epsilon = \frac{\sum_{i=1}^l a_i \epsilon_i C_i}{\sum_{i=1}^l a_i C_i} \quad (5.12)$$

where

$$a_i = \begin{cases} 1 & \text{(Drude)} \\ 1/(\epsilon_i + 2) & \text{(MG)} \end{cases} \quad (5.12a)$$

C_i is the relative density of material and ϵ_i is the bulk dielectric constant of material component i . For porous GRIN GLAD coatings, $l=2$ and in the current research the two materials used in the model are air ($\epsilon_{\text{air}}=1$) and SiO_2 ($\epsilon_{\text{SiO}_2}=2.074$). The relative density of each of the components is given by Equation 5.9 where

$$C_{\text{SiO}_2} = \rho_r(z) \quad (5.13)$$

$$C_{\text{air}} = 1 - \rho_r(z) \quad (5.14)$$

Appendix B provides the details of the overall modelling process along with sample Matlab© m-files used to calculate values for transmission of the specular beam for specific film parameters. The index of refraction for GRIN GLAD layers composed of the non-absorbing dielectrics SiO_2 and air are calculated from

$$n = \epsilon^{1/2} \quad (5.15)$$

5.3.4 Scattering from GRIN GLAD films

Scattering from the rough surface of the GRIN GLAD AR coating must also be taken into account to properly model the interaction between the film structure and incident radiation. As the incident wavelength approaches the lower limit of 400 nm, the size scale of the film's features begins to become appreciable and effects such as Rayleigh scattering can reduce the overall specular transmission. To simulate these effects, an empirical λ^{-4} Rayleigh factor was included in the transmission model.

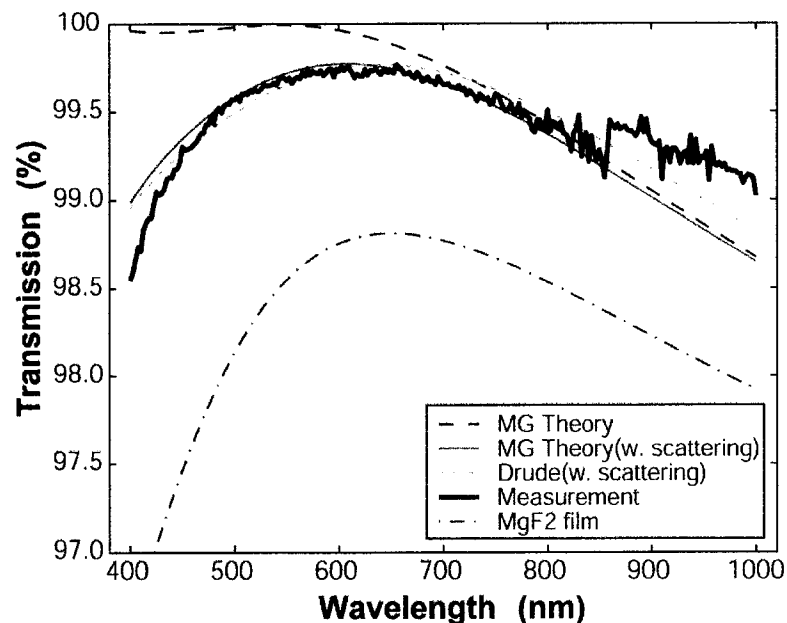


Figure 5.7 – Transmission spectrum for a GRIN GLAD film and a comparison with several models. Note the inclusion of scattering more accurately represents the measured results. For comparison, the calculated transmission spectrum for a single layer MgF₂ interference coating is also shown.

Shown in Figure 5.7 are results of both Drude and MG models graphed simultaneously with an actual transmission measurement of a GRIN GLAD film. The discontinuity in the spectrum at 862 nm is due to the spectrophotometer detector and grating change-over introducing an error of approximately 0.15%. As can be seen in this plot, both effective medium theories provide reasonable results when compared with the measured spectrum; however, outside the peak transmission portion of the spectrum, the added complexity of the MG model more accurately predicts the obtained spectrum. At shorter wavelengths, the λ^{-4} rolloff of the measured transmission due to Rayleigh

scattering can also be seen and justifies the use of the correction factor when modelling the AR coatings. The MG model with this correction is also plotted and shows good agreement between theory and results. Finally, to illustrate the effectiveness of the GRIN GLAD AR coating over a single layer MgF_2 interference coating on glass, the response of the latter has been plotted in the same figure. This ideal simulated result is for a coating tuned for optimal transmission at 550 nm and, as can be seen in the graph, the transmission is much lower than that of the GRIN GLAD film.

5.4 Antireflection results

To characterize the optical properties of the fabricated GRIN GLAD AR films, transmission measurements were performed for wavelengths in the visible and NIR range from 400 to 1000 nm. As it is often the need for high transmission through a material with a non-zero index of refraction that mandates the use of an AR film, transmission measurements, as opposed to reflection measurements, were an appropriate means of characterization. A Perkin Elmer Lambda 900 spectrophotometer with a photomultiplier (visual) and PbS (NIR) integrating sphere detector was used to obtain the spectra for each measurement configuration. As the design of the AR films calls for high porosity, it is possible that their overall performance might be affected by condensation of ambient humidity in the fine nanostructures [5, 55, 56]. To verify that this potentially detrimental property of the films was not significant in the measurements performed on them, a ‘dry’ test was done with the closed optical bench compartment purged with dry nitrogen and desiccant added. The ensuing result was compared with a measurement taken at regular relative humidity values (15-20%) and no notable difference in transmission was found indicating there is little effect on the performance of the coating from ambient moisture.

In producing graded index porous AR coatings, the goal is to reduce index mismatch and Fresnel reflection at the interfaces. As the glass substrate upon which the films were deposited had two sides and thus two interfaces from which reflection could occur, a coating would need to be deposited on both sides of the substrate to obtain the optimal transmission through the device. As the glass had known properties and the optical thickness of the substrates was large ($n_{\text{glass}} \cdot 0.8\text{mm}$) so that interference effects could be ignored, the extra deposition was not required to determine the response of just

the air/AR/glass interface. The total transmission of the device was corrected by the addition of the known reflection from the backside of the substrate. The Fresnel reflection for normal incidence at the substrate backside was calculated from

$$R = \left(\frac{n_0 - n_1}{n_0 + n_1} \right)^2 \quad (5.16)$$

with $n_0=n_{\text{glass}}=1.53$ and $n_1=n_{\text{air}}=1.0$, and this correction factor was applied to the measured spectra. To confirm this result, a measurement was performed on an uncoated glass sample and a value for reflectance of $4.39\pm 0.05\%$ across the measured spectrum was obtained, confirming the result obtained from Equation 5.16.

5.4.1 Effect of index of refraction profile

To determine the optimal profile for the index of refraction of GRIN GLAD films, a series of coatings were deposited with decay constant values, m , varying from 2.0 to 3.0. The films were all 295 nm thick and fabricated by electron beam deposition of SiO₂. By varying the parameter m , fine-tuning of the density profile is achieved whereby the resulting structure has the index profiles shown in Figure 5.2. Shown in Figure 5.8 are the results of the measured bandwidths for transmission measurements performed on the series of films. As the transmission for these films is extremely high across a large spectrum, we have chosen to define the bandwidth as wavelengths having transmission greater than 99.7% so that relative comparisons between the films could be made. Note the bandwidth is representative of real films including the effects of Rayleigh scattering, and incorporating its effect on transmission at shorter wavelengths.

Across the visible spectrum, peak transmission through the GLAD AR interface was found to be greater than 99.9% for the optimum film with $m=2.5$, and greater than 99.7% for all other films. These results also show extreme broadband behaviour and high transmission, characteristic of high quality AR layers. When compared to other accepted coatings such as a single layer of MgF₂, they thoroughly outperform their counterpart. For the $m=2.5$ film, the bandwidth is greater than 460nm, covering most of the visible spectrum and part of the NIR. From comparison of the ideal quintic polynomial profile with those fabricated with a gaussian profile, it can be seen in Figure

5.2 that for the optimal film with $m=2.5$, the ideal profile is most closely emulated with respect to both the slope and values as a function of depth, z . To produce GRIN GLAD coatings with the optimal performance, a value of 2.5 should be chosen for the decay parameter, m .

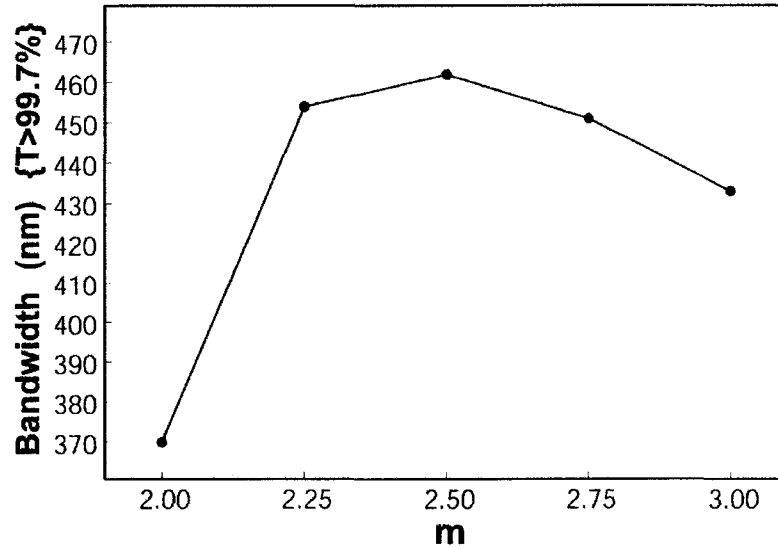


Figure 5.8 – Bandwidth results as a function of the index profile, m . Because of the high transmission values obtained, the bandwidth has been defined by wavelengths with transmission greater than 99.7%.

5.4.2 Wavelength properties of GRIN GLAD films

The wavelength response of AR films is often of critical importance to their design as the coatings are frequently applied for specific windows of the spectrum. We thus define λ_{peak} , the peak wavelength, as the wavelength of maximum transmission and hence minimum reflection and scattering. As can be seen in the plots of Figure 5.9, the dependence of λ_{peak} on the profile structure parameter, m , is decreasing with increasing m and when compared to the average index of the layers there is a correlation between the two results. The average index of an AR layer is calculated by integrating the optical path length through the porous films and dividing by the film thickness,

$$n_{\text{average}} = \frac{1}{z_0} \int_0^{z_0} n(z) dz \quad (5.17)$$

where $n(z)$ is obtained from MG effective medium theory. For films of constant thickness, $z_0=295$ nm, a smaller value for m corresponds to a greater optical thickness and

a larger n_{average} . The correlation between λ_{peak} and n_{average} indicates the interconnection of these two values and in particular shows that the wavelength response can be defined in terms of the optical thickness of the coating.

For films fabricated with the optimal profile, $m=2.5$, the physical thickness provides another means of tailoring the wavelength response of the AR film and is a direct consequence of the relationship determined above. By increasing the physical thickness, z_0 , of the GRIN GLAD film, the value of λ_{peak} increases in a uniform manner as shown in the graph of Figure 5.10. To compare these values to those of other porous AR coatings, results of calculations performed for similar “moth-eye” AR structures have shown that reflection is predicted to fall to a minimum for values of $\lambda_{\text{peak}} \approx 2.5z_0$ [147, 153]. Linear regression analysis done on the data of Figure 5.10 has resulted in a value for the slope of 2.35, only 6% from the theoretical value for structures prepared by a variety of other means. The results obtained show little deviation from the predicted linear relationship, indicating that the result is an accurate means of forecasting the wavelength response of GRIN GLAD films. The non-zero intercept obtained from GRIN GLAD films is a result of the shift of λ_{peak} toward the red part of the spectrum and is due to the effects of Rayleigh scattering on shorter wavelengths.

By controlling the optical thickness of the film through the average index of refraction and the actual physical thickness, the portion of the spectrum that provides optimal transmission for the AR coating can be predicted and the coating designed appropriately.

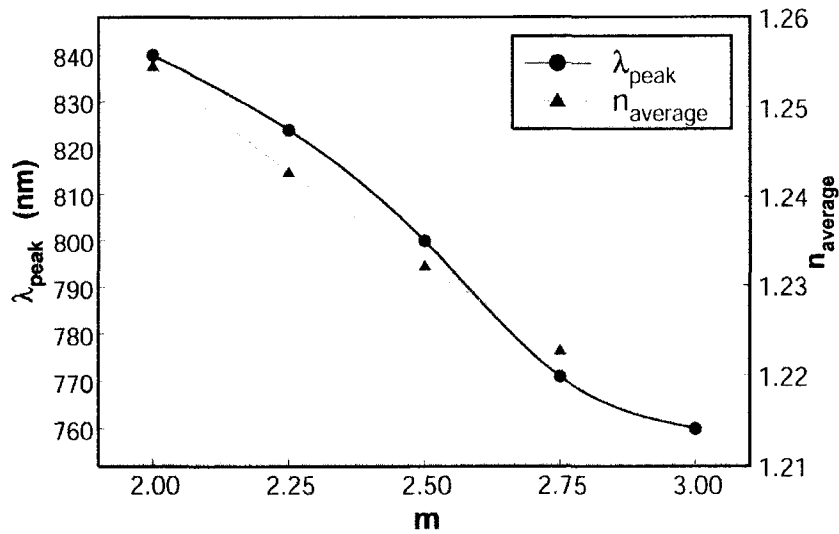


Figure 5.9 – Wavelength of peak transmission as a function of the index profile variable, m , for films with constant thickness, $z_0=295$ nm. Also included is the calculation of the average index for the different profiles showing a correlation between the optical thickness and λ_{peak} .

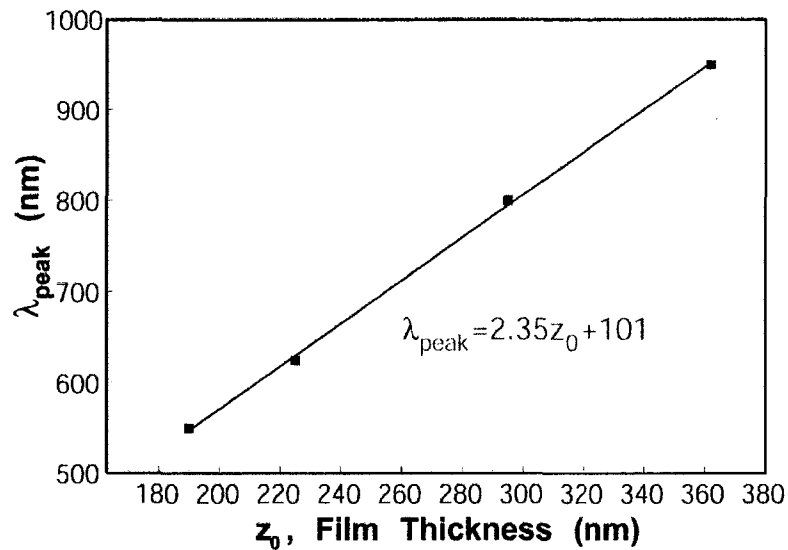


Figure 5.10 – Wavelength of peak transmission as a function of film thickness, z_0 , for films fabricated with $m=2.5$. The linear relationship is predicted from theory and agrees with accepted values [153].

5.4.3 AR properties at non-normal incidence

Due to the reduction of discontinuities in the index of refraction for GLAD films rather than the use of specific phase relations of interference coatings in providing a reduction in backscattered waves, GRIN GLAD porous AR coatings should outperform their counterparts at non-normal angles of incidence. As the angle of incidence of the incoming wavefront becomes more oblique with respect to the substrate surface, the effective thickness of the coating is increased. This increase is due to the longer distance through which the beam must pass to reach the substrate interface, it subsequently alters the phase relationship between incoming and reflected waves and, for interference coatings, the antireflective properties are highly dependent on the angle of incidence. For electromagnetic waves travelling through GRIN GLAD AR films, the phase relationship is not critically important and thus both polarizations exhibit high transmission at non-normal angles of incidence.

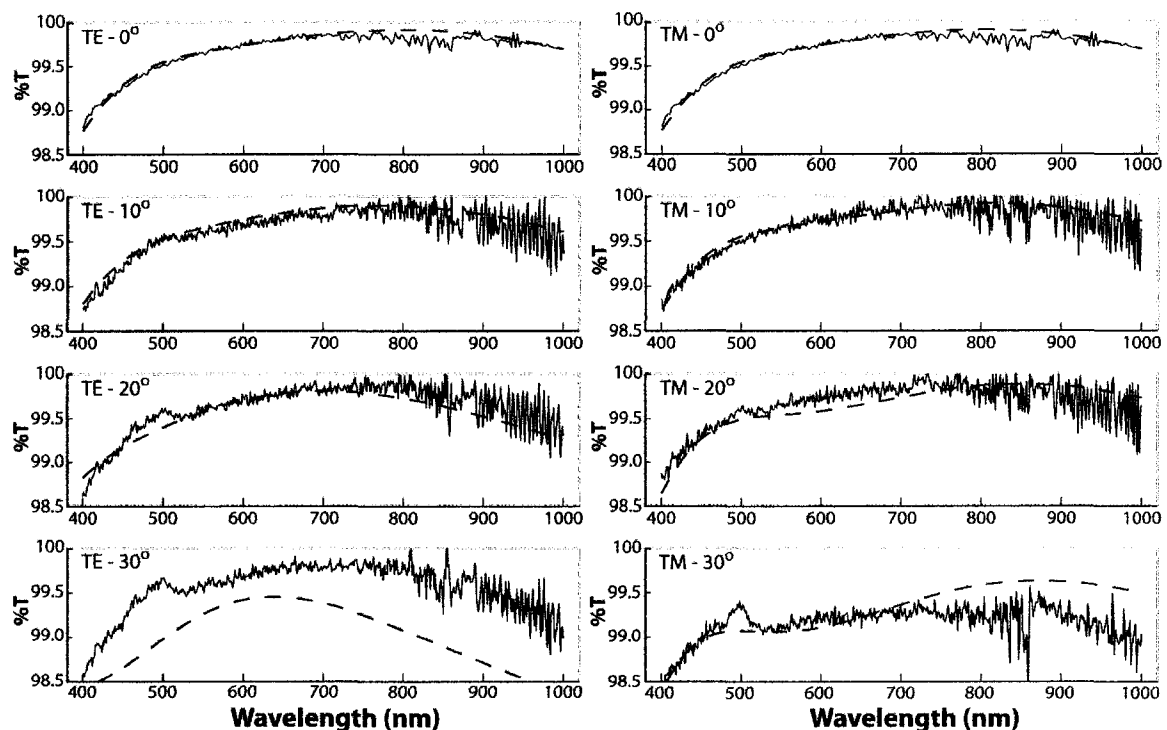


Figure 5.11 – Transmission spectra of both TE and TM polarizations for angles of incidence from 0 to 30°. The dashed curves are theoretical results of the MG derived models and the solid curve, experimental results. Note the high transmission across the spectrum characteristic of graded index coatings for non-normal angles of incidence, a result not possible with most interference AR coatings.

Transmission measurements were conducted at angles of incidence of up to 30° for both transverse electric (TE) and transverse magnetic (TM) polarizations. The polarization modes are named with respect to the plane of incidence containing both the incoming beam and the surface normal. Shown in Figure 5.11 are transmission measurements performed on a GRIN GLAD film for both normal and non-zero angles of incidence. The film can be seen to provide excellent broad angle, broadband transmission with little loss from reflection when compared to interference coatings [167]. The model used is accurate for all measured angles of TM polarization. For TE polarization some divergence in the results from the theory occurs only for data taken at 30° . This disagreement was consistent for all films and was most likely due to surface roughness not taken into account by the model. The projection of the microscopic roughness into the oblique TE plane may provide a more gradual interface, compensating for the typical effects on the effective index difference at an interface for non-normal incidence and results in a corresponding increase in transmission. For the TM polarization, the model fit is much more consistent as this polarization should not be affected to the same degree by surface roughness. Overall, the films exhibit excellent response to a broad angle of incidence for all visible wavelengths.

5.5 Conclusions

It has been found that through the fabrication of gaussian profile GRIN GLAD coatings it is possible to provide high quality AR surface treatments that allow for a wide range of wavelength tuning along with substantial bandwidth improvement over common multi-layer interference coatings. The GRIN GLAD films exhibit extremely low reflectance, with measured transmission values corresponding to significantly less than the 0.3% reflectance reported for similar layers fabricated using alternate methods [153]. These coatings are easily deposited on any flat surface and as virtually any material can be evaporated by a similar principle to that used to fabricate SiO_2 AR films, this process can be implemented in a wide variety of applications.

SiO₂ films deposited with a gaussian profile index of refraction on glass showed favourable optical responses. Profiles that were closer to the accepted ideal 5th order polynomial function showed superior performance and had peak transmittances of greater than 99.9%. The suppression of reflection was also maintained at non-normal angles of incidence for both TE and TM polarizations.

One major downfall of porous GRIN GLAD coatings is their durability. As the structures of the films are delicate and scraping the substrate often breaks off the projections that are critical to the performance of these coatings, they must be used in a controlled environment. Another factor that must be acknowledged in the use of such devices is the wavelength range under investigation as scattering from surface irregularities and finite sized nanostructures in the blue part of the visible spectrum results in a notable loss and reduced overall transmission.

6 Chapter 6

Summary and Conclusions

6.1 Optical GLAD nanostructures

This thesis presents several photonics applications of nanostructured thin films fabricated by the GLAD technique. In particular, the union of GLAD thin film morphologies with applications in photonics is natural due to the size scale of the thin film structures that lie in the range of wavelengths corresponding to optical frequencies of electromagnetic radiation. The interaction of incident radiation with the uniquely shaped film structures provides the opportunity to actively design GLAD films and tailor the response for a variety of applications. As the GLAD process is highly flexible, it is possible to use the properties of oblique deposition and substrate motion along with other deposition parameters to fine-tune the optical response of the devices. Three principle areas of application were investigated, three-dimensional photonic band gap crystals, chiral thin film/liquid crystal hybrid devices, and broadband porous antireflection coatings, and for each type of structure favourable results were obtained.

6.1.1 Square spiral photonic band gap crystals

The forbidden propagation of certain frequency bands in periodic dielectric crystals has many potential uses and by implementing customized motion control with the GLAD technique a full, three-dimensional band gap crystal was fabricated. Unlike traditional PC fabrication methods, GLAD deposition of tetragonal square spiral crystals does not require complex processes such as lithography, alignment, or etching. Once a substrate is obtained with the appropriate pre-patterned square topography and lattice period a , an entire photonic crystal with specified dimensions can be fabricated in a virtual single step deposition process.

Square spiral structures, when arranged in a regular tetragonal array, emulate the optimal diamond lattice by having each spiral elbow coincide with the approximate location of the diamond lattice sites. Given an ideally fabricated, infinite crystal with

uniform silicon spirals, a relative band gap of up to 16% can be achieved for the direct crystal structure. For a fabricated crystal, reflection measurements indicate a full three-dimensional band gap of 10%, and although less than the value predicted from theory, this value is still large when compared with many other accepted structures that employ more complex fabrication methods. The reduction in the PBG width for the fabricated structures was found to be due to variations in the spiral shapes that arose from non-uniformities of the deposition process. Variations in the fill factor of up to 10% were found to accurately predict the intersection of isolated band gaps throughout the crystal and were confirmed by variations in the measured band gap centre frequency of isolated points along the crystal edge. The overlapping of local band edges due to the reduction of crystal symmetry indicates that there might exist localized modes within the crystal rather than being completely devoid of radiation for frequencies corresponding to the band gap.

In fabricating the direct silicon tetragonal square spiral crystals, it was found that the subsequent deposition of inclined columns at right angles to the previous growth was not sufficient to produce a satisfactory structure. Advanced substrate motion was used to confine growth via imposed self-shadowing in several techniques that were developed to enhance the spirals. The 'slow corner' method produced the most favourable and symmetric crystals and as the natural density of one third for the silicon films grown at approximately 85° was close to the ideal value, this method was used to fabricate the first successful three-dimensional PBG square spiral crystal.

The optical response of PCs is governed by Maxwell's equations and as they are linear and have no dependence on dimensions, the PBGs can be scaled to virtually any wavelength regime. The crystals highlighted in this thesis were fabricated with periods corresponding to band gaps in the infrared, yet it should be possible to scale the structures and produce band gaps in the visible or communications spectrum near $1.55 \mu\text{m}$. Currently, continuing work is being done by colleague Martin O. Jensen in an attempt to scale down the crystals to this regime with success demonstrated when using electron beam lithography for substrate patterning. It was shown that by subtly changing the spiral shape through control offered by the deposition parameters, it is possible to shift

the band gap centre frequency. By scaling the substrate lattice period and accurately controlling the deposited spiral film, the optical response can be tuned to suit the desired application.

The materials properties of the spiral films were also investigated and it was found that for the deposited silicon direct structure, the films were amorphous. Annealing was investigated for SiO₂ films as a remedy for the lack of regular atomic arrangement in other materials and it was also observed that by allowing subtle reflow of the film material at high temperatures some of the non-uniformities of the crystal could be removed.

6.1.2 Chiral thin film/liquid crystal hybrids

The natural anisotropy of chiral thin films provides a circularly birefringent and optically active medium with which the polarization of incident light can be modified. To enhance the properties of the porous films, NLCs can be added whereby the chiral nanostructure of the film provides a backbone for alignment of the NLC molecules. Using this technique, rotatory powers of up to 2.3°/μm have been obtained for dielectric films filled with NLCs.

Using the variable porosity and helical dimensions of chiral films allowed by GLAD deposition, the effects of film structure on the chiral optical response were examined. It was found that when deposited at 85°, the resulting films had the optimal nanostructure for NLC alignment while maintaining a large porosity for infiltration by NLCs. The helical pitch, which can be varied across a large range of values through the rotation rate of the substrate during deposition, serves to tune the wavelength properties of the device. The greatest circular birefringence was found for Al₂O₃ films, and was due to the higher index of refraction of this material.

Upon addition of liquid crystals to the chiral films, enhancement of the optical properties of the device was seen, however it was also accompanied by a reversal in rotation direction for Al₂O₃ and MgF₂ films. It has been postulated that films fabricated from these materials have structure that is conducive to alignment of the NLC molecules opposite the handedness of the film, although the exact alignment mechanism has not

been determined. In addition to the direction reversal, the wavelength properties of all films with added NLCs were shifted towards the blue portion of the spectrum. The addition of a higher index material to the film structure is expected to yield a shift in the opposite direction, and further investigation is required to determine the origin of this behaviour. Colleague Andy van Popta is currently continuing research in this field, principally investigating the effects of film materials with higher indices of refraction such as TiO₂ in addition to the effect of NLCs on optical response and their interaction with porous films.

6.1.3 Porous broadband GRIN GLAD antireflection coatings

Recognising the potential of traditional highly porous GLAD thin films along with the versatility and control that this deposition technique offers over nanostructure fabrication, porous broadband antireflection coatings with extremely high transmission were engineered. By grading the density of the films through the angle of flux incidence, films were fabricated with gaussian density profiles that avoided significant discontinuities in the index of refraction across the coating layer. The creation of a graded index avoids the problems typically associated with common interference coatings of limited bandwidth and reduced performance at oblique incidence. In addition, a single GRIN GLAD coating was shown to substantially outperform a standard MgF₂ interference coating on glass.

To accurately predict the response of GRIN GLAD films, a model was developed that reduced the complex geometries of the GLAD nanostructures to a series of individual, uniform layers. Using effective medium theory based on the Maxwell-Garnett model, the variable density of the SiO₂ films was converted into layers with effective indices of refraction. By dividing the coatings with thicknesses of a few hundred nanometres into more than 30 sub-layers, highly accurate predictions of transmission results were obtained. The microscopic roughness of the thin film structures were prone to scattering at shorter wavelengths and to correct the model for this discrepancy it was necessary to include an empirical λ^{-4} Rayleigh factor in the calculated transmission spectra.

A control routine was developed to create an array of cone-like or ‘moth-eye’ projections across the surface of the substrate. In accurately depositing the structure with the desired density profile, a correction factor for oblique growth was included in the non-linear expression for density as a function of incidence angle. Also, as both the deposition and index profile derivation were not material specific, this technique can be used without modification for a wide range of materials including higher index semiconductors such as silicon.

The GRIN GLAD films demonstrated extremely high transmission for SiO₂ deposited on 7059 glass. Peak transmission of greater than 99.9% was obtained for an optimized film and less than 0.3% reflection loss was seen across a bandwidth of greater than 460 nm. In addition to the favourable optical response of the films, the peak transmission wavelength was easily tuned by adjusting the film thickness. Transmission at oblique incidence was also investigated for both polarization modes and it was found that the performance degraded little over a range of 30°.

6.2 Recommendations

As the research presented in this thesis represents some of the initial investigation of these applications, many ideas and recommendations for future research directions have resulted. These recommendations are aimed at both improving the optical performance of the devices and gaining greater insight into the fabrication of nanostructures by GLAD deposition.

Just as intrinsic semiconductors have limited usefulness without the addition of impurities to create defect states within the electronic band gap, PCs cannot be implemented in devices without the introduction of flaws or crystal defects. Line defects or optical microcircuitry embedded in a three-dimensional PBG crystal can be extremely useful when their dimensions are chosen to correspond to propagating modes that lie in the forbidden gap of the surrounding medium. Due the lack of propagating states outside the defect, light can be channelled along the defect with very little loss. Now that a full, three-dimensional band gap has been established for GLAD square spiral PCs, the next step in the development of this technology is to characterize defects than can be readily

fabricated using the GLAD technique. The omission of lines of seeds on the substrate, or the alteration of a single spiral turn during the growth of the PC can easily provide planar defects that can serve as slab waveguides. The omission of a single spiral can also create a line defect through the thickness of the crystal, although both this procedure and the elimination of multiple seeds must be more thoroughly investigated to determine the effect of seed pattern modification on the growth of adjacent spiral structures. Ongoing research in this area is currently being performed by colleague Martin O. Jensen.

Another PBG structure based on GLAD that must be examined is the inverse square spiral PC. The development of these periodic dielectrics that are predicted to exhibit even larger relative band gaps requires a departure from the single step deposition process of the direct structure, however, when compared to other PC fabrication methods, the number of steps and requirements of precision are still minimal. It is suggested that to fabricate the inverse structure, SiO₂ spirals be first deposited followed by either annealing, or possibly plasma enhanced CVD of SiO₂ to broaden the nanostructures. LPCVD of silicon must then be performed followed by the selective etching of the original template. By developing the inverse square spiral structure it is likely that integration of photonic devices will be facilitated, and research in this area is currently being investigated by Mark Summers.

The PC structures fabricated in this thesis had dimensions that corresponded to band gaps in the infrared. As the potential use of PBG devices lies in the fields of photonics and optical communications whose wavelengths are centred in the near infrared, an attempt should be made at reducing the size of the spirals. Scaling should be possible using the GLAD technique as typical dimensions of structures are on the order of a hundred nanometres, and through the use of techniques such as electron beam lithography, pre-patterned wafers with the appropriate lattice dimensions should be easily obtained. One difficulty with this process that must be overcome is the material requirement for large index materials that are lossless in the shorter wavelength regions of the spectrum. Although GLAD offers the ability to deposit a wide variety of materials, and as it is necessary for the formation of large band gaps to have large index contrasts, in particular the minimum requirement for a nearest-neighbour connection crystal of 2.15

[8], it is possible that special techniques must be adopted to provide the required high index contrast for wavelengths in the visible spectrum.

The unpredicted results of negative optical activity and the blue shift of the optical response upon the addition of NLCs to chiral thin films require a great deal more investigation to fully understand the interaction of LCs with GLAD films. Although a potential mechanism has been proposed that might account for negative optical activity in certain films, chiral thin film/LC hybrids must be more thoroughly examined in particular with respect to material and wavelength properties. Through better understanding of the performance of these devices, applications to flat panel display technologies should be possible.

Due to the simplicity of GRIN GLAD antireflection coatings and the versatility of the fabrication process, favourable AR responses have been obtained that can be fine-tuned to the desired spectrum. Although scattering reduces the efficiency of the coatings at shorter wavelengths, for the visible spectrum these AR layers are extremely effective. For commercial implementation of these coatings it would be highly desirable to be able to deposit GRIN GLAD on curved surfaces such as lens faces, so that they can be used wherever more traditional interference coatings are found. Such a development would require intensive study because of the complex geometries imposed by a non-planar surface, however as the deposition process is quite versatile with many variable parameters it can hopefully be achieved.

7 References

- [1] K. Robbie, M. J. Brett, and A. Lakhtakia, "First thin film realization of a helicoidal bianisotropic medium," *J. Vac. Sci. Technol. A*, vol. 13, pp. 2991-2993, 1995.
- [2] K. Robbie, M. J. Brett, and A. Lakhtakia, "Chiral sculptured thin films," *Nature*, vol. 384, pp. 616-616, 1996.
- [3] K. Robbie and M. J. Brett, "Sculptured thin films and glancing angle deposition: Growth mechanics and applications," *J. Vac. Sci. Technol. A*, vol. 15, pp. 1460-1465, 1997.
- [4] K. D. Harris, J. R. McBride, K. E. Nietering, and M. J. Brett, "Fabrication of porous platinum thin films for hydrocarbon sensor applications," *Sensors and Materials*, vol. 13, pp. 225-234, 2001.
- [5] K. D. Harris, A. Huizinga, and M. J. Brett, "High-speed porous thin film humidity sensors," *Electrochem. solid-state lett.*, vol. 5, pp. H27-H29, 2002.
- [6] M. W. Seto, B. Dick, and M. J. Brett, "Microsprings and microcantilevers: studies of mechanical response," *Journal micromech. microeng.*, vol. 11, pp. 582-588, 2001.
- [7] M. W. Seto, K. Robbie, D. Vick, M. J. Brett, and L. Kuhn, "Mechanical response of thin films with helical microstructures," *J. Vac. Sci. Technol. B*, vol. 17, pp. 2172-2177, 1999.
- [8] O. Toader and S. John, "Square spiral photonic crystals: A Robust architecture for microfabrication of materials with large three-dimensional photonic band gaps," *Phys. Rev. E*, vol. 66, pp. 016610, 2002.
- [9] O. Toader and S. John, "Proposed Square Spiral Microfabrication for Large Three-Dimensional Photonic Band Gap Crystals," *Science*, vol. 292, pp. 1133-1135, 2001.
- [10] M. Faraday, *Phil. Trans.*, vol. 147, pp. 145, 1857.
- [11] R. Nahrwold, *Ann. Physik*, vol. 31, pp. 467, 1887.
- [12] A. Kundt, *Ann. Physik*, vol. 34, pp. 473, 1888.
- [13] J. C. Maxwell, *A Treatise on Electricity and Magnetism*, 3rd ed. Stanford: Academic Reprints, 1891.
- [14] H. A. Macleod, *Thin-Film Optical Filters*. New York: American Elsevier, 1969.

- [15] L. I. Maissel and R. Glang, "Handbook of Thin Film Technology." New York: McGraw Hill, 1970.
- [16] R. F. Bunshah, "Handbook of Deposition Technologies For Films and Coatings: Science, Technology and Applications," 2nd ed. Park Ridge: Noyes Publications, 1994.
- [17] M. Ohring, *The Materials Science of Thin Films*. San Diego: Academic Press, 1992.
- [18] R. Glang, "Vacuum Evaporation," in *Handbook of Thin Film Technology*, L. I. Maissel and R. Glang, Eds. New York: McGraw Hill, 1970.
- [19] B. N. Chapman, *Glow Discharge Processes*. New York: Wiley, 1980.
- [20] E. B. Graper, "Evaporation Characteristics of Materials from an Electron-Beam Gun," *J. Vac. Sci. Technol.*, vol. 8, pp. 333-337, 1971.
- [21] E. B. Graper, "Evaporation characteristics of materials from an electron beam gun II," *J. Vac. Sci. Technol. A*, vol. 5, pp. 2718-2723, 1987.
- [22] J. C. Sit, D. Vick, K. Robbie, and M. J. Brett, "Thin film microstructure control using glancing angle deposition by sputtering," *J. mater. res.*, vol. 14, pp. 1197-1199, 1999.
- [23] J. F. O'Hanlon, *A user's guide to vacuum technology*, 2nd ed. New York: Wiley, 1989.
- [24] B. A. Movchan and A. V. Demchishin, "Study of the structure and properties of thick vacuum condensates of nickel, titanium, tungsten, aluminum oxide and zirconium dioxide," *Phys. Met. Metallog.*, vol. 28(II), pp. 83-90, 1969.
- [25] J. A. Thornton, "High Rate Thick Film Growth," *Ann. Rev. Mater. Sci.*, vol. 7, pp. 239-260, 1977.
- [26] R. Messier, A. P. Giri, and R. A. Roy, "Revised structure zone model for thin film physical structure," *J. Vac. Sci. Technol. A*, vol. 2, pp. 500-503, 1984.
- [27] R. Messier, "Toward quantification of thin film morphology," *J. Vac. Sci. Technol. A*, vol. 4, pp. 490-495, 1986.
- [28] T. G. Knorr and R. W. Hoffman, "Dependence of Geometric Magnetic Anisotropy in Thin Iron Films," *Phys. Rev. B*, vol. 113, pp. 1039-1046, 1959.
- [29] D. O. Smith, "Anisotropy in Permalloy Films," *J. Appl. Phys.*, vol. 30, pp. 264S-265S, 1959.

- [30] D. O. Smith, M. S. Cohen, and G. P. Weiss, "Oblique-Incidence Anisotropy in Evaporated Permalloy Films," *J. Appl. Phys.*, vol. 31, pp. 1755-1762, 1960.
- [31] N. O. Young and J. Kowal, "Optically Active Fluorite Films," *Nature*, vol. 183, pp. 104-105, 1959.
- [32] I. J. Hodgkinson, F. Horowitz, H. A. Macleod, M. Sikkens, and J. J. Wharton, "Measurement of the principal refractive indices of thin films deposited at oblique incidence," *J. Opt. Soc. Am. A*, vol. 2, pp. 1693-1697, 1985.
- [33] K. Robbie, L. J. Friedrich, S. K. Dew, T. Smy, and M. J. Brett, "Fabrication of Thin-Films with Highly Porous Microstructures," *J. Vac. Sci. Technol. A*, vol. 13, pp. 1032-1035, 1995.
- [34] K. Robbie, "Glancing angle deposition," PhD dissertation, University of Alberta, Dept. of Electrical and Computer Engineering, 1998.
- [35] K. Robbie, J. C. Sit, and M. J. Brett, "Advanced techniques for glancing angle deposition," *J. Vac. Sci. Technol. B*, vol. 16, pp. 1115-1122, 1998.
- [36] K. Robbie, C. Shafai, and M. J. Brett, "Thin films with nanometer-scale pillar microstructure," *J. mater. res.*, vol. 14, pp. 3158-3163, 1999.
- [37] K. Robbie and M. J. Brett, "Method of depositing shadow sculpted thin films", *US Patent No. 5,866,204*, 1999.
- [38] T. Motohiro and Y. Taga, "Thin film retardation plate by oblique deposition," *Appl. Opt.*, vol. 28, pp. 2466-2482, 1989.
- [39] I. J. Hodgkinson, S. J. Cloughley, Q. H. Wu, and S. Kassam, "Anisotropic scatter patterns and anomalous birefringence of obliquely deposited cerium oxide films," *Appl. Opt.*, vol. 35, pp. 5563-5568, 1996.
- [40] R. Messier, T. Gehrke, C. Frankel, V. C. Venugopal, W. Otano, and A. Lakhtakia, "Engineered sculptured nematic thin films," *J. Vac. Sci. Technol. A*, vol. 15, pp. 2148-2152, 1997.
- [41] L. Abelmann and C. Lodder, "Oblique evaporation and surface diffusion," *Thin Solid Films*, vol. 305, pp. 1-21, 1997.
- [42] I. Hodgkinson and Q. Wu, "Serial bideposition of anisotropic thin films with enhanced linear birefringence," *Appl. Opt.*, vol. 38, pp. 3621-3625, 1999.
- [43] J. M. Nieuwenhuizen and H. B. Haanstra, "Microfractography of thin films," *Philips Tech. Rev.*, vol. 27, pp. 87-91, 1966.
- [44] A. G. Dirks and H. J. Leamy, "Columnar Microstructure in Vapor-Deposited Thin Films," *Thin Solid Films*, vol. 47, pp. 219-233, 1977.

- [45] S. Lichter and J. Chen, "Model for Columnar Microstructure of Thin Solid Films," *Phys. Rev. Lett.*, vol. 56, pp. 1396-1399, 1986.
- [46] I. Hodgkinson, Q. Wu, and A. McPhun, "Incremental-growth model for the deposition of spatially modulated thin film nanostructures," *J. Vac. Sci. Technol. B*, vol. 16, pp. 2811-2816, 1998.
- [47] R. N. Tait, T. Smy, and M. J. Brett, "Modeling and Characterization of Columnar Growth in Evaporated-Films," *Thin Solid Films*, vol. 226, pp. 196-201, 1993.
- [48] J. C. Sit, "Thin film / liquid crystal composite optical materials and devices," PhD dissertation, University of Alberta, Dept. of Electrical and Computer Engineering, 2002.
- [49] K. Robbie, A. J. P. Hnatiw, M. J. Brett, R. I. MacDonald, and J. N. McMullin, "Inhomogeneous thin film optical filters fabricated using glancing angle deposition," *Electron. Lett.*, vol. 33, pp. 1213-1214, 1997.
- [50] J. C. Sit, D. J. Broer, and M. J. Brett, "Liquid Crystal Alignment and Switching in Porous Chiral Thin Films," *Adv. Mater.*, vol. 12, pp. 371-373, 2000.
- [51] S. R. Kennedy, J. C. Sit, D. J. Broer, and M. J. Brett, "Optical activity of chiral thin film and liquid crystal hybrids," *Liquid Crystals*, vol. 28, pp. 1799-1803, 2001.
- [52] S. R. Kennedy, M. J. Brett, O. Toader, and S. John, "Fabrication of Tetragonal Square Spiral Photonic Crystals," *Nano Lett.*, vol. 2, pp. 59-62, 2002.
- [53] S. R. Kennedy, M. J. Brett, H. Miguez, O. Toader, and S. John, "Optical Properties of a Three-Dimensional Silicon Square Spiral Photonic Crystal," *Photonics and Nanostructures*, vol. www.elsevierphysics.com/physics.html, in press 2003.
- [54] S. R. Kennedy and M. J. Brett, "Porous Broadband Antireflection Coatings by Glancing Angle Deposition," *Appl. Opt.*, vol. 42, pp. 4573-4579, 2003.
- [55] A. T. Wu, M. Seto, and M. J. Brett, "Capacitive SiO humidity sensors with novel microstructures," *Sensors and Materials*, vol. 11, pp. 493-505, 1999.
- [56] A. T. Wu and M. J. Brett, "Sensing humidity using nanostructured SiO posts: Mechanism and optimization," *Sensors and Materials*, vol. 13, pp. 399-431, 2001.
- [57] K. D. Harris, D. Vick, E. J. Gonzalez, T. Smy, K. Robbie, and M. J. Brett, "Porous thin films for thermal barrier coatings," *Surf. coat. technol.*, vol. 138, pp. 185-191, 2001.

- [58] J. N. Broughton and M. J. Brett, "Electrochemical capacitance in manganese thin films with chevron microstructure," *Electrochem. solid-state lett.*, vol. 5, pp. A279-A282, 2002.
- [59] B. Dick, M. J. Brett, T. J. Smy, M. R. Freeman, M. Malac, and R. F. Egerton, "Periodic magnetic microstructures by glancing angle deposition," *J. Vac. Sci. Technol. A*, vol. 18, pp. 1838-1844, 2000.
- [60] M. J. Colgan and M. J. Brett, "Field emission from carbon and silicon films with pillar microstructure," *Thin Solid Films*, vol. 389, pp. 1-4, 2001.
- [61] P. C. P. Hruday, M. Taschuk, Y. Y. Tsui, R. Fedosejevs, J. C. Sit, and M. J. Brett, "Evaporated nanostructured $Y_2O_3:Eu$ thin films," presented at International Conference on MEMS, NANO and Smart Systems 2003, Banff, Alberta, Canada, 2003.
- [62] K. D. Harris, K. L. Westra, and M. J. Brett, "Fabrication of perforated thin films with helical and chevron pore shapes," *Electrochem. solid-state lett.*, vol. 4, pp. C39-C42, 2001.
- [63] K. D. Harris, J. C. Sit, and M. J. Brett, "Fabrication and optical characterization of template-constructed thin films with chiral nanostructure," *IEEE trans. nanotech.*, vol. 1, pp. 122-128, 2002.
- [64] W. L. Bragg, "The Structure of Some Crystals as Indicated by their Diffraction of X-rays," *Proc. R. Soc. Lond. A*, vol. 89, pp. 248-277, 1913.
- [65] L. Brillouin, *Wave Propagation in Periodic Structures*, 2nd ed. New York: Dover Publications Inc., 1953.
- [66] P. W. Anderson, "Absence of Diffusion in Certain Random Lattices," *Phys. Rev.*, vol. 109, pp. 1492-1505, 1958.
- [67] S. John, "Electromagnetic Absorption in a Disordered Medium near a Photon Mobility Edge," *Phys. Rev. Lett.*, vol. 53, pp. 2169-2172, 1984.
- [68] S. John, "Strong Localization of Photons in Certain Disordered Dielectric Superlattices," *Phys. Rev. Lett.*, vol. 58, pp. 2486-2489, 1987.
- [69] E. Yablonovitch, "Inhibited Spontaneous Emission in Solid-State Physics and Electronics," *Phys. Rev. Lett.*, vol. 58, pp. 2059-2062, 1987.
- [70] J. D. Joannopoulos, P. R. Villeneuve, and S. Fan, "Photonic crystals: putting a new twist on light," *Nature*, vol. 386, pp. 143-149, 1997.
- [71] E. Yablonovitch, "Photonic band-gap structures," *J. Opt. Soc. Am. B*, vol. 10, pp. 283-295, 1993.

- [72] S. John and M. Florescu, "Photonic bandgap materials: Towards an all-optical micro-transistor," *J. Opt. A*, vol. 3, pp. S103-S120, 2001.
- [73] K. M. Ho, C. T. Chan, and C. M. Soukoulis, "Existence of a Photonic Gap in Periodic Dielectric Structures," *Phys. Rev. Lett.*, vol. 65, pp. 3152-3155, 1990.
- [74] S. Satpathy, Z. Zhang, and M. R. Salehpour, "Theory of Photon Bands in Three-Dimensional Periodic Structures," *Phys. Rev. Lett.*, vol. 64, pp. 1239-1242, 1990.
- [75] Z. Zhang and S. Satpathy, "Electromagnetic Wave Propagation in Periodic Structures: Bloch Wave Solution of Maxwell's Equation," *Phys. Rev. Lett.*, vol. 65, pp. 2650-2653, 1990.
- [76] R. D. Meade, K. D. Brommer, A. M. Rappe, and J. D. Joannopoulos, "Photonic bound states in periodic dielectric materials," *Phys. Rev. B*, vol. 44, pp. 13772-13774, 1991.
- [77] R. D. Meade, A. M. Rappe, K. D. Brommer, J. D. Joannopoulos, and O. L. Alerhand, "Accurate theoretical analysis of photonic band-gap materials," *Phys. Rev. B*, vol. 48, pp. 8434-8437, 1993.
- [78] J. D. Joannopoulos, R. D. Meade, and J. N. Winn, *Photonic Crystals: molding the flow of light*. Princeton: Princeton University Press, 1995.
- [79] A. Taflove, *Computational electrodynamics: the finite-difference time-domain method*, 2nd ed. Boston: Artech House, 2000.
- [80] F. Herman, "The Electronic Energy Band Structure of Silicon and Germanium," *Proc. IRE*, vol. 43, pp. 1703-1732, 1955.
- [81] E. Yablonovitch, T. J. Gmitter, and K. M. Leung, "Photonic Band Structure: The Face-Centered-Cubic Case Employing Nonspherical Atoms," *Phys. Rev. Lett.*, vol. 67, pp. 2295-2298, 1991.
- [82] C. T. Chan, S. Datta, K. M. Ho, and C. M. Soukoulis, "A7 structure: A family of photonic crystals," *Phys. Rev. B*, vol. 50, pp. 1988-1991, 1994.
- [83] C. C. Cheng and A. Scherer, "Fabrication of photonic band-gap crystals," *J. Vac. Sci. Technol. B*, vol. 13, pp. 2696-2700, 1995.
- [84] C. C. Cheng, A. Scherer, V. Arbet-Engels, and E. Yablonovitch, "Lithographic band gap tunig in phonic band gap crystals," *J. Vac. Sci. Technol. B*, vol. 14, pp. 4110-4114, 1996.
- [85] K. M. Ho, C. T. Chan, C. M. Soukoulis, R. Biswas, and M. Sigalas, "Photonic band gaps in three dimensions: new layer-by-layer periodic structures," *Solid State Commun.*, vol. 89, pp. 413-416, 1994.

- [86] E. Ozbay, "Layer-by-layer photonic crystals from microwave to far-infrared frequencies," *J. Opt. Soc. Am. B*, vol. 13, pp. 1945-1955, 1996.
- [87] S. Noda, K. Tomoda, N. Yamamoto, and A. Chutinan, "Full Three-Dimensional Photonic Bandgap Crystals at Near-Infrared Wavelengths," *Science*, vol. 289, pp. 604-606, 2000.
- [88] K. Busch and S. John, "Photonic band gap formation in certain self-organizing systems," *Phys. Rev. E*, vol. 58, pp. 3896-3908, 1998.
- [89] H. Miguez, F. Meseguer, C. Lopez, A. Blanco, J. S. Moya, J. Requena, A. Mifsud, and V. Fornes, "Control of the Photonic Crystal Properties of fcc-Packed Submicrometer SiO₂ Spheres by Sintering," *Adv. Mater.*, vol. 10, pp. 480-483, 1998.
- [90] A. Blanco, E. Chomski, S. Grachtchak, M. Ibsate, S. John, S. W. Leonard, C. Lopez, F. Meseguer, H. Miguez, J. P. Mondia, G. A. Ozin, O. Toader, and H. M. van Driel, "Large-scale synthesis of a silicon photonic crystal with a complete three-dimensional band gap near 1.5 micrometres," *Nature*, vol. 405, pp. 437-440, 2000.
- [91] Y. A. Vlasov, X. Z. Bo, J. C. Sturm, and D. J. Norris, "On-chip natural assembly of silicon photonic bandgap crystals," *Nature*, vol. 414, pp. 289-293, 2001.
- [92] A. Chutinan and S. Noda, "Spiral three-dimensional photonic-band-gap structure," *Phys. Rev. B*, vol. 57, pp. R2006-R2008, 1998.
- [93] M. Malac, R. F. Egerton, M. J. Brett, and B. Dick, "Fabrication of submicrometer regular arrays of pillars and helices," *J. Vac. Sci. Technol. B*, vol. 17, pp. 2671-2674, 1999.
- [94] B. Dick, J. C. Sit, M. J. Brett, I. M. N. Votte, and C. W. M. Bastiaansen, "Embossed polymeric relief structures as a template for the growth of periodic inorganic microstructures," *Nano Lett.*, vol. 1, pp. 71-73, 2001.
- [95] B. Dick, M. J. Brett, and T. Smy, "Controlled growth of periodic pillars by glancing angle deposition," *J. Vac. Sci. Technol. B*, vol. 21, pp. 23-28, 2003.
- [96] N. N. Efremow, N. P. Economou, K. Bezjian, S. S. Dana, and H. I. Smith, "A simple technique for modifying the profile of resist exposed by holographic lithography," *J. Vac. Sci. Technol.*, vol. 19, pp. 1234-1237, 1981.
- [97] B. A. Dick, "Properties and Growth of Thin Films Produced by Glancing Angle Deposition," PhD dissertation, University of Alberta, Dept. of Electrical and Computer Engineering, 2003.

- [98] S. Y. Lin, J. G. Fleming, D. L. Hetherington, B. K. Smith, R. Biswas, K. M. Ho, M. Sigalas, W. Zubrzycki, S. R. Kurtz, and J. Bur, "A three-dimensional photonic crystal operating at infrared wavelengths," *Nature*, vol. 394, pp. 251-253, 1998.
- [99] A. Chutinan, S. John, and O. Toader, "Diffractionless Flow of Light in All-Optical Microchips," *Phys. Rev. Lett.*, vol. 90, pp. 123901, 2003.
- [100] S. R. Kennedy and M. J. Brett, "Advanced Techniques for the Fabrication of Square Spiral Photonic Crystals by Glancing Angle Deposition," *submitted to J. Vac. Sci. Technol. B*, 2003.
- [101] E. C. Freeman and W. Paul, "Optical constants of rf sputtered hydrogenated amorphous Si," *Phys. Rev. B*, vol. 20, pp. 716-728, 1979.
- [102] H. Piller, "Silicon (Amorphous)," in *Handbook of Optical Constants of Solids*, E. D. Palik, Ed. London: Academic Press, Inc., 1985, pp. 571-586.
- [103] E. Bauer, "Growth of Oriented Films on Amorphous Surfaces," in *Single Crystal Films*, M. H. Francombe and H. Sato, Eds. Oxford: Pergamon, 1964.
- [104] B. Dick, M. J. Brett, and T. Smy, "Effect of Substrate Rotation on the Growth of Microstructures at Glancing Incidence," *submitted to J. Vac. Sci. Technol. B*, 2003.
- [105] R. Jacobsson, "Inhomogeneous and Coevaporated Homogeneous Films for Optical Applications," in *Phys. Thin Films*, vol. 8, G. Hass, M. Francombe, and R. Hoffman, Eds., 1975, pp. 51-98.
- [106] R. Landauer, "Electrical Conductivity in Inhomogeneous Media," in *Proceedings of the First Congress on the Electrical Transport and Optical Properties of Inhomogeneous Media*, vol. 40, J. C. Garland and D. B. Tanner, Eds. New York: AIP, pp. 2-43, 1978.
- [107] O. Dag, G. A. Ozin, H. Yang, C. Reber, and G. Bussiere, "Photoluminescent Silicon Clusters in Oriented Hexagonal Mesoporous Silica Film," *Adv. Mater.*, vol. 11, pp. 474-480, 1999.
- [108] M. J. Cooke, "A review of LPCVD metallization for semiconductor devices," *Vacuum*, vol. 35, pp. 67-73, 1985.
- [109] M. J. Colgan, B. Djurfors, D. G. Ivey, and M. J. Brett, "Effects of Annealing on Titanium Dioxide Structured Films," *submitted to Thin Solid Films*, 2003.
- [110] "www.nobel.se/chemistry/laureates/2001." The Royal Swedish Academy of Sciences
- [111] L. D. Barron, *Molecular Light Scattering and Optical Activity*. New York: Cambridge University Press, 1982.

- [112] J. Kerr, "A new relation between Electricity and Light: Dielectrified Media Birefringent," *Phil. Mag.*, vol. 50, pp. 337-348, 1875.
- [113] M. Faraday, "Experimental Researches in Electricity - Nineteenth Series," *Phil. Mag.*, vol. 28, pp. 294-317, 1846.
- [114] D. F. J. Arago, *Mem. de l'Inst.*, vol. 12, pp. 93, 1811.
- [115] J. B. Biot, *Mem. de l'Inst.*, vol. 13, pp. 218, 1812.
- [116] E. Hecht, *Optics*, 2nd ed. Don Mills: Addison-Wesley Publishing Co., Inc, 1990.
- [117] M. Born and E. Wolf, *Principles of Optics*, 4th ed. New York: Pergamon Press, 1970.
- [118] A. Cotton, "Absorption inegale des rayons circulaires droit et gauche dans certains corps actifs," *C. R. Hebdo. Acad. Sci.*, vol. 120, pp. 989-991, 1895.
- [119] C. W. Oseen, "The Theory of Liquid Crystals," *Trans. Faraday Soc.*, vol. 29, pp. 883-899, 1933.
- [120] R. M. A. Azzam, "Chiral thin solid films: Method of deposition and applications," *Appl. Phys. Lett.*, vol. 61, pp. 3118-3120, 1992.
- [121] A. Lakhtakia and W. S. Weiglhofer, "On Light Propagation in Helicoidal Bianisotropic Mediums," *Proc. R. Soc. Lond. A*, vol. 448, pp. 419-437, 1995.
- [122] P. I. Rovira, R. A. Yarussi, R. W. Collins, R. Messier, V. C. Venugopal, A. Lakhtakia, K. Robbie, and M. J. Brett, "Transmission ellipsometry of a thin-film helicoidal bianisotropic medium," *Appl. Phys. Lett.*, vol. 71, pp. 1180-1182, 1997.
- [123] P. I. Rovira, R. A. Yarussi, R. W. Collins, V. C. Venugopal, A. Lakhtakia, R. Messier, K. Robbie, and M. J. Brett, "Rotating-compensator multichannel transmission ellipsometry of a thin-film helicoidal bianisotropic medium," *Thin Solid Films*, vol. 313, pp. 373-378, 1998.
- [124] I. Hodgkinson, Q. Wu, B. Knight, A. Lakhtakia, and K. Robbie, "Vacuum deposition of chiral sculptured thin films with high optical activity," *Appl. Opt.*, vol. 39, pp. 642-649, 2000.
- [125] K. Robbie, D. J. Broer, and M. J. Brett, "Chiral nematic order in liquid crystals imposed by an engineered inorganic nanostructure," *Nature*, vol. 399, pp. 764-766, 1999.
- [126] J. C. Sit, D. J. Broer, and M. J. Brett, "Alignment and switching of nematic liquid crystals embedded in porous chiral thin films," *Liquid Crystals*, vol. 27, pp. 387-391, 2000.

- [127] W. C. O'Mara, *Liquid crystal flat panel display: manufacturing science & technology*. New York: Van Nostrand Reinhold, 1993.
- [128] S. Chandrasekhar, *Liquid Crystals*, 2nd ed. Cambridge: Cambridge University Press, 1994.
- [129] H. de Vries, "Rotatory Power and Other Optical Properties of Certain Liquid Crystals," *Acta. Cryst.*, vol. 4, pp. 219-226, 1951.
- [130] S. Meiboom and M. Sammon, "Molecular Orientation of Monomolecular Liquid Crystal Layers on Various Substrated," in *The Physics and Chemistry of Liquid Crystal Devices*, G. Sprokel, Ed. New York: Plenum Press, 1980, pp. 13-21.
- [131] G. W. Gray, "Liquid Crystalline Materials for Display Devices," in *Proceedings of ERA Symposium on Liquid Crystals for Display Applications*. Brighton, pp. 61-68, 1972.
- [132] G. Friedel, "Les etats mesomorphes de la matiere," *Ann. Physique*, vol. 18(9), pp. 273-474, 1922.
- [133] A. D. Buckingham, G. P. Ceasar, and M. B. Dunn, "The Addition of Optically Active Compounds to Nematic Liquid Crystals," *Chem. Phys. Lett.*, vol. 3, pp. 540-541, 1969.
- [134] M. Schadt and W. Helfrich, "Voltage-Dependent Optical Activity of a Twisted Nematic Liquid Crystal," *Appl. Phys. Lett.*, vol. 18, pp. 127-128, 1971.
- [135] V. H. Zocher, *Naturwissenschaften*, vol. 13, pp. 1015, 1925.
- [136] J. L. Janning, "Thin films surface orientation for liquid crystals," *Appl. Phys. Lett.*, vol. 21, pp. 173-174, 1972.
- [137] W. Urbach, M. Boix, and E. Guyon, "Alignment of nematics and smectics on evaporated films," *Appl. Phys. Lett.*, vol. 25, pp. 479-481, 1974.
- [138] W. M. Gibbons, P. J. Shannon, S.-T. Sun, and B. J. Swetlin, "Surface-mediated alignment of nematic liquid crystals with polarized laser light," *Nature*, vol. 351, pp. 49-50, 1991.
- [139] I. Hodgkinson, Q. Wu, and K. M. McGrath, "Moisture adsorption effects in biaxial and chiral optical thin film coatings," vol. 3790, *Proceedings of SPIE*, A. Lakhtakia and R. F. Messier, Eds. Denver: SPIE, pp. 184-194, 1999.
- [140] A. van Popta, "Personal Communication,"
- [141] D. J. Broer, J. Lub, and G. N. Mol, "Wide-band reflective polarizers from cholesteric polymer networks with a pitch gradient," *Nature*, vol. 378, pp. 467-469, 1995.

- [142] S. R. Kennedy and M. J. Brett, "Porous Broadband Antireflection Coatings by Glancing Angle Deposition," *Appl. Opt. OT*, in press 2003.
- [143] L. Schirone, G. Sotgiu, and F. P. Califano, "Chemically etched porous silicon as an anti-reflection coating for high efficiency solar cells," *Thin Solid Films*, vol. 297, pp. 296-298, 1997.
- [144] P. Vitanov, M. Kamenova, N. Tyutyundzhiev, M. Delibasheva, E. Goranova, and M. Peneva, "High-efficiency solar cell using a thin porous silicon layer," *Thin Solid Films*, vol. 297, pp. 299-303, 1997.
- [145] W. H. Lowdermilk and D. Milam, "Graded-index antireflection surfaces for high-power laser applications," *Appl. Phys. Lett.*, vol. 36, pp. 891-893, 1980.
- [146] T. Beyer and M. Tacke, "Antireflection coatings for PbSe diode lasers," *Appl. Phys. Lett.*, vol. 73, pp. 1191-1193, 1998.
- [147] A. Gombert, W. Glaubitt, K. Rose, J. Dreibholz, C. Zanke, B. Blasi, A. Heinzl, W. Horbelt, D. Sporn, W. Doll, V. Wittwer, and J. Luther, "Glazing with very high solar transmittance," *Solar Energy*, vol. 62, pp. 177-188, 1998.
- [148] K. Hadobas, S. Kirsch, A. Carl, M. Acet, and E. F. Wasserman, "Reflection properties of nanostructure-arrayed silicon surfaces," *Nanotechnology*, vol. 11, pp. 161-164, 2000.
- [149] P. Yeh, *Optical waves in layered media*. New York: Wiley, 1988.
- [150] N. Ford and P. W. McMillan, "Integral antireflection films for glasses: a review," *Glass Technol.*, vol. 26, pp. 104-107, 1985.
- [151] J. Fraunhofer, *Gesammelte Schriften*. Munich, 1887.
- [152] C. G. Bernhard, "Structural and functional adaptation in a visual system," *Endeavour*, vol. 26, pp. 79-84, 1967.
- [153] S. J. Wilson and M. C. Hutley, "The optical properties of 'moth eye' antireflection surfaces," *Optica Acta*, vol. 29, pp. 993-1009, 1982.
- [154] W. H. Southwell, "Gradient-index antireflection coatings," *Opt. Lett.*, vol. 8, pp. 584-586, 1983.
- [155] W. H. Southwell, "Pyramid-array surface-relief structures producing antireflection index matching on optical surfaces," *J. Opt. Soc. Am. A*, vol. 8, pp. 549-553, 1991.
- [156] M. Thonissen, M. G. Berger, M. Kruger, W. Theiss, S. Hilbrich, R. Arens-Fischer, S. Billat, and H. Luth, "Improved interference filter structures made of porous silicon," *Mat. Res. Soc. Proc.*, vol. 452, pp. 643-648, 1997.

- [157] S. Uehara, K. Kurose, and T. Masubara, "Wide Bandwidth Porous Silicon Coatings for Silicon," *Phys. Stat. Sol. A*, vol. 182, pp. 461-464, 2000.
- [158] K. Kintaka, J. Nishii, A. Mizutani, H. Kikuta, and H. Nakano, "Antireflection microstructures fabricated upon fluorine-doped SiO₂ films," *Appl. Opt.*, vol. 26, pp. 1642-1644, 2001.
- [159] J. C. Maxwell-Garnett, "Colours in Metal Glasses and in Metallic Films," *Philos. Trans. R. Soc. London*, vol. 203, pp. 385-420, 1904.
- [160] J. C. Maxwell-Garnett, "Colours in Metal Glasses, in Metallic Films, and in Metallic Solutions. II," *Philos. Trans. R. Soc. London*, vol. 205, pp. 237-288, 1906.
- [161] D. A. G. Bruggeman, "Berechnung verschiedener physikalischer Konstanten von heterogenen Substanzen," *Ann. Physik*, vol. 24, pp. 636-664, 1935.
- [162] C. G. Granqvist and O. Hunderi, "Optical properties of ultrafine gold particles," *Phys. Rev. B*, vol. 16, pp. 3513-3534, 1977.
- [163] R. Clausius, "Die mechanische Behandlung der Electricitat." Braunschweig: Vieweg, 1879, pp. 62.
- [164] O. F. Mosotti, "Memorie di Matematica e di Fisica della Societa Italiana delle Scienze Residente in Modena," vol. 24, pp. 49-74, 1850.
- [165] L. Lorenz, *Weidemannsche Annalen*, vol. 11, pp. 70, 1880.
- [166] H. A. Lorentz, *The Theory of Electrons*. New York: Dover, 1952.
- [167] R. M. A. Azzam, "Single-layer antireflection coatings on absorbing substrates for the parallel and perpendicular polarizations at oblique incidence," *Appl. Opt.*, vol. 24, pp. 513-518, 1985.

A Appendix A

GLAD Nanostructure Control Routines

The many unique nanostructures characteristic of GLAD films result from careful substrate motion during the deposition. Two stepper motors that allow the motion two degrees of freedom accomplish the accurate positioning of the substrate, and by computer software control the desired motion is controlled as a function of integrated film thickness, z . In all of the following definitions, the film thickness is defined with its origin at the substrate surface and positive outward from this interface. This definition is in contrast to the definitions of z used in theoretical simulations of the films due to the opposite order in which the two interfaces are encountered in fabrication and simulation. The two position variables α , the angle of incidence, and φ , the rotation of the substrate about the axis normal to its surface, are independent, and implemented through predefined functions programmed into the control software:

$$\alpha = \alpha(z) \tag{A.1}$$

$$\varphi = \varphi(z) \tag{A.2}$$

The angle of incidence is measured in degrees, with 0° representing a substrate orientation with flux normal to the surface, and 90° with flux incident parallel to the surface (most GLAD films are deposited with α from 80° to 90°). The substrate rotation, φ , is measured in integral number of turns with positive values being indicative of substrate rotation in the counter-clockwise direction when looking at the surface to be deposited on. Included in this appendix are the predefined functions for several of the GLAD nanostructures developed for use in this research.

A.1 Slanted posts

At extremely oblique angles of incidence, the most basic GLAD film, the slanted post film, produces individual ‘matchsticks’ that grow in the deposition plane at a non-normal angle, less than the angle of flux incidence. The motion that produces this structure is given by

$$\alpha(z) = \alpha_0 \quad (\text{A.3})$$

$$\varphi(z) = \varphi_0 \quad (\text{A.4})$$

where α_0 and φ_0 are constants. To obtain highly porous films, α is typically maintained at values larger than 80° .

A.2 Chiral nanostructure

To produce helical films, the substrate is rotated at a constant speed relative to the deposition rate. By rotating the substrate, the deposition plane precesses around the substrate normal and the film grows in a related manner, producing a helical nanostructure. The motion of the substrate is defined by

$$\alpha(z) = \alpha_0 \quad (\text{A.5})$$

$$\varphi(z) = \pm \frac{z}{\Phi} \quad (\text{A.6})$$

The angle of incidence is kept constant throughout the deposition to maintain self-shadowing, while the pitch, Φ , which is the amount of vertical film growth per complete revolution of the substrate defines the rotation. The rotation direction determines the handedness of the nanostructure while the helical radius and cross section are determined by the deposition variables of material and angle of incidence.

A.3 Vertical posts

The adatom diffusion length characteristic of the deposited film material determines the width of the arms of a helical structure. For materials with a lower melting point, the structures tend to have thicker arms due to diffusion of the impinging vapour atoms, while higher melting point materials produce finer structures at a given angle of incidence. If the vertical pitch is small in comparison to the width of the chiral arms, the helical structural becomes fused into a vertical column. Thus by spinning the substrate at high speeds to distribute the flux evenly in all azimuthal directions, it is possible to produce vertical posts. The functions for α and φ used to produce vertical

posts are thus the same as those for a helical film, with the pitch chosen to be smaller than the natural chiral arm cross section diameter. Typical values of Φ for vertical posts are from 10 to 30 nm.

A.4 Zig Zags

If abrupt discontinuities in the nanostructure of a GLAD film are desired, rapid instantaneous motion is used at a given thickness value. The most basic of these films is the zigzag film, where slanted posts oriented at 180° from the previous layer are stacked upon each other. The motion is defined by

$$\alpha(z) = \alpha_0 \quad (\text{A.7})$$

$$\varphi(z) = \pm \frac{1}{2} \left\lfloor \frac{z}{\Phi/2} \right\rfloor \quad (\text{A.8})$$

where Φ is the vertical cycle including one ‘zig’ and one ‘zag’. This expression includes the floor function equal to the integer value of the argument discarding any fractional value. Thus a zigzag is produced by rotation of one-half turn at every half pitch, and at a constant angle of incidence.

A.5 Polygonal spirals

A variation on the zigzag structure, the polygonal spiral, produces a many-sided chiral structure used in the fabrication of periodic photonic band gap crystals. The most important of these structures is the square spiral where a four-sided staircase is grown. Similar to the zigzag, the motion is defined by

$$\alpha(z) = \alpha_0 \quad (\text{A.9})$$

$$\varphi(z) = \pm \frac{1}{j} \left\lfloor \frac{z}{\Phi/j} \right\rfloor \quad (\text{A.10})$$

where j is the number of sides. In the case of a square spiral, $j=4$, resulting in four 90° turns spaced periodically in z .

A.6 Exponential Capping

Often it is desirable to vary the density of the film as the flux accumulates, and to produce such an effect the angle of incidence is varied throughout the deposition. To create a solid capping film on top of an existing porous GLAD film, the angle of incidence is set to evolve exponentially from highly oblique to normal incidence as per the functions

$$\alpha(z) = (\alpha_2 - \alpha_1) \left[\frac{e^{-m \frac{(z_0 - z)}{z_0}} - e^{-m}}{1 - e^{-m}} \right] + \alpha_1 \quad (\text{A.11})$$

$$\varphi(z) = \pm \frac{z}{\Phi} \quad (\text{A.12})$$

where α_1 is the starting angle, α_2 is the final angle, z_0 is the total thickness, and m is the decay constant that controls the rate of transition from large to small values of α . Typical values of m are from 2 to 3. The substrate is rotated rapidly throughout the deposition of a capping layer to avoid anisotropy in the solid film with typical pitches, Φ , in the range from 10 to 30 nm.

A.7 Antireflection coatings

Applications of graded porosity films include antireflection coatings on glass, and by employing the variable angle of incidence in GLAD deposition accurate porosity profiles can be created. The profiles used in Chapter 5 were implemented by the functions

$$\alpha(z) = \cos^{-1} \left[\left(2e^{m \left(\frac{z}{z_0} \right)^2} - 1 \right)^{-1} \right] \quad (\text{A.13})$$

$$\varphi(z) = \pm \frac{z}{\Phi} \quad (\text{A.14})$$

where z_0 is the total thickness and m is the decay constant controlling the rate of progression from high to low density. The inverse cosine function is used to calculate the angle of incidence for a specific relative density given by the gaussian-exponential profile. Again the substrate is rotated rapidly with pitch, Φ , in the range of 10 to 30 nm.

A.8 User input file

Potentially the most versatile control routine that has been developed has the functions for α and ϕ taken from a set of data contained within a user developed input file. A series of three-element, tab delimited row vectors containing the thickness, corresponding angle of incidence and rotational orientation is read in from a text file. The thickness is input in nanometres and both the angle of incidence and rotational orientation in degrees (positive angles again correspond to counter-clockwise rotation and negative angles to clockwise rotation). The software routine checks the current thickness and finds the two row vectors that contain the next highest and lowest values for the thickness entries. The current angle of incidence and rotational orientation are set by linear interpolation calculated from the data points obtained from the two row vectors. An example of an input file is given below.

<u>z (nm)</u>	<u>α (°)</u>	<u>ϕ (°)</u>
0	85	0
199	85	0
200	85	180
600	85	540
800	30	4140

Table A.1 – Example of an input file used to control the structural parameters of a GLAD thin film. By specifying a series of data values for thickness, angle of incidence and rotational orientation it is possible to create a series of film nanostructure.

The starting row contains the initialization entries with the starting positions for the two angles and the thickness equal to zero. The subsequent line describes a 199 nm high slanted post layer deposited at 85°, followed by a zig on top and a one-turn helix with a pitch of 400 nm. The final line describes a capping layer using linear progression from high to low angles of incidence with a 20 nm pitch.

Assuming the two row vectors selected are labelled as row i and row $i+1$, the current values for α and φ are calculated from

$$\alpha = \alpha_i + \frac{\alpha_{i+1} - \alpha_i}{z_{i+1} - z_i} (z - z_i) \quad (\text{A.15})$$

$$\varphi = \varphi_i + \frac{\varphi_{i+1} - \varphi_i}{z_{i+1} - z_i} (z - z_i) \quad (\text{A.16})$$

B Appendix B

Simulation of GLAD Antireflection Coatings

Simulation of the optical response is a key component of the design of graded index coatings by glancing angle deposition (GRIN GLAD) for applications in antireflection (AR) devices. By accurately modelling the tailored nanostructures to determine transmission and reflection coefficients for the visible wavelengths of interest, greater insight can be gained into the fabrication of high quality films.

B.1 Effective medium theory

AR films of SiO₂ ($n_{\text{SiO}_2}=1.44$) were deposited on 7059 glass ($n_{\text{glass}}=1.53$) with graded relative porosity profiles given by the gaussian function

$$\rho_r(z) = \frac{\rho(z)}{\rho_0} = e^{-m\left(\frac{z_0-z}{z_0}\right)^2} \quad (\text{B.1})$$

where z_0 is the total AR film thickness, m is a decay constant responsible for fine-tuning the nanostructure of the film and hence its optical response, and ρ_0 is the bulk density of the film material, which is ideally matched to that of the substrate. To model this functional profile, the film was divided into a stack of p slabs, or sub-layers, of equal thickness, dz . Each of these layers was defined by a fixed index of refraction calculated from an effective medium theory (EMT) for the density given by Equation B.1 at its midpoint,

$$\rho_j = \rho_r\left(\left(j + \frac{1}{2}\right)dz\right) \quad j = 0, \dots, p-1 \quad (\text{B.2})$$

For both the fabricated and simulated films, the thickness, z_0 , was less than 360 nm and convergence was found for p greater than 20. The total number of layers was set in the simulation by the variable *nolayers* and was set equal to p .

Two EMTs were used to determine the effective index of refraction for each of the sub-layers of the simulated coating. The simpler Drude model and the more comprehensive Clausius-Mosotti-Lorenz-Lorentz (CMLL) or Maxwell Garnett (MG)

models were both implemented, with the effective dielectric constant given by the equation [105]

$$\varepsilon = \frac{\sum_{i=1}^l a_i \varepsilon_i C_i}{\sum_{i=1}^l a_i C_i} \quad (\text{B.3})$$

with

$$a_i = \begin{cases} 1 & (\text{Drude}) \\ 1/(\varepsilon_i + 2) & (\text{MG}) \end{cases} \quad (\text{B.3a})$$

where ε_i is the bulk dielectric constant and C_i is the relative concentration of the i th component. For the AR films on glass, $l=2$ with the two materials being air ($\varepsilon_{\text{air}}=1.00$) and silicon dioxide ($\varepsilon_{\text{SiO}_2}=2.074$). From comparison with actual spectra, the CMLL model was found to be more accurate and hence the files included in this appendix implement the more complex algorithm.

The relative concentration of each of the two component materials, air and SiO_2 , for each sub-layer was calculated from the gaussian density profile by

$$C_{\text{SiO}_2,j} = \rho_j \quad (\text{B.4})$$

$$C_{\text{air},j} = 1 - \rho_j \quad (\text{B.5})$$

while the effective index of refraction for each slab or sub-layer was found for the non-absorbing layers from

$$n_j = (\varepsilon_j)^{1/2} \quad (\text{B.6})$$

In the implementation of the model, the GRIN GLAD film has been reduced from a single layer with a continuously varying density to a multi-layer stack of discrete films, each with homogeneous properties.

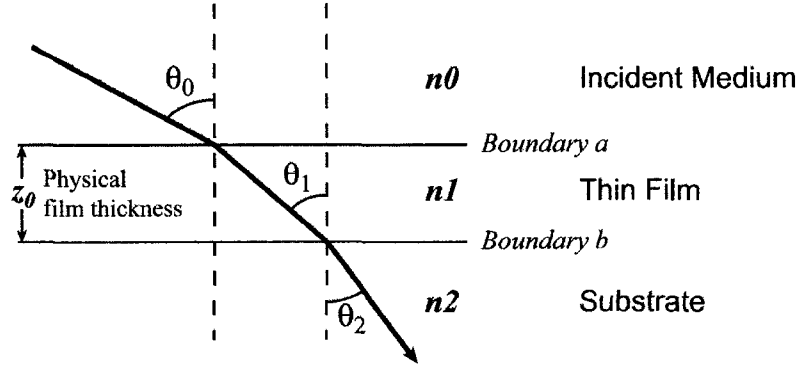


Figure B.1 – Coordinates used to calculate reflection and transmission by the Characteristic Matrix Method. The ray makes angles θ with the interface normals, z_0 is the physical film thickness and the layers have real indices of refraction, n .

B.2 Characteristic Matrix Method

To calculate the reflection and transmission through the model representation of the film composed of multiple layers, the Characteristic Matrix Method is used. Figure B.1 shows the configuration of the single film including the two interfaces, a and b . From derivations by MacLeod [14], if we define the admittance of an optical material by

$$Y = \frac{\vec{H}}{\vec{k} \times \vec{E}} \quad (\text{B.7})$$

we find that for a single thin film assembly composed of two interfaces, a substrate, an incident medium, and the film in question, the admittance of the overall assembly can be calculated from the characteristic matrix,

$$\begin{pmatrix} \vec{k} \times \vec{E}_a \\ C \end{pmatrix} \begin{bmatrix} B \\ C \end{bmatrix} = \begin{bmatrix} \cos \delta_1 & (i \sin \delta_1) / \eta_1 \\ i \eta_1 \sin \delta_1 & \cos \delta_1 \end{bmatrix} \begin{bmatrix} 1 \\ \eta_2 \end{bmatrix} \begin{pmatrix} \vec{k} \times \vec{E}_b \end{pmatrix} \quad (\text{B.8})$$

with

$$Y = \frac{C}{B} = \frac{\eta_2 \cos \delta_1 + i \sin \delta_1}{\cos \delta_1 + i(\eta_2 / \eta_1) \sin \delta_1} \quad (\text{B.8a})$$

The components of this equation are, η_1 and η_2 , the modified admittances of the film and substrate materials respectively, taking into account the angular dependence of the incident beam, δ_1 is the phase shift undergone by the wave as it passes through the film

thickness, and i is the imaginary constant equal to the square root of negative one. As the two linear polarizations, transverse electric (TE) and transverse magnetic (TM), are subject to continuity of their tangential components to the surface across the interface, these conditions define the modified admittance by

$$\eta_{TE} = n \cos \theta \quad (\text{B.9})$$

$$\eta_{TM} = \frac{n}{\cos \theta} \quad (\text{B.10})$$

where n is the bulk index of the refracting medium and θ is the angle that the refracted ray makes with the normal to the surface. The phase delay incurred by the wave as it propagates through the film is given by

$$\delta_1 = \frac{2\pi n_1}{\lambda} \cos \theta_1 \cdot z_0 \quad (\text{B.11})$$

where n_1 is the again the index of refraction of the film or layer, λ is vacuum wavelength of the incident light, z_0 is the physical thickness of the film or layer, and θ_1 is the angle that the ray in the film makes with the normal to the surface.

To find the characteristic matrix of a stack of multiple thin films, the matrices of subsequent layers can simply be appended to the left hand side of the expression in Equation B.8. For an assembly of p layers plus the substrate, denoted by the index $p+1$, we can calculate its characteristic impedance from

$$\begin{bmatrix} B \\ C \end{bmatrix} = \left\{ \prod_{r=1}^p \begin{bmatrix} \cos \delta_r & (i \sin \delta_r) / \eta_r \\ i \eta_r \sin \delta_r & \cos \delta_r \end{bmatrix} \right\} \begin{bmatrix} 1 \\ \eta_{p+1} \end{bmatrix}, \quad \text{with } Y = \frac{C}{B} \quad (\text{B.12})$$

The characteristic impedance, Y , of the assembly provides insight into the interaction of a wavefront incident from a known medium and the film stack. In particular, the reflectivity of the assembly is given by

$$r = \frac{\eta_0 - Y}{\eta_0 + Y} \quad (\text{B.13})$$

yielding a reflectance,

$$R = \left(\frac{\eta_0 - Y}{\eta_0 + Y} \right) \left(\frac{\eta_0 - Y}{\eta_0 + Y} \right)^* \quad (\text{B.14})$$

B.3 Rayleigh Scattering

As the SiO₂ films are non-absorbing, it would be expected that the transmittance might be calculated by simple conservation of energy,

$$T = 1 - R \quad (\text{B.15})$$

however Rayleigh scattering that occurs at the rough surfaces of the film nanostructure reduces the overall transmission and is also wavelength dependent. Resultantly, a scattering correction factor, C_{Rayleigh} , must be included, and thus the corrected transmission is calculated by

$$T_{\text{corr}}(\lambda) = C_{\text{Rayleigh}}(\lambda)[1 - R(\lambda)] \quad (\text{B.16})$$

where

$$C_{\text{Rayleigh}}(\lambda) = \frac{2.75 \times 10^{-28}}{\lambda^4} \quad (\text{B.17})$$

These results were compared with actual measurement values for the films named by *ar#* where # represents the film's serial number in the overall set of deposited films.

B.4 Backside reflection

As the measurements performed on the fabricated films had reduced transmission due to reflection from the backside of the substrate, one final correction was made to the measurement values so that comparison of only the AR coatings could be made. The reflection from the backside interface was calculated for both TE and TM modes by

$$R_{TE} = \left[\frac{\sin(\theta_i - \theta_t)}{\sin(\theta_i + \theta_t)} \right]^2 \quad (\text{B.18})$$

$$R_{TM} = \left[\frac{\tan(\theta_i - \theta_t)}{\tan(\theta_i + \theta_t)} \right]^2 \quad (\text{B.19})$$

Where θ_i is the angle that the incident ray makes with the normal to the glass/air interface and θ_t is the angle that the transmitted ray makes with the normal. The results from these calculations were added to the spectra obtained so that comparisons of just the AR layers could be made.

B.5 Matlab code files

Included below are the two Matlab© m-files written to calculate transmission and reflection for the fabricated GRIN GLAD antireflection film.

B.5.1 Calculations for TE modes

```
%AR coating simulation Version 3.0 - Lorentz/Lorenz Calculation at non-zero angles
%for specular transmission
%****TE MODES ONLY (s-polarization)****

clear;
%Define wavelength boundaries and wavelength increment
minlambda=400;
maxlambda=1000;
dellambda=1;
lambda=[minlambda:dellambda:maxlambda]*1e-9;

%Define film parameters (gaussian profile only)
m=2.5;          %*****Set for each film*****
totalthick=295e-9; %*****Set for each film*****
nolayers=30;
delthick=totalthick/nolayers;
ESiO2=(1.44)^2;
EAir=1;
NSubs=1.53;     %7059 glass
file='ar1';    %*****Each file has a unique name identified by ar#*****

%Define measurement angles
mintheta=0;
maxtheta=30;
deltheta=10;
theta=[mintheta:deltheta:maxtheta];

%calculate film density profile
z=ones(1,nolayers);
for n=1:nolayers
    z(1,n)=n-0.5; %midpoint of each layer is used for each slab calculation
```

```

end
z=delthick*z;
RHO=exp(-m*(z./totalthick).^2);
RHO=flipr(RHO);
%minimum relative density is 17% (from AFM data)
for n=1:nolayers
    if RHO(1,n)<0.17
        RHO(1,n)=0.17;
    end
end

%calculate effective index
%Lorentz-Lorenz (NLL) formula
ELL=((RHO*ESiO2/(ESiO2+2))+((1-RHO)*EAir/(EAir+2)))./((RHO/(ESiO2+2))+((1-
RHO)/(EAir+2)));
NLL=ELL.^(.5); %N__ is the vector containing n as a function of z

%calculate spectral reflection

%angles as they propagate through the film
%THETA FILM (in rad) has first entry of air, second entry
THETA FILM=ones(length(theta),nolayers+1);
THETA FILM(:,1)=pi*theta/180;
THETA FILM(:,2)=asin((1/NLL(1,1))*sin(THETA FILM(:,1)));
for n=3:nolayers+1
    THETA FILM(:,n)=asin((NLL(1,n-2)/NLL(1,n-1))*sin(THETA FILM(:,n-1)));
end
SUBANGLES=asin((NLL(1,length(NLL))/NSubs)*sin(THETA FILM(:,length(THETA
FILM))));
    %angles w.r.t. the substrate normal for each incidence angle

%calculate characteristic matrices of layers
R=ones(length(theta),length(lambda)); %initialize Reflectivity matrix
%calculation of phase shift per thickness (DELTA)
DELTA=ones(length(NLL),length(lambda));
for q=1:length(theta)
    const=2*pi*delthick;
    DELTA=ones(length(NLL),length(lambda));
    for n=1:length(lambda)
        DELTA(:,n)=const*(NLL)';
    end
    for n=1:length(NLL)
        DELTA(n,:)=DELTA(n,:).*cos(THETA FILM(q,n))./lambda;
    end

%calculation of matrices (one for each lambda)

```

```

for n=1:length(lambda)
    A=eye(2,2);
    for j=1:length(NLL)
        a=[cos(DELTA(j,n)) i*sin(DELTA(j,n))/(NLL(1,j)*cos(THETAFILM(q,j)));
i*NLL(1,j)*cos(THETAFILM(q,j))*sin(DELTA(j,n)) cos(DELTA(j,n))];
        A=A*a;
    end
    y=A*[1; NSubs*cos(SUBSANGLES(q))];
    Y=y(2,1)/y(1,1); %Admittance of the stack for each angle and
wavelength
    R(q,n)=((EAir-Y)/(EAir+Y))*conj((EAir-Y)/(EAir+Y));
end
end

```

```

%correction for Rayleigh scattering
C=2.75e-28;
rayleigh=C./(lambda.^4);
%%%%%%%%%%
T=100-R.*100;
for n=1:length(theta)
    Tcorrected(n,:)=T(n,:).*(1-rayleigh); %Correction factor for Rayleigh scattering
end

```

```

figure(1)
%load measurement data
eval(sprintf('load D:\AntiReflection\gaussianfilms\unprocessed\%s0spS.rls;',file));
eval(sprintf('load D:\AntiReflection\gaussianfilms\unprocessed\%s10sS.rls;',file));
eval(sprintf('load D:\AntiReflection\gaussianfilms\unprocessed\%s20sS.rls;',file));
eval(sprintf('load D:\AntiReflection\gaussianfilms\unprocessed\%s30sS.rls;',file));
%correct for substrate reflection
TANGLES=asin(NSubs*sin(SUBSANGLES)); %calculate the transmission angles
emerging from the substrate
corrref=ones(length(TANGLES));
for n=2:length(TANGLES)
    corrref(n)=100*(sin(SUBSANGLES(n)-
TANGLES(n))./sin(SUBSANGLES(n)+TANGLES(n))).^2;
end
corrref(1)=4.39; %normal incidence correction

```

```

%add backside reflection to measurement results
a0=eval(sprintf('%s0spS+[zeros(length(%s0spS),1)
corrref(1)*ones(length(%s0spS),1)];',file,file,file));
a1=eval(sprintf('%s10sS+[zeros(length(%s10sS),1)
corrref(2)*ones(length(%s10sS),1)];',file,file,file));
a2=eval(sprintf('%s20sS+[zeros(length(%s20sS),1)
corrref(3)*ones(length(%s20sS),1)];',file,file,file));

```

```

a3=eval(sprintf('%s30sS+[zeros(length(%s30sS),1)
corrref(4)*ones(length(%s30sS),1)];',file,file,file));

subplot(4,1,1), axis([(minlambda-20) (maxlambda+20) 98.5 100]);
hold on;
subplot(4,1,1), ylabel('%T');
subplot(4,1,1), text(410,99.8,'TE - 0^o');
subplot(4,1,1), plot(lambda*1e9,Tcorrected(1,:),'k--');
subplot(4,1,1), plot(a0(:,1),a0(:,2),'k');
hold off;

subplot(4,1,2), axis([(minlambda-20) (maxlambda+20) 98.5 100]);
hold on;
subplot(4,1,2), ylabel('%T');
subplot(4,1,2), text(410,99.8,'TE - 10^o');
subplot(4,1,2), plot(lambda*1e9,Tcorrected(2,:),'k--');
subplot(4,1,2), plot(a1(:,1),a1(:,2),'k');
hold off;

subplot(4,1,3), axis([(minlambda-20) (maxlambda+20) 98.5 100]);
hold on;
subplot(4,1,3), ylabel('%T');
subplot(4,1,3), text(410,99.8,'TE - 20^o');
subplot(4,1,3), plot(lambda*1e9,Tcorrected(3,:),'k--');
subplot(4,1,3), plot(a2(:,1),a2(:,2),'k');
hold off;

subplot(4,1,4), axis([(minlambda-20) (maxlambda+20) 98.5 100]);
hold on;
subplot(4,1,4), plot(lambda*1e9,Tcorrected(4,:),'k--');
subplot(4,1,4), xlabel('Wavelength (nm)');
subplot(4,1,4), ylabel('%T');
subplot(4,1,4), text(410,99.8,'TE - 30^o');
subplot(4,1,4), plot(a3(:,1),a3(:,2),'k');
hold off;

legend('0^o','10^o','20^o','30^o','Measurement 0^o','Measurement 10^o','Measurement
20^o','Measurement 30^o',4);

```

B.5.2 Calculations for TM modes

```

%AR coating simulation Version 3.1 - Lorentz/Lorenz Calculation at non-zero angles
%for specular transmission
%****TM MODES ONLY (p-polarization)****

```

```

clear;
%Define wavelength boundaries and wavelength increment
minlambda=400;
maxlambda=1000;
dellambda=1;
lambda=[minlambda:dellambda:maxlambda]*1e-9;

%Define film parameters (gaussian profile only)
m=2.5;          %*****Set for each film*****
totalthick=295e-9; %*****Set for each film*****
nolayers=29;
delthick=totalthick/nolayers;
ESiO2=(1.44)^2;
EAir=1;
NSubs=1.53;    %7059 glass
file='ar1';   %*****Each file has a unique name identified by ar#*****

%Define measurement angles
mintheta=0;
maxtheta=30;
deltheta=10;
theta=[mintheta:deltheta:maxtheta];

%calculate film density profile
z=ones(1,nolayers);
for n=1:nolayers
    z(1,n)=n-0.5; %midpoint of each layer is used for each slab calculation
end
z=delthick*z;
RHO=exp(-m*(z./totalthick).^2);
RHO=fliplr(RHO);
%minimum relative density is 17% (from AFM data)
for n=1:nolayers
    if RHO(1,n)<0.17
        RHO(1,n)=0.17;
    end
end

%calculate effective index
%Lorentz-Lorenz (NLL) formula
ELL=((RHO*ESiO2/(ESiO2+2))+((1-RHO)*EAir/(EAir+2)))/((RHO/(ESiO2+2))+((1-
RHO)/(EAir+2)));
NLL=ELL.^(.5); %N__ is the vector containing n as a function of z

%calculate spectral reflection

```

```

%angles as they propagate through the film
%THETA FILM (in rad) has first entry of air, second entry
THETA FILM=ones(length(theta),nolayers+1);
THETA FILM(:,1)=pi*theta/180;
THETA FILM(:,2)=asin((1/NLL(1,1))*sin(THETA FILM(:,1)));
for n=3:nolayers+1
    THETA FILM(:,n)=asin((NLL(1,n-2)/NLL(1,n-1))*sin(THETA FILM(:,n-1)));
end
SUBSANGLES=asin((NLL(1,length(NLL))/NSubs)*sin(THETA FILM(:,length(THETA
FILM))));
    %angles w.r.t. the substrate normal for each incidence angle

%calculate characteristic matrices of layers
R=ones(length(theta),length(lambda)); %initialize Reflectivity matrix
%calculation of phase shift per thickness (DELTA)
DELTA=ones(length(NLL),length(lambda));
for q=1:length(theta)
    const=2*pi*delthick;
    for n=1:length(lambda)
        DELTA(:,n)=const*(NLL)';
    end
    for n=1:length(NLL)
        DELTA(n,:)=DELTA(n,:).*cos(THETA FILM(q,n))./lambda;
    end

    %calculation of matrices (one for each lambda)
    for n=1:length(lambda)
        A=eye(2,2);
        for j=1:length(NLL)
            a=[cos(DELTA(j,n)) i*sin(DELTA(j,n))/((NLL(1,j)/cos(THETA FILM(q,j))));
i*NLL(1,j)*sin(DELTA(j,n))/cos(THETA FILM(q,j)) cos(DELTA(j,n))];
            A=A*a;
        end
        y=A*[1;(NSubs/cos(SUBSANGLES(q)))]';
        Y=y(2,1)/y(1,1); %Admittance of the stack for each angle and
wavelength
        R(q,n)=((EAir-Y)/(EAir+Y))*conj((EAir-Y)/(EAir+Y));
    end
end

%correction for Rayleigh scattering
C=2.75e-28;
rayleigh=C./(lambda.^4);
%%%%%%%%%%
T=100-R.*100;
for n=1:length(theta)

```

```

    Tcorrected(n,:)=T(n,:).*(1-rayleigh); %Correction factor for Rayleigh scattering
end

figure(1)
%load measurement data
eval(sprintf('load D:\\AntiReflection\\gaussianfilms\\unprocessed\\%s0spS.rls;',file));
eval(sprintf('load D:\\AntiReflection\\gaussianfilms\\unprocessed\\%s10pS.rls;',file));
eval(sprintf('load D:\\AntiReflection\\gaussianfilms\\unprocessed\\%s20pS.rls;',file));
eval(sprintf('load D:\\AntiReflection\\gaussianfilms\\unprocessed\\%s30pS.rls;',file));

%correct for substrate reflection
TANGLES=asin(NSubs*sin(SUBSANGLES)); %calculate the transmission angles
emerging from the substrate
corrref=ones(length(TANGLES));
for n=2:length(TANGLES)
    corrref(n)=100*(tan(SUBSANGLES(n)-
TANGLES(n))./tan(SUBSANGLES(n)+TANGLES(n))).^2;
end
corrref(1)=4.39; %normal incidence correction

%add backside reflection to measurement results
a0=eval(sprintf('%s0spS+[zeros(length(%s0spS),1)
corrref(1)*ones(length(%s0spS),1)];',file,file,file));
a1=eval(sprintf('%s10pS+[zeros(length(%s10pS),1)
corrref(2)*ones(length(%s10pS),1)];',file,file,file));
a2=eval(sprintf('%s20pS+[zeros(length(%s20pS),1)
corrref(3)*ones(length(%s20pS),1)];',file,file,file));
a3=eval(sprintf('%s30pS+[zeros(length(%s30pS),1)
corrref(4)*ones(length(%s30pS),1)];',file,file,file));

subplot(4,1,1), axis([(minlambda-20) (maxlambda+20) 98.5 100]);
hold on;
subplot(4,1,1), plot(lambda*1e9,Tcorrected(1,:),'k--');
subplot(4,1,1), ylabel('%T');
subplot(4,1,1), text(410,99.8,'TM - 0^o');
subplot(4,1,1), plot(a0(:,1),a0(:,2),'k');
hold off

subplot(4,1,2), axis([(minlambda-20) (maxlambda+20) 98.5 100]);
hold on;
subplot(4,1,2), plot(lambda*1e9,Tcorrected(2,:),'k--');
subplot(4,1,2), ylabel('%T');
subplot(4,1,2), text(410,99.8,'TM - 10^o');
subplot(4,1,2), plot(a1(:,1),a1(:,2),'k');
hold off;

```

```

subplot(4,1,3), axis([(minlambda-20) (maxlambda+20) 98.5 100]);
hold on;
subplot(4,1,3), plot(lambda*1e9,Tcorrected(3,:),'k--');
subplot(4,1,3), ylabel('%T');
subplot(4,1,3), text(410,99.8,'TM - 20^o');
subplot(4,1,3), plot(a2(:,1),a2(:,2),'k');
hold off;

subplot(4,1,4), axis([(minlambda-20) (maxlambda+20) 98.5 100]);
hold on;
subplot(4,1,4), plot(lambda*1e9,Tcorrected(4,:),'k--');
subplot(4,1,4), xlabel('Wavelength (nm)');
subplot(4,1,4), ylabel('%T');
subplot(4,1,4), text(410,99.8,'TM - 30^o');
subplot(4,1,4), plot(a3(:,1),a3(:,2),'k');
hold off;

legend('0^o','10^o','20^o','30^o','Measurement 0^o','Measurement 10^o','Measurement
20^o','Measurement 30^o',4);

```

Scott R Kennedy

From: "Elizabeth Potts" <Elizabeth.Potts@tandf.co.uk>
To: <skennedy@ee.ualberta.ca>
Sent: July 25, 2003 8:48 AM
Subject: Your permission request

Dear Scott R Kennedy

Thank you for your correspondence requesting permission to reproduce the following material from our Journal in your dissertation.

'Optical activity of chiral thin film and liquid crystal hybrids' by S R Kennedy, J C Sit, D J Broer and M J Brett, Liquid Crystals, (2001) vol. 28 no. 12 pp 1700-1803

As you are one of the authors of the article, we will be pleased to grant entirely free permission on the condition that you acknowledge the original source of publication and insert a reference to the Journal's web site:

<http://www.tandf.co.uk>

Thank you for your interest in our Journal.

Yours sincerely

Elizabeth Potts
Permissions Administrator (UK) Journals
Elizabeth.Potts@tandf.co.uk

24/10/2003